

**Determination of Thermal Strains  
In the Neighborhood of a Bimaterial Interface**


by

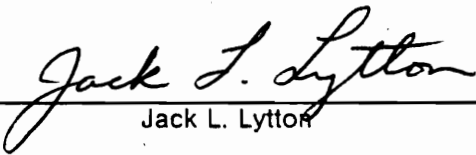
Judy D. Wood

Dissertation submitted to the Faculty of the  
Virginia Polytechnic Institute and State University  
in partial fulfillment of the requirements for the degree of  
Doctor of Philosophy  
in  
Materials Engineering Science

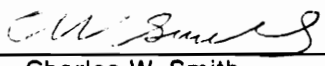
APPROVED:

  
\_\_\_\_\_  
Daniel Post, Chairman

  
\_\_\_\_\_  
Kenneth L. Reifsnider, Program Chairman

  
\_\_\_\_\_  
Jack L. Lytton

  
\_\_\_\_\_  
Don H. Morris

  
\_\_\_\_\_  
Charles W. Smith

February, 1992

Blacksburg, Virginia

**Determination of Thermal Strains  
in the Neighborhood of a Bimaterial Interface**

by

Judy D. Wood

Daniel Post, Chairman

Materials Engineering Science

(ABSTRACT)

An experimental analysis was conducted on a bimaterial plate of steel and brass, subjected to a uniform temperature change. The steel and brass portions of the plate were joined along a common edge with a nearly zero thickness medium. Whole-field, in-plane displacement measurements  $U$  and  $V$  were made by means of high-sensitivity moiré interferometry. The corresponding distributions of stresses,  $\sigma_x$ ,  $\sigma_y$ , and  $\tau_{xy}$  were determined for the free surface. Near the interface, and along its length, the largest stresses were  $\sigma_y$ , acting perpendicular to the interface. The  $\sigma_y$  peaks occurred very close to the interface, but not on it. These peak values were tensile in the steel and compressive in the brass. The transition between these opposite peak stresses featured an extremely strong gradient in a  $50 \mu m$  interface zone. The distribution was akin to that of a stress singularity, but the stresses reached finite peak values in the physical experiment. Even larger stresses were found near the corner, where the interface of the two materials intersects the free edge. Both macroscopic and microscopic moiré interferometry were required to determine the stress distribution.

## **Acknowledgements**

I would like to express my sincere thanks to all of the members of my thesis committee, the Materials Engineering Science Program Chairman, Dr. K. L. Reifsnider, Dr. J. L. Lytton, Dr. D. H. Morris, Prof. C. W. Smith, and my advisor, Dr. Daniel Post, for their continuous assistance and support, as well as their sincere respect and dedication, throughout my graduate studies. They have shown me a tremendous amount of trust and respect, in addition to their technical support.

This work was sponsored by the National Center for Composite Materials Research under ONR Grant N00014-86-K0799 and by Sandia National Laboratories under Contract No. 75-8962. The support, scientific interest, and encouragement from these organizations has been gratefully appreciated.

And, most of all, this work would not have been possible without the extraordinary skill, patience, support, and sincere respect of my medical doctors, especially Drs. Eric Chino, Jeffrey P. Cichon, Robert W. Stockburger, Ronald L. Myers, and David S. Bell. Each of them has shown me such a tremendous amount of trust and faith. They believed in me. But, even more

importantly, they showed me that I was worth their faith. I owe them a great deal of gratitude. They are very special and extraordinary people, to whom I literally owe my life.

And, finally, I would like to thank my advisor, Dr. Daniel Post, and my best friend, Mara Knott, for standing by and helping me.

# Table of Contents

<b>Chapter 1: Introduction</b> .....	<b>1</b>
<b>Chapter 2: Background and Literature Review</b> .....	<b>3</b>
2.1 Initial Developments .....	6
2.1.1 Saint-Venant's Principle .....	6
2.1.2 Development of the End Solution .....	7
2.1.3 Similarity with Single-Lap Joints and Previous Work .....	10
2.2 Considerations in Formulating the Problem .....	15
2.2.1 Three Dimensionality - (A Strength-of-Materials Approach) .....	15
2.2.2 Inapplicability of Plane Stress and Plane Strain .....	18
2.3 Recent Developments .....	20
2.3.1 Recent Theoretical and Numerical Solutions .....	20
2.3.2 Correlation with Experimental Measurements .....	21
2.4 Applications .....	23
2.4.1 Application to Composites .....	23
<b>Table of Contents</b>	<b>v</b>

2.4.2	Other applications of this problem	25
2.4.3	Interface Stresses and Plasticity	25
2.5	Background Summary	28
<b>Chapter 3:</b>	<b>Experimental Investigation</b>	<b>29</b>
3.1	Specimen Material and Geometry	29
3.2	The Experimental Method: Moiré Interferometry	35
3.2.1	Introduction	35
3.2.2	Moiré Interferometry - the Basic Principle	36
3.3	Experimental Procedure	37
3.3.1	Method for Absolute Thermal Strain Measurements	38
3.3.2	Zero-expansion Mold	39
3.3.3	Specimen Grating, Elevated Temperature	41
3.3.4	Optical Apparatus and Virtual Reference Grating	41
3.3.5	Virtual Reference Grating - Calibration	43
3.3.6	Moiré Carrier Patterns	45
3.4	Data Extraction from Experimental Results	48
3.4.1	Recording Data	48
3.4.2	Specimen A - An Example of the Experimental Method	48
3.4.3	Data Reduction	50
3.4.3.1	Calculation of Strains and Stresses	50
3.4.3.2	Specimen-A: An Example of the Experimental method, using carrier patterns	52
<b>Chapter 4:</b>	<b>Experimental Results</b>	<b>54</b>
4.1	Results: Specimen - A	55
4.1.1	The Use of Moiré Interferometry	55

4.1.2	The Use of Mechanical Differentiation	60
4.1.3	Graphs and Contour Maps	64
4.2	Technique developed for increasing sensitivity of the experimental method.	69
4.3	The turn-around-point	72
4.4	Summary of Results	80
<b>Chapter 5: Interpretation and Discussion</b>		<b>81</b>
5.1	Stresses within the Interface Zone, Specimen A,D	81
5.2	Supplementary Experiment	83
5.3	Discussion	88
<b>Chapter 6: Conclusions</b>		<b>89</b>
<b>References</b>		<b>91</b>
<b>Vita</b>		<b>106</b>

# List of Illustrations

Figure 1. Two-dimensional strength-of-materials approach. . . . .	5
Figure 2. Radius of curvature varies with material properties and geometry. . . . .	8
Figure 3. Similarities between (a) adhesive-lap joints and (b) bimaterial joints. . . . .	11
Figure 4. Adhesive deformation of a lap joint varies with material properties. . . . .	13
Figure 5. Stress similarities between (a) a lap joint and (b) a bimaterial joint. . . . .	14
Figure 6. 2-D vs. 3-D deformations of a bimaterial joint. . . . .	16
Figure 7. Two-dimensional deformations with corresponding two-dimensional stresses. . . . .	17
Figure 8. 3-D deformations with corresponding 3-D stresses. . . . .	17
Figure 9. Applicable problem for plane stress. . . . .	19
Figure 10. Applicable problem for plane strain. . . . .	19
Figure 11. BEM results by Terasaki, et. al. [37]. . . . .	22
Figure 12. Experimental results using strain gages, by Suganuma, et. al. [47]. . . . .	22
Figure 13. Stress-strain behavior of a strain-hardening material. . . . .	27
Figure 14. Specimen-A geometry and material properties. . . . .	30
Figure 15. Relative orientation of specimen dimensions. . . . .	31
Figure 16. Specimen geometries (a) A, (b) B, and (c) C. . . . .	32
Figure 17. Specimen-D geometry and material properties. . . . .	34
Figure 18. Grating replication at (a) Room-temperature and (b) elevated-temperature. . . . .	40
Figure 19. Four-beam moiré interferometer and specimen with deformed grating. . . . .	42



Figure 20. ULE grating mold (a) original orientation, (b) replicated, and (c) rotated, only. . . . .	44
Figure 21. Specimen-A. V-displacement field without a carrier pattern. . . . .	47
Figure 22. Specimen-A. V-displacement field with a carrier pattern. . . . .	47
Figure 23. The V-displacement field in the stress-free brass corner, (a) without, and (b) with carrier pattern. . . . .	53
Figure 24. Specimen-A. V-displacement fields in the shaded region for $\Delta T = -133^{\circ}\text{C}$ . . . . .	56
Figure 25. Specimen-A. U-displacement fields in the shaded region for $\Delta T = -133^{\circ}\text{C}$ . . . . .	57
Figure 26. Specimen A. (a) V-displacement field, and (b) with higher magnification. . . . .	59
Figure 27. Contours of displacement derivatives by mechanical differentiation. . . . .	61
Figure 28. Specimen-A. Stress-induced strains along the $y'$ axis. . . . .	65
Figure 29. Specimen-A. The distribution of stresses on the $y'$ axis. . . . .	67
Figure 30. Specimen-A. The distribution of peak stresses along the interface. . . . .	68
Figure 31. Specimen-A. Contour maps of surface stress distributions. . . . .	70
Figure 32. Specimen-B. Total V-displacement field. . . . .	73
Figure 33. Specimen-B. V-displacement field, with carrier fringes of extension. . . . .	74
Figure 34. Specimen-B. Stresses perpendicular to the interface along the centerline. . . . .	75
Figure 35. Specimen-C. V-displacement field. . . . .	77
Figure 36. Specimen-C. (a) V field without, (b) with carrier, and (c) W field, with carrier. . . . .	78
Figure 37. Specimen-C. Stresses perpendicular to the interface along the centerline. . . . .	79
Figure 38. Specimen-D. Microscopic moiré patterns corresponding to Figures 20 and 21(b). . . . .	85
Figure 39. The distribution of stresses near the interface, perpendicular to the interface. . . . .	87

# List of Tables

Table 1. Approaches found in the literature for solving the bimaterial problem. . . . .	3
Table 2. Additional approaches used to determine the interface-stress distribution in a composite-free-edge problem. . . . .	24
Table 3. Applications of the bimaterial problem. . . . .	26
Table 4. Specimen geometric aspect ratios. . . . .	31
Table 5. Specimen material properties. . . . .	33
Table 6. Governing equations for the thermal-strain problem. . . . .	51
Table 7. Temperature increments, thermal strains, and coefficients of thermal expansion. . . . .	55
Table 8. Effect of geometric aspect ratio on turn-around-point. . . . .	76

# Chapter 1

## Chapter 1: Introduction

In every case where dissimilar materials are bonded together and undergo a subsequent change of temperature, there will be residual stresses developed because of the mismatch of material properties. These residual stresses can be very large and may have a significant influence on the life of that product. For this reason, it is of great importance to clearly define the state of stress existing in a bimaterial joint. This problem can be approached as a strength-of-materials problem, an elasticity problem, a materials problem, as well as an interface problem of composite materials.

The state of stress near the interface of a bimaterial joint is very complex. The stress field is statically indeterminate and self-equilibrating. In addition, the stress field may induce zones of plastic as well as elastic deformation. Because of these complexities, a complete analytical solution to this problem does not appear in the literature. However, there are several useful approaches in the literature based on various assumptions that have simplified the problem. Analytical solutions usually involve a number of parameters and assumptions which may not

be completely understood. Therefore, experimental work, recording actual strains and displacements in a bimaterial joint, is needed to supplement these theoretical solutions.

The motivation for the following experimental work was to produce detailed knowledge of the thermally induced deformation in the interface region of a bimaterial joint. This investigation may also be useful to gain insight into the performance of bimaterial joints under mechanical loading because the critical stresses in a bimaterial joint subjected to mechanical loading are directly analogous to those caused by thermal loading.

## Chapter 2

### Chapter 2: Background and Literature Review

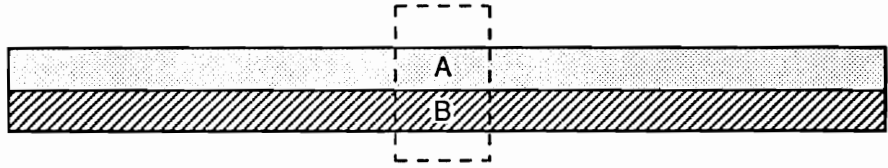
Theoretical solutions to the bimaterial problem have been evolving over the past 60 years with rather little guidance from detailed experimental work. Without this guidance, several different approaches have emerged. These can be divided into the five categories shown in Table 1, where the numbers in brackets pertain to corresponding literature citations in the Reference section.

**Table 1. Approaches found in the literature for solving the bimaterial problem.**

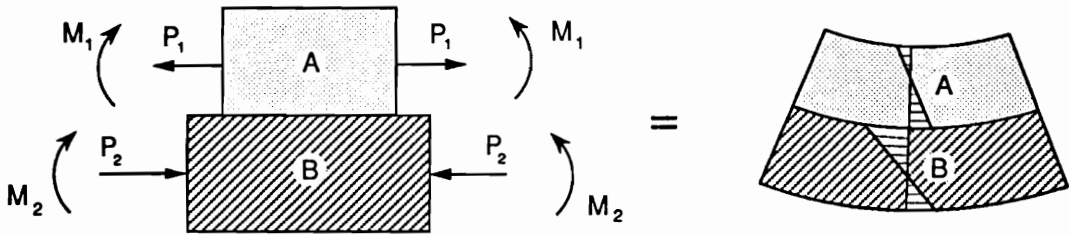
	<u>References</u>
1. Strength of materials (beam theory)(2-D) .....	[1,2,3,4,5,6,7,8,9,10,11,12]
2. Eigenfunction series approximations (2-D) .....	[10,11,12,13,14,15]
3. Elasticity (2-D, and 3-D) .....	[16,17,18,19,20,21,22,23,24,25,26,27,28,29,30]
4. Finite Element Method (3-D) .....	[31,32,33,34,35,36]
Boundary Element Method (2-D, and 3-D) .....	[37,38]
5. Experimental Measurements .....	[39,40,41,42,43,44,45,46,47,48,49,50]

The bimaterial problem was studied by Timoshenko in 1925 [1] using a strength of materials or beam theory approach. Timoshenko [1] wrote a seminal paper on the two-dimensional plane-stress analysis of a bimaterial bonded strip, subjected to a uniform thermal change. He used a two-dimensional analysis to describe the deformation of a bi-material bonded strip subjected to a uniform temperature change. Figure 1 illustrates this approach. With a given temperature change, material B expands more than material A. If the two materials remain bonded along the interface, material A is stressed in tension at the interface and material B in compression so that they are the same length along the interface. Timoshenko represented this loading as a combination of an axial load,  $P$ , and a moment,  $M$ , acting on each component. This analysis produced relatively good results, except near the ends of the strip, and near the interface. Timoshenko, himself, noted that the stress-distribution must be more complicated in these regions. Boley and Weiner also made contributions with a very similar approach [3].

Timoshenko's solution to the bimaterial problem is a special case of a beam in bending. It is a good approximation of the stress field away from the ends. However, with Timoshenko's solution, as with a beam in bending, the axial stress varies linearly with depth in each lamina, as shown in Figure 1(c). However, the ends of the bimaterial beam are traction free and therefore the stress field near the ends must change to satisfy the stress-free boundary conditions.

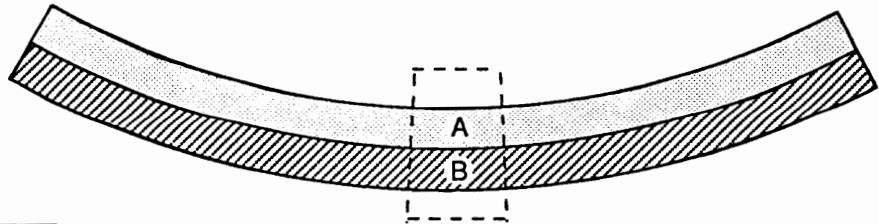


(a) Undeformed specimen



(b) Free expansion of each unbonded part with simplified loading model of mutual constraint.

(c) Bonded geometry of center portion.



for  $\alpha_B > \alpha_A$   
with  $T_2 > T_1$

(b) Bonded geometry of beam.

Figure 1. Two dimensional strength-of-materials approach.

## **2.1 Initial Developments**

### **2.1.1 Saint-Venant's Principle**

Timoshenko was actually applying Saint-Venant's principle to his formulation of the bimaterial problem. This allowed him to solve a much simpler problem and then apply this solution to the bimaterial problem. Saint Venant's principle assumes that the stress fields away from the end are essentially the same in both the bimaterial problem and the simplified problem of Figure 1(b), provided the applied loads are statically equivalent.

As a separate example, a distributed load can be represented by a (statically-equivalent) point load, which makes the problem much easier to solve. However, this simpler solution does not apply in the region near the loading point and it is understandable that the two stress fields in this region would not be alike. However, the difference between the two stress fields decays in a characteristic length away from the loading region until the difference is negligible.

This characteristic decay length varies, but it is often assumed to be approximately equal to the height of the beam (or lamina). Alwar [44] measured this decay length experimentally, using photoelastic techniques. He determined that the decay of the end effect is much slower for a laminated beam than for a solid beam. This decay length increased with an increasing difference in Young's Modulus between adjacent lamina. Accordingly, the two-dimensional strength of materials solution cannot be applied to accurately determine the stress field that is within this characteristic length from the end of the beam. If the beam is shorter than twice this characteristic length, the two-dimensional strength-of-materials solution will not approxi-



mate the stress field anywhere in the beam. Therefore, it is erroneous to evaluate the stresses in a short beam by using Timoshenko's formula, which incorporates Saint-Venant's principle.

The two-dimensional strength of materials or beam theory approach does not consider the stress distribution near the ends of the beam, nor the stress disturbance near the interface. Although this solution is a good approximation for the bending stresses away from the ends, it does not address the stress singularities nor satisfy the traction-free boundary conditions. Despite the approximations, this two-dimensional solution has been used extensively as a standard for experimentally determining the difference in thermal expansion between enamel and metal [39,40,41,42,43].

## **2.1.2 Development of the End Solution**

Hess recognized the need to satisfy the boundary conditions, and superimposed a stress field on Timoshenko's two-dimensional solution that negated the traction near the ends [10]. A 30-term eigenfunction-series expansion was used to approximate the correct end condition. This solution accommodated the normal stress and shear stress distributions along the interface near the end of the bimaterial joint.

Hess [11] also found that the radii of curvature determined by the Timoshenko solution was not necessarily the same for each material, as illustrated in Figure 2. Therefore, normal stresses are required to enforce continuity at the interface and these normal stresses perpendicular to the interface could be either tensile or compressive. Consequently, tensile peel

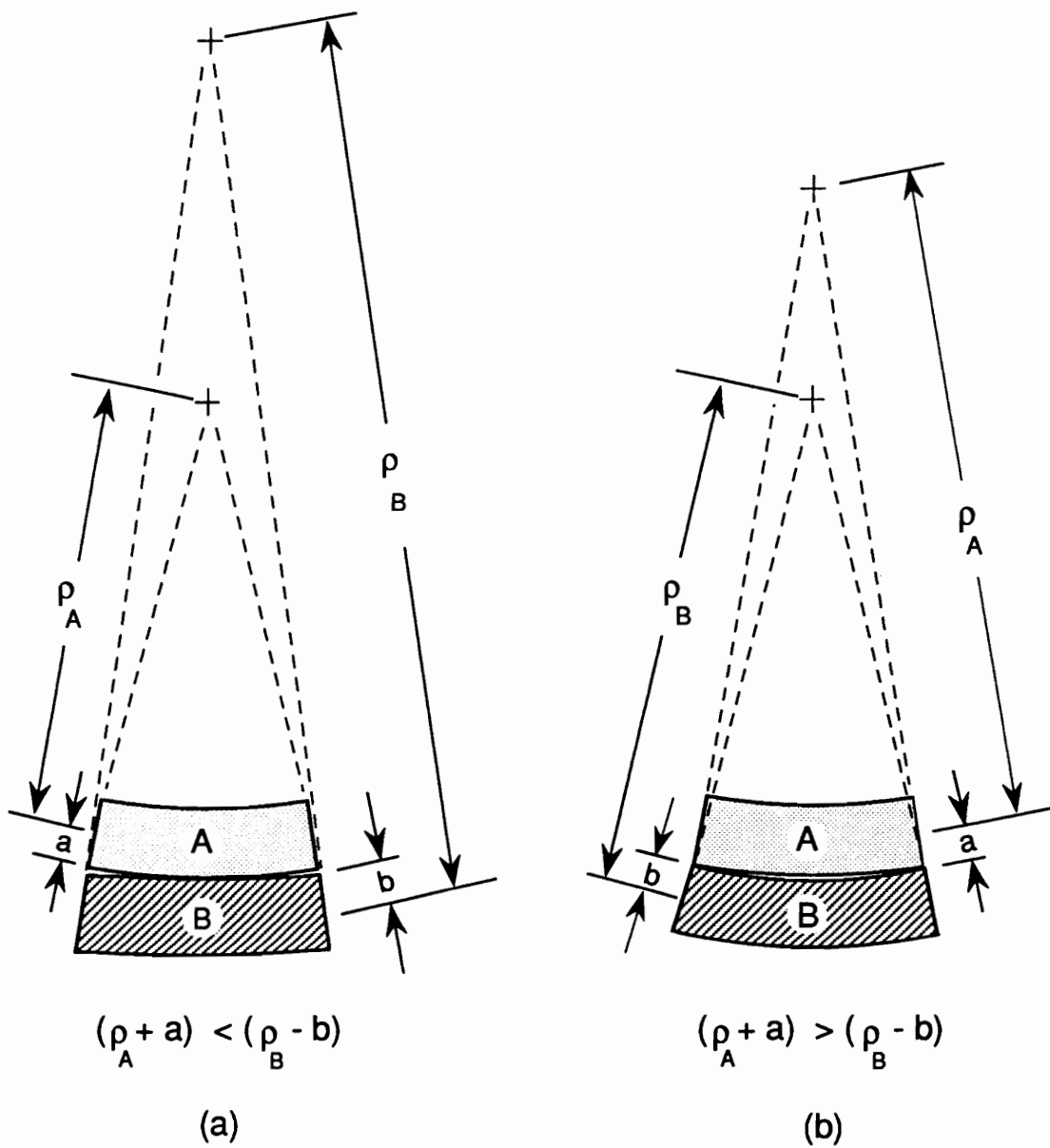


Figure 2. Radius of curvature can vary with material properties and geometry.

stresses or compressive pinch stresses are developed along the interface near the free ends of the joint.

Hess's approach was really quite clever. He basically agreed with Timoshenko's solution, but modified it to satisfy two-dimensional boundary conditions. It was a backward approach. Instead of forming a solution that directly modeled the stress distribution at the end of the beam, the approach Hess used was based on modeling the additional stresses that were needed to cancel the Timoshenko stresses near the ends of the beam. The results of Hess's parametric study are presented in reference [11].

Hess's solution actually satisfied the boundary conditions near the end of the joint, but not exactly at the end of the joint. His solution for the stress distributions at the end of the joint was unbounded, and therefore no finite prediction for the stress could be obtained. The solution implies infinite stresses there.

The stress field Hess dictates near each end of the joint includes normal and shear stresses at the interface. These components may induce delamination. It has been demonstrated by Hein, Erdogan, Bogy, and Sternberg [17,18,19,20], that this stress field will theoretically include a singularity at the end of the interface. While a singularity cannot exist in a real material, a severe stress concentration is to be anticipated.

Bogy and Sternberg [16,19] used two-dimensional elasticity to investigate singularities arising from discontinuous (normal and shear-stress) loadings applied to an arbitrary semi-infinite solid. This is similar to the discontinuous loading at a bimaterial interface. Bogy later extended this work to study bonded bimaterial half planes [20,21] using plane (plane strain and generalized plane stress) theory of elasticity. He then determined the plane solution for joined elastic semistrips by superposition of solutions for the half planes and for infinite strips [27].

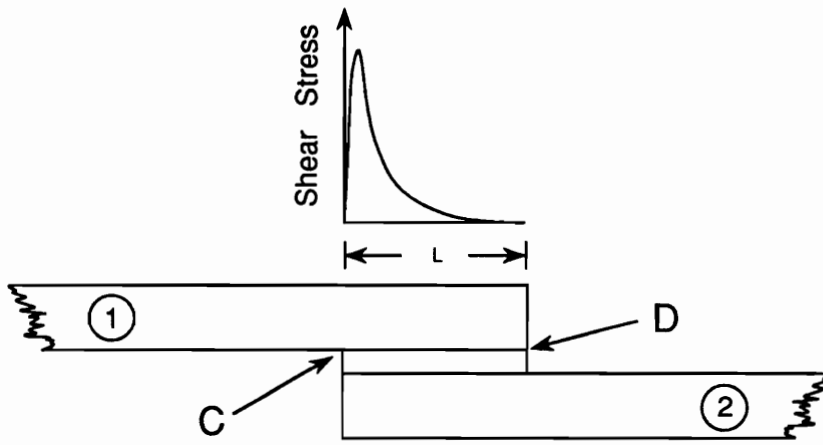
The principle of superposition allowed Bogy to solve two simpler problems, where their combined solutions satisfy the original problem. The strength of the singularity resulting from different material properties and angles of intersection was also investigated [22,23,24,25,26].

Grimado [12] also used a strength of materials approach. Unlike Timoshenko and Hess, Grimado considered the effect of the bonding material as a third layer. However, he ignored equilibrium of this third layer (the bonding layer) and the stress-free end conditions of this layer. Grimado's results show the maximum interlaminar shear stress occurs at both ends of the beam (i.e.  $\tau_{xy} \neq 0$  on the free ends). Cheng and Gerhardt [28] used two-dimensional elasticity to study this problem; here, too, the stress-free end condition is not satisfied.

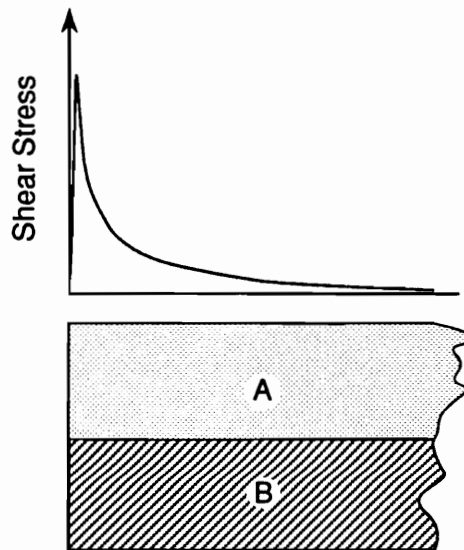
Chen, Cheng, and Gerhardt [29] expanded on this earlier (two-dimensional theory of elasticity) solution of Cheng and Gerhardt [28]. In their treatment, Chen, Cheng, and Gerhardt also used two-dimensional theory of elasticity, but in conjunction with the variational theorem of complementary energy. They developed a pair of governing differential equations that satisfy the boundary conditions concerning stress-free surfaces and stress-free ends of the beam.

### **2.1.3 Similarity with Single-Lap Joints and Previous Work**

The knowledge gained in studying adhesive lap joints may be useful in the study of bimaterial joints. The stress distribution in an adhesively-bonded single-lap joint, Figure 3(a), is very similar to the stress distribution near the end of a bimaterial interface, Figure 3(b). The strongest similarity in the two problems is the discontinuous loading at the end of the joint, where the highest shear stresses seem most likely to occur. As discussed above, Bogy and Sternberg [16,19] investigated singular stresses that result from a discontinuous loading.



(a)

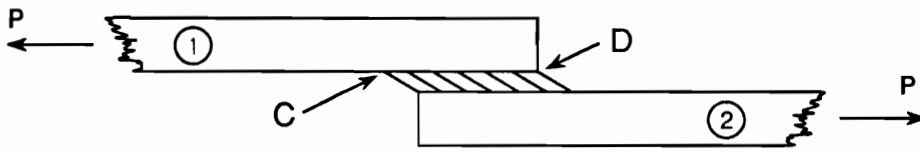


(b)

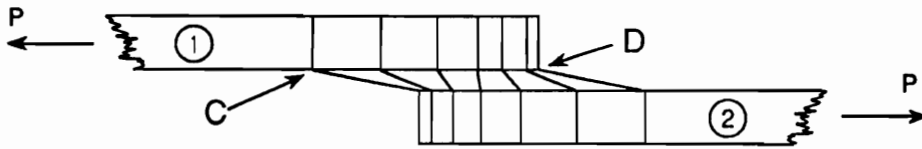
Figure 3. Singular stresses and stress distributions along the interface are similar in (a) adhesive lap joints and (b) bimaterial joints.

If the adherends are inextensible, as shown in Figure 4(a), they will move as solid blocks and the adhesive will deform rather uniformly. Although the adhesive deforms uniformly, the stress distribution will not be uniform. Each adherend carries the full load,  $P$ , until reaching the joint region, where the load is transferred to the other adherend through the adhesive. Therefore, the load carried by the inextensible adherend no. 1, is greatest at C and diminishes toward D, where it is zero. So, if the adherends are compliant, as in Figure 4(b), the greatest interface strain  $\epsilon_x$  in adherend no. 1 would occur at C and diminish toward D. Since the shear stress  $\tau_{yx}$  at A increases from zero at a finite rate, the drop in  $\epsilon_x$  is continuous. An assumption of non-zero  $\tau_{yx}$  at the end of the joint would imply a discontinuous variation of  $\epsilon_x$  and it would violate the condition of zero shear stress  $\tau_{yx}$  at the free surface.

This is the same situation facing the bimaterial problem where the elementary solution prescribes stresses at the free edge, in Figure 5(b). Neither of these models can have stresses on the free edge. Therefore, the stress distribution very near this edge must change rapidly to accommodate the free surface. This self equilibration of the stresses near the end of the joint is expected to be very similar in these two problems, as shown in Figure 3, and thus have similar solutions. Stress distributions in bonded-lap joints have been investigated analytically [2,25,51,52,53,54,55] and experimentally [56,57,58]. The experimental deformations presented by Post, et. al. [56,58] validate this rapid change near the free surface of the adhesive-lap joint that must similarly occur in the bimaterial specimen.



(a) Rigid adherends



(b) Compliant adherends

Figure 4. Adhesive deformation in a lap joint varies with material properties.

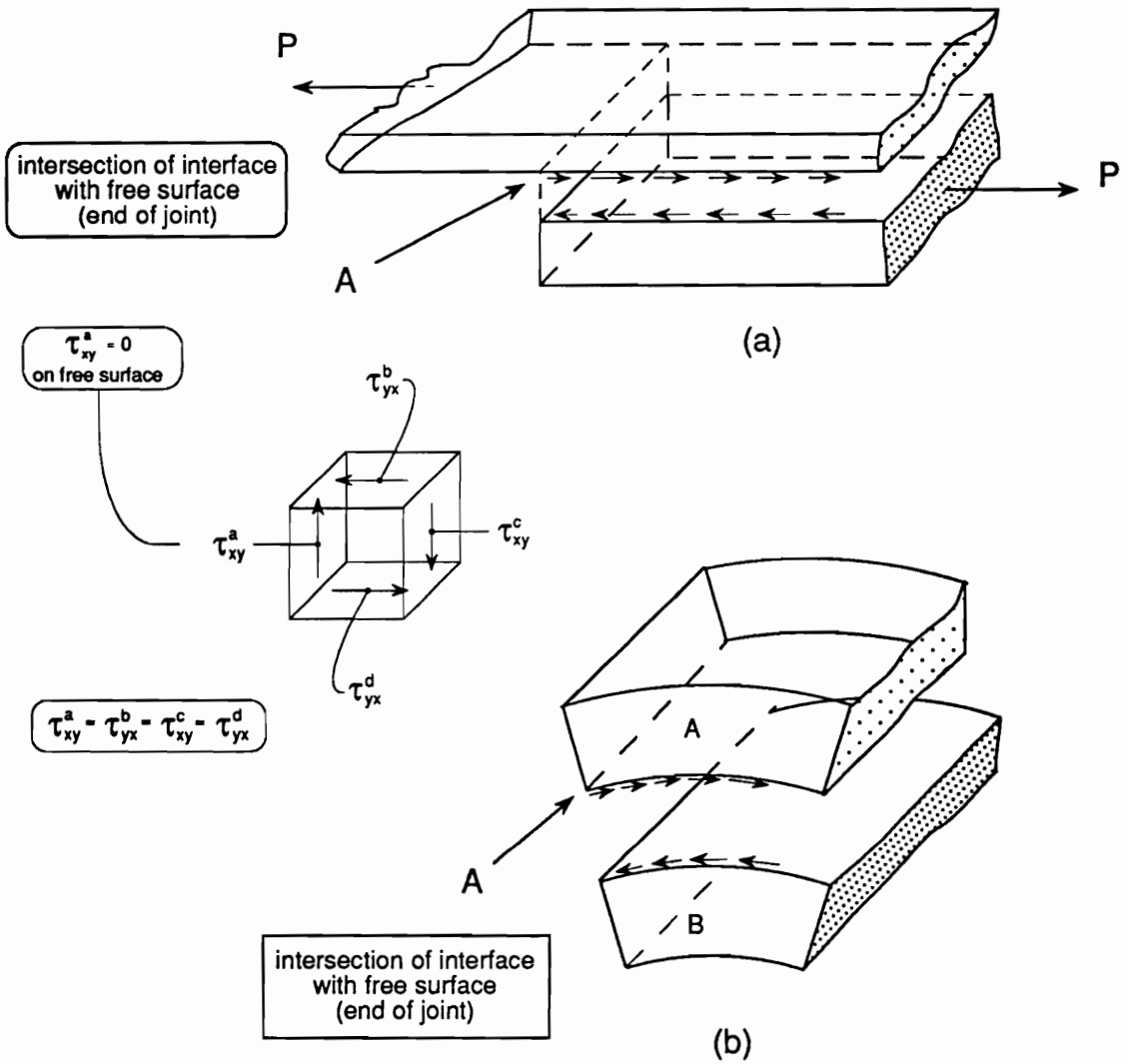


Figure 5. Interface stress distribution similarities between (a) lap joint and (b) bimaterial joint.



## 2.2 Considerations in Formulating the Problem

### 2.2.1 Three Dimensionality - (A Strength-of-Materials Approach)

Although the above solutions give meaningful insights, they are solutions to two-dimensional problems and not the real three-dimensional problem. Figure 6 illustrates why this must be solved as a three-dimensional problem. The two-dimensional approaches do not account for the thermal expansions in the third direction. This two-dimensional deformation recognizes stress singularities at the ends only (c) and assumes constant stresses through the thickness. The stresses,  $\sigma_y^{(relative)}$ , shown in Figure 6 are a qualitative representation of the  $\sigma_y$  stresses, relative to the stress at the center of the specimen interface.

Unequal thermal expansions of the two adjoining bodies create shear stresses on the joint interface. In the two-dimensional problem, illustrated in Figure 7, the  $\tau_{xy}$  interface shear stresses cause bending of unequal curvatures of the two bodies, depending on the geometry and material properties. For continuity of these two bodies, normal stresses must exist along the interface. These normal stresses depend on the geometry and material properties, which determine a peel condition (Figure 7a) or a pinch condition (Figure 7b).

The same deformations that develop  $\tau_{xy}$  stresses on the interface in the two-dimensional problem must also exist for  $\tau_{yz}$  stresses in the real, three-dimensional problem. Figure 8, illustrates the three-dimensional peel and pinch conditions.

Consequently, a three-dimensional approach (Figure 6e) will conclude that similar types of stress singularities existing at the ends of the two-dimensional joint (Figure 6c) also exist

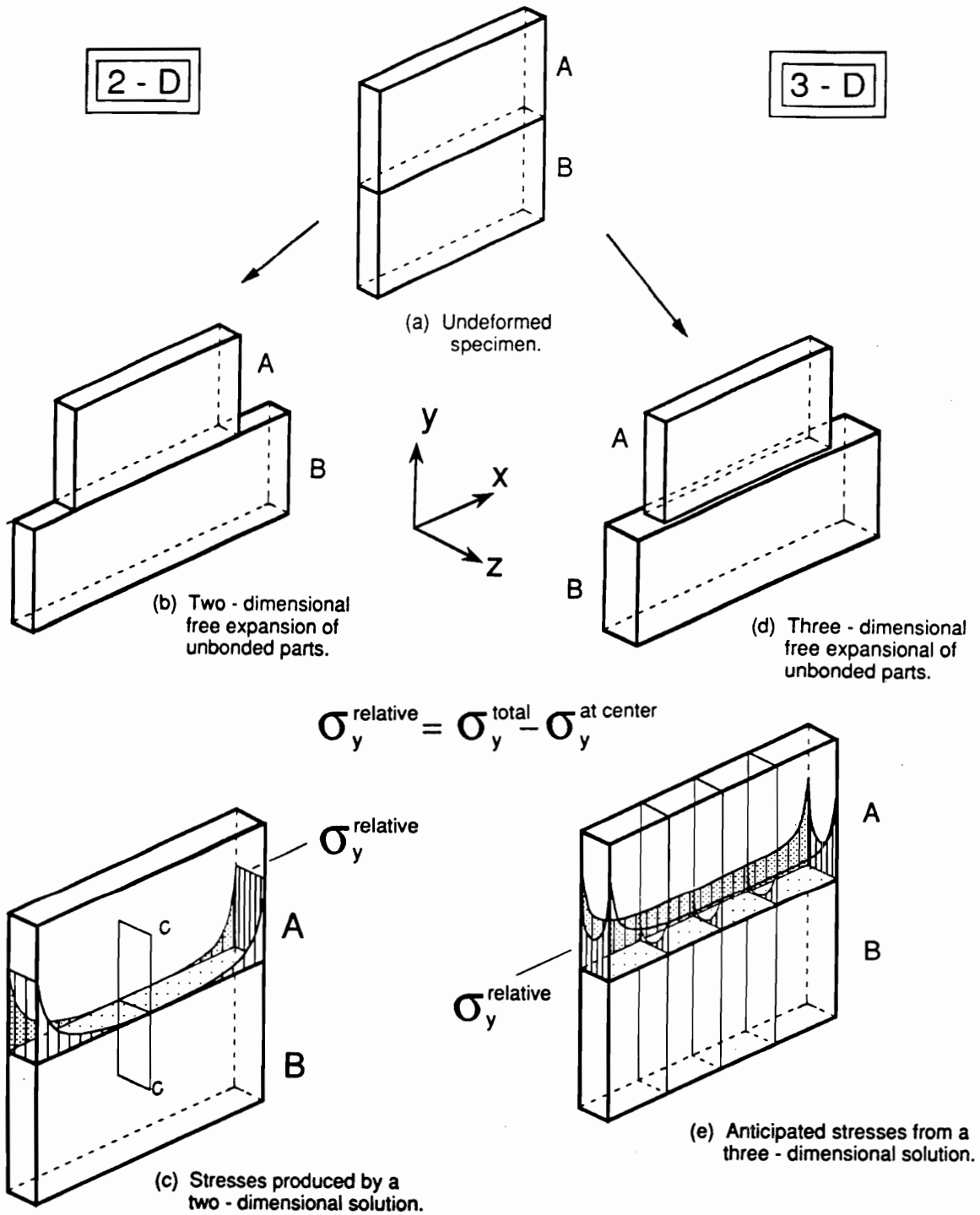


Figure 6. A comparison between deformations and stresses considered in a two - dimensional solution and in a three - dimensional solution for the mutual constraint of a bimaterial interface.

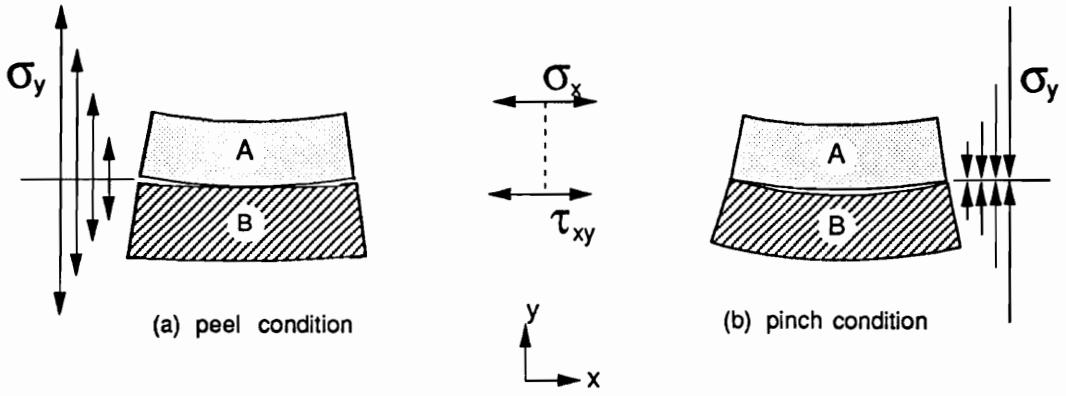


Figure 7. Two-dimensional deformations with corresponding two-dimensional stresses.

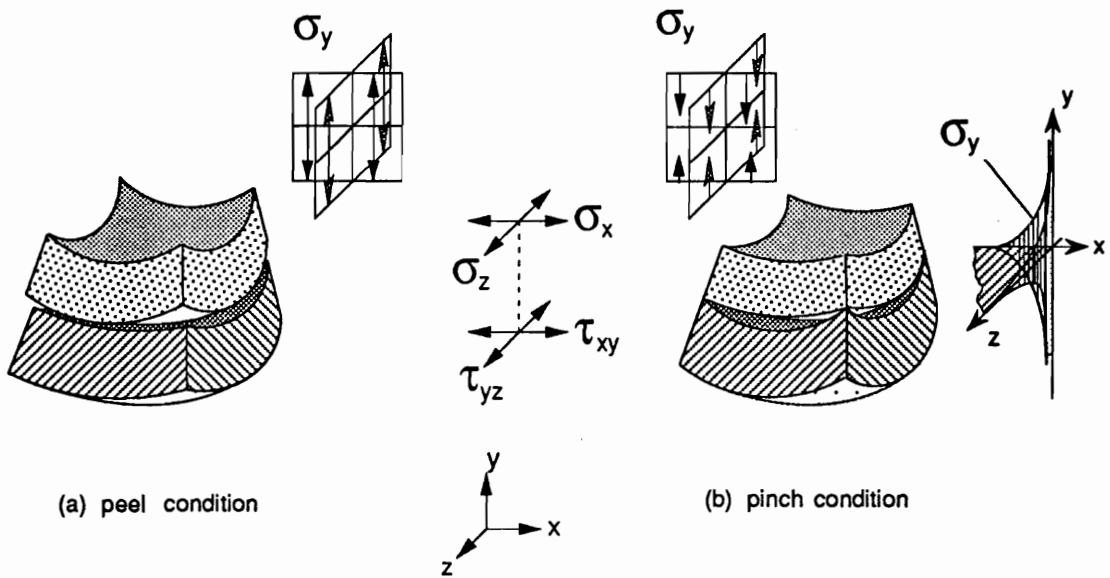


Figure 8. Three-dimensional deformations with corresponding three-dimensional stresses.

along all edges of the joint. Understanding this, it is clear that theoretical singularities exist along the entire perimeter of the joint, and the three-dimensional problem becomes very much more complex.

## 2.2.2 Inapplicability of Plane Stress and Plane Strain

Because of this complexity, most of the analytical solutions are based on the assumptions of either generalized plane stress or generalized plane strain [2,9,14,20,21,22,23,27,29], which are not realistic here. The plane-stress assumption applies to a thin plate, loaded parallel to the plane of the plate and with loads distributed uniformly across the thickness, as illustrated in Figure 9. And, if the stresses  $\sigma_x$  and  $\sigma_y$ , applied to the edge of the plate, in Figure 9 are not uniform across the thickness of the plate, but are symmetrical with respect to the middle plane of the plate, a state of generalized plane stress is said to exist. In formulating problems for this case, the field variables,  $\sigma_i$ ,  $\epsilon_i$ , and  $U_i$  are averaged across the thickness of the plate. However, in the bimaterial problem -

- (1) the interface stresses vary significantly through the plate thickness
- (2) significant shear stresses act perpendicular to the plane of the plate.

Each of these reasons indicate that the generalized plane stress-assumption should not be applied for a fully valid solution.

The plane-strain assumption applies to a long body that is loaded perpendicular to the longitudinal direction,  $x$ , illustrated in Figure 10. For the plane-strain assumption to be applicable, the body can have no displacement in the axial direction, and the load must not vary along the length (i.e. every cross-section will undergo the same deformation). However, the interface

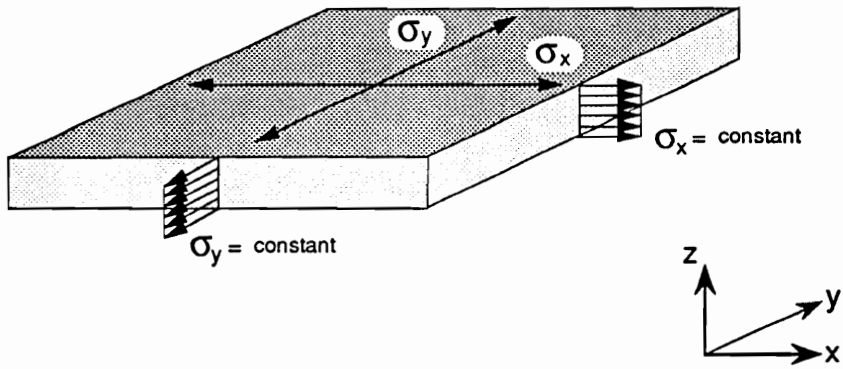


Figure 9. Plane stress problem.

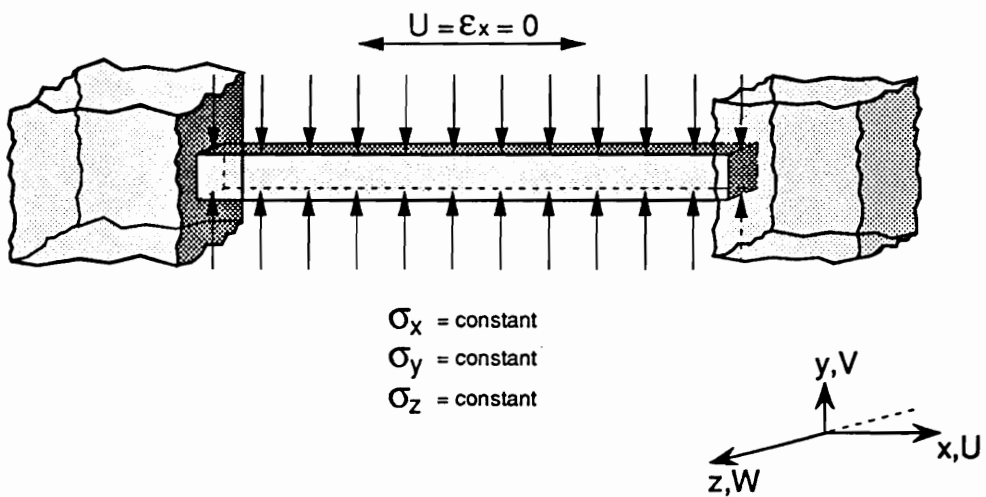


Figure 10. Plane strain problem.

shear and normal stresses along the bimaterial interface indicate that displacement and strain will occur in all three directions within the interface region of the bimaterial specimen. For these reasons, the plane-strain assumption cannot be applied. In conclusion, the shear stresses existing on the bimaterial interface (acting along the interface, perpendicular to the plane of the body) require this to be considered as a three-dimensional problem.

## **2.3 *Recent Developments***

### **2.3.1 Recent Theoretical and Numerical Solutions**

Sawa, et. al. [30] used three-dimensional elasticity to solve for the interface stresses between two dissimilar adherends in an axisymmetric adhesive butt joint of aluminum and steel. Their interest was in determining the interface stresses that may be responsible for initiating the fracture or debonding of the joint. They report that their elasticity solution correlates well with experimental results. However, the experimental (strain) data presented were taken with strain gages along a line perpendicular to the interface and extending across the interface on both sides, and the elasticity solutions (stress) are presented along the interior interface from the core to the surface. The elasticity solution presented shows singularities along the interface near the free surface. It seems unrealistic that three strain gages mounted 5-mm apart, with the closest one mounted 5-mm from the interface, could validate such a singularity.

Seo, et. al. [59], studied the three-dimensional, axisymmetric problem by the boundary element method (BEM) and the finite element method (FEM). They plotted distributions of the

stress normal to the interface along the free surface of the cylinder, where they showed tensile stresses on one side of the interface and compression on the other.

Yada, et. al. [36] investigated how the geometry of an axisymmetric-bimaterial butt joint affects the stress distribution, using a three-dimensional finite element method and varying the angle of one of the cylindrical walls. These results show the same kind of singularities presented in Sawa, et. al. [30].

Most of the interest in the bimaterial problem is concerned about the interface and free-edge/interface stresses. Most of the information found in the literature only presents stress distributions along the joint interface and not across the interface. However, Terasaki, et. al. [38] investigated the residual thermal stresses using a boundary element method (BEM) to determine the stresses along a line perpendicular to the interface of the two bonded materials. They presented the effect of various geometric ratios, shown in Figure 11. They used a plane-stress condition, which might be an appropriate assumption of the stress field away from the interface, but, it cannot be an accurate result near the interface where the critical stresses occur, where the three-dimensional effect is more significant. Instead, certain trends would be revealed. The results of Terasaki, et. al., presented in Figure 11, shows an extremely sharp transition of normal stresses from tension to compression along the free surface, across the interface. A strong stress gradient is predicted across the interface.

### **2.3.2 Correlation with Experimental Measurements**

Suganuma, et. al. [47,48], found a similar normal stress distribution experimentally, with a thermal loading. Strain gages (1-mm by 1-mm) were placed along a line perpendicular to the

Figure 11.

Stresses across the interface using a Boundary Element Method (BEM) and assuming a plane - stress condition, by Terasaki, et. al. [37].

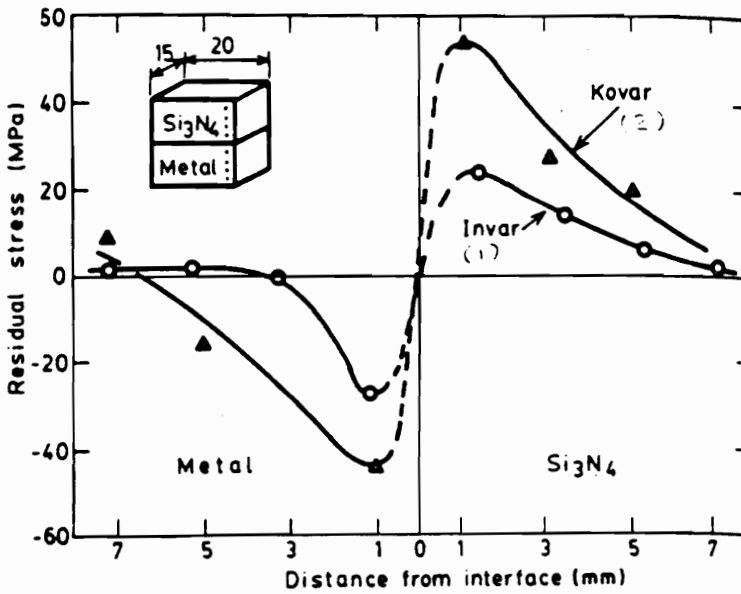
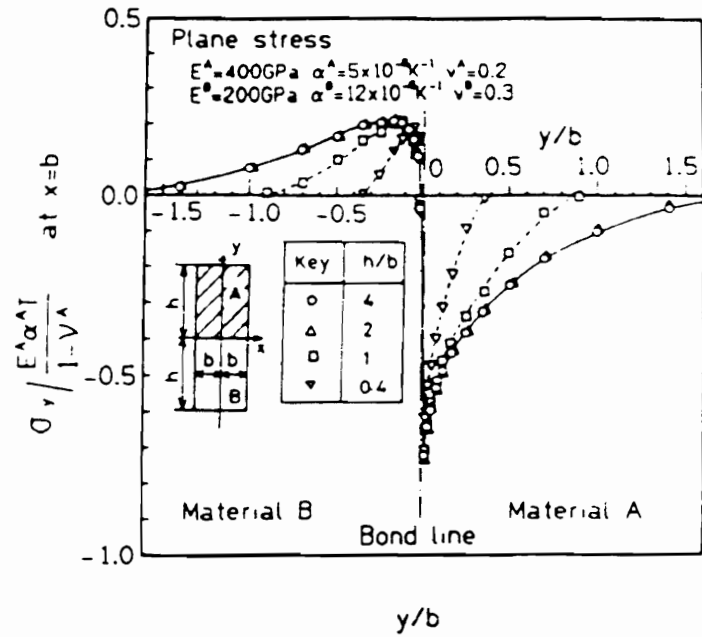


Figure 12.

Experimental Results using strain gages, by Suganuma, et. al. [47].



interface and 1 mm from the edge (or corner). The results of these experiments are shown in Figure 12 for (1) Invar bonded to silicon nitride and (2) Kovar bonded to silicon nitride. Although information closer to the interface could not be obtained, both of these results exhibit the change of sign and strong gradient presented in the BEM results of Terasaki, et al. [38]. However, the capability of strain gages is very limited for detailed analysis.

There are two important limitations to using strain gages for this problem.

- (1) The data collected represents the average strain in the area contacted by the strain gage. Thus, measurements made in zones of rapid change are inaccurate.
- (2) The size of the gage limits how close it can be placed to a specific point.

These limitations are apparent in the experimental results shown in Figure 12, where the closest measurements were 1-mm from the interface. In addition, the strains recorded are the average (not peak) values occurring in the area of the gage.

## **2.4 Applications**

### **2.4.1 Application to Composites**

The composites community is also concerned about this same three-dimensional problem, calling it "free-edge effects." This free-edge effect is thought to cause theoretical singular stresses in a composite laminate everywhere a cross-ply or angle-ply interface intersects a free edge. These free-edge stresses may be large and can greatly reduce the strength of the laminate [60,61]. Free-edge stresses can be caused by fabrication (curing stresses) [62] and

thermal changes [63] as well as by mechanical loading [64]. Although the magnitudes will vary, these stresses will exist regardless of joint geometry or what dissimilar materials are involved. For this reason, there has been a lot of emphasis given to determining the stress distribution in the edge region. This region borders the free edge and extends into the composite along the interface. The inward distance is small, typically only a few ply thicknesses.

The composite free-edge problem is actually a special application of the more general bimaterial joint problem discussed above. The composite contains many bimaterial interfaces between plies, but also introduces the added complexities of anisotropic materials and the influence of nearby plies on the stress fields.

**Table 2. Additional approaches used to determine the interface-stress distribution in a composite-free-edge problem.**

	<u>References</u>
1. Elasticity .....	[65,66,67,68,69,70,71,72,73,74]
2. Approximate Analytical Methods .....	[75,76,77,78]
Eigenfunction and Fourier Series approximations (2-D) .....	[73,74,79]
3. Finite Element Methods .....	[60,61,63,80,81,82,83,84,85,86,87]
Boundary Element Methods (2-D, and 3-D) .....	[88,89]
Finite Difference Methods .....	[66,90]
4. Experimental Methods .....	[91-117]

Solutions to the composite free-edge problem have evolved in ways analogous to the work of Timoshenko and Hess, described above. Similar to Timoshenko’s bimaterial strip solution, lamination theory also implies boundary tractions on a free edge - which cannot exist [65,91,118,119,120]. Analogous to the Hess approach, several solutions have emerged to determine the interlaminar stress distribution required to satisfy the free-edge boundary conditions. Approaches that have been used to determine the interlaminar stress distribution are given in Table 2. In [111], Guo, et. al., measured interface strains in laminated composites

under compression, revealing  $\varepsilon_y$  strain concentrations on the free surface and extremely strong  $\varepsilon_y$  gradients in the interface region;  $\varepsilon_y$  is the strain perpendicular to the interface.

## **2.4.2 Other applications of this problem**

There are many applications in which the bimaterial mechanics problem is a dominant issue. Some of these are listed in Table 3, with pertinent literature references.

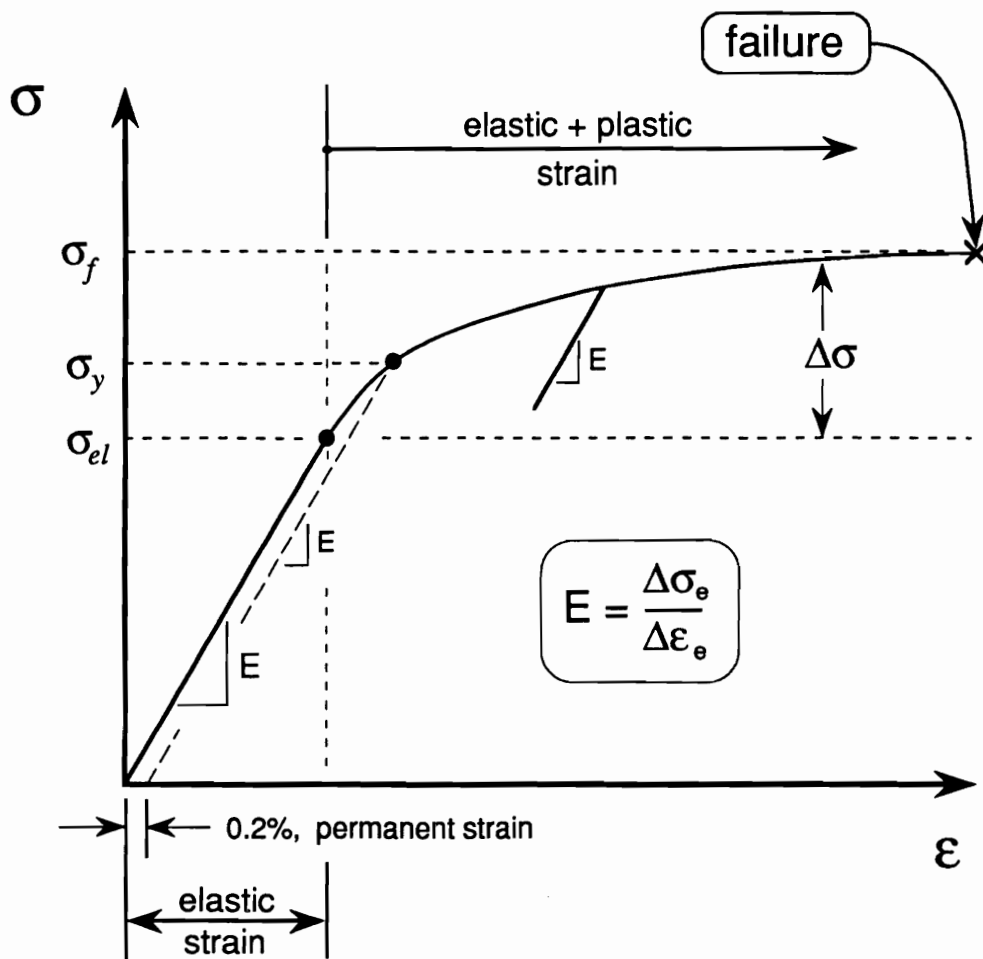
## **2.4.3 Interface Stresses and Plasticity**

It has been shown above, that the stress field near a bimaterial interface is very complex, with predicted singular stresses near the bimaterial interface (see Figure 11). Singular or infinite stresses, however, cannot exist in reality because a given material will either yield or fracture. A ductile material yields and spreads the load over a larger region. It is assumed that yielding occurs near the bimaterial interface.

The mechanical properties of ductile materials change when they are strained beyond the elastic range. For strain-hardening metals, an ever-increasing stress is needed to produce further yielding, as indicated in Figure 13. This is the result of dislocation interaction from the localized stresses surrounding the dislocations. The magnitude of these particular stresses cannot be measured directly, but may be estimated through the theory of elasticity.

**Table 3. Applications of the bimaterial problem.**

	<u>References</u>
1. Composite Materials .....	[60,61,63,64,65,91,111,118,119,120,121,122]
(edge-effects) .....	[62,63,64,68,75,77,79,83,84,85,86,90,93,94,95,121,123,124,125,126,127]
(interface stresses and delamination) .....	[50,60,61,62,65,66,67,68,76,78,79,81,82,85]
.....	[91,92,96,102,109,111,118,120,122,126,128,129,130,131,132,133]
(fiber/matrix bond-interface stresses) .....	[122,134,135]
2. Seals	
(ceramic/metal) .....	[44,46,47,48,59,123,136,137,138,139,140,141,142]
(glass/ceramic) .....	[143,144,145]
(glass/metal) .....	[146,147]
(other) .....	[9,34]
3. Porcelain Enamel on Sheet Iron .....	[39,40,41,42,43,97,98,100,148,149,150,151]
(and other coatings) .....	[43,100,152]
4. Brazed and Welded Joints .....	[44,87,123,153]
5. Microelectronics Industry Applications .....	[5,6,145,154,155,156]
(thin films on substrates) .....	[152]
(ceramic-to-metal joining) .....	[44,46,59,138,139,140]
(packaging, circuit boards, etc.) .....	[154,155]
6. Adhesives . [2,53,80,102,105,151,157,163,164,169,170,171,172,173,174,175,176,177,178,179,180]	
(surface chemistry) .....	[134,157,158]
(butt joints) .....	[40,49,69,101,128,159,160,161,162,163]
(lap joints) .....	[40,51,52,54,55,56,57,102,164,165,166,167]
7. Laminated Beams .....	[29,45,49,50,53,58,68,79,126,128,131,169,171,181,182,183]
8. Transition Interlayers .....	[79,101,129,137,142,147,153,156,161,184,185]
9. Stress corrosion cracking .....	[87,157,186,187,188]
10. Residual Stress .....	[50,103,104,126,138,139,140,153,157,161,165,167,171,174,181,184,189]
11. Bimaterial Interfaces	
(crack propagation) .....	[79,88,89,157,161,171,180,190,191,192,193]
(interface flaws) .....	[79]
(dislocations) .....	[152,194,195,196,199]
(residual stresses and Plasticity) .....	[49,59,88,105,107,111,124,126,127,130,133,134,138]
.....	[139,140,143,144,145,151,157,158,162,163,165,171,172,173]
.....	[174,179,183,187,188,191,192,194,195,196,197,198,199,200]
12. Strength Evaluation of a Bimaterial Joint	
(stress and strength evaluation) [61,80,118,122,126,127,141,143,172,177,185,199,201,202,203]	
(failure) .....	[154,175,203]
13. Mathematical Singularities	
(singular solutions) .....	[49,64,70,71,79,95,126,130,151,167,168,177,180,190]
.....	[197,199,204,205,206,207,208,209,210,211,212,213,214]
(mathematical models) .....	[49,53,70,71,80,81,82,95,126,130,131,134,151,154,157,167,168,179]
.....	[189,195,197,204,205,206,207,208,209,210,211,213,215,216,217,218,219,220,221,222,223]
(effect of geometry) .....	[49,70,80,91,119,140,166,209,210,211,212,213,214]



$\sigma_{el}$  = elastic limit

$\sigma_y$  = yield strength, usually defined as 0.2% strain offset, i.e. 0.2% permanent strain.

$\sigma_f$  = failure

$E$  = (or Young's Modulus) is assumed to be linear, and is determined by the slope of the stress-strain curve below  $\sigma_{el}$

Figure 13. Stress - strain behavior of a strain-hardening material.

## **2.5 Background Summary**

From the above analyses, we can conclude that there is a critical region of stress concentration, which exists along the entire perimeter of the bimaterial interface. This region is near the line of intersection of the interface with the free surface of the composite body, or "critical line." In addition, it follows that the stress concentrations along a "critical line" are further increased in the region where two "critical lines" intersect, i.e. at the corners. These critical regions of stress concentration exist at any bimaterial interface, regardless of the type of loading (thermal or mechanical, static or dynamic), regardless of materials (flexible or stiff, elastic or plastic), and regardless of geometry.

In earlier studies, this line of intersection of the interface with the free surface (or "critical line") was avoided entirely (Timoshenko's solution). In later studies, this region was treated as one exhibiting singular stresses (Hess). However, the analyses are typified as plane solutions, which model the critical region at the end of the specimen, but ignore the "critical line" along the face of the specimen.

More information is needed to better understand the actual stresses acting in this region. Severe stress gradients are anticipated as a result of singular or free-edge effects. Experimental documentation is needed to characterize and model the three-dimensional nature of those effects.

## **Chapter 3**

### **Chapter 3: Experimental Investigation**

#### ***3.1 Specimen Material and Geometry***

The following research was designed to produce a detailed knowledge of the thermally-induced surface deformation in the interface region of the bimaterial joint. The specimen geometry and experimental conditions are shown in Figure 14 for Specimen A, the primary specimen studied.

From the previous work seen in the literature [6,9,10,11,30,36,38,47,48,49], the stress distributions are greatly influenced by the geometric aspect ratio. For this reason, two other geometries were also studied to compare the influence of aspect ratio on the thermally-induced deformation and corresponding stress distributions. The geometry of Specimen A was chosen

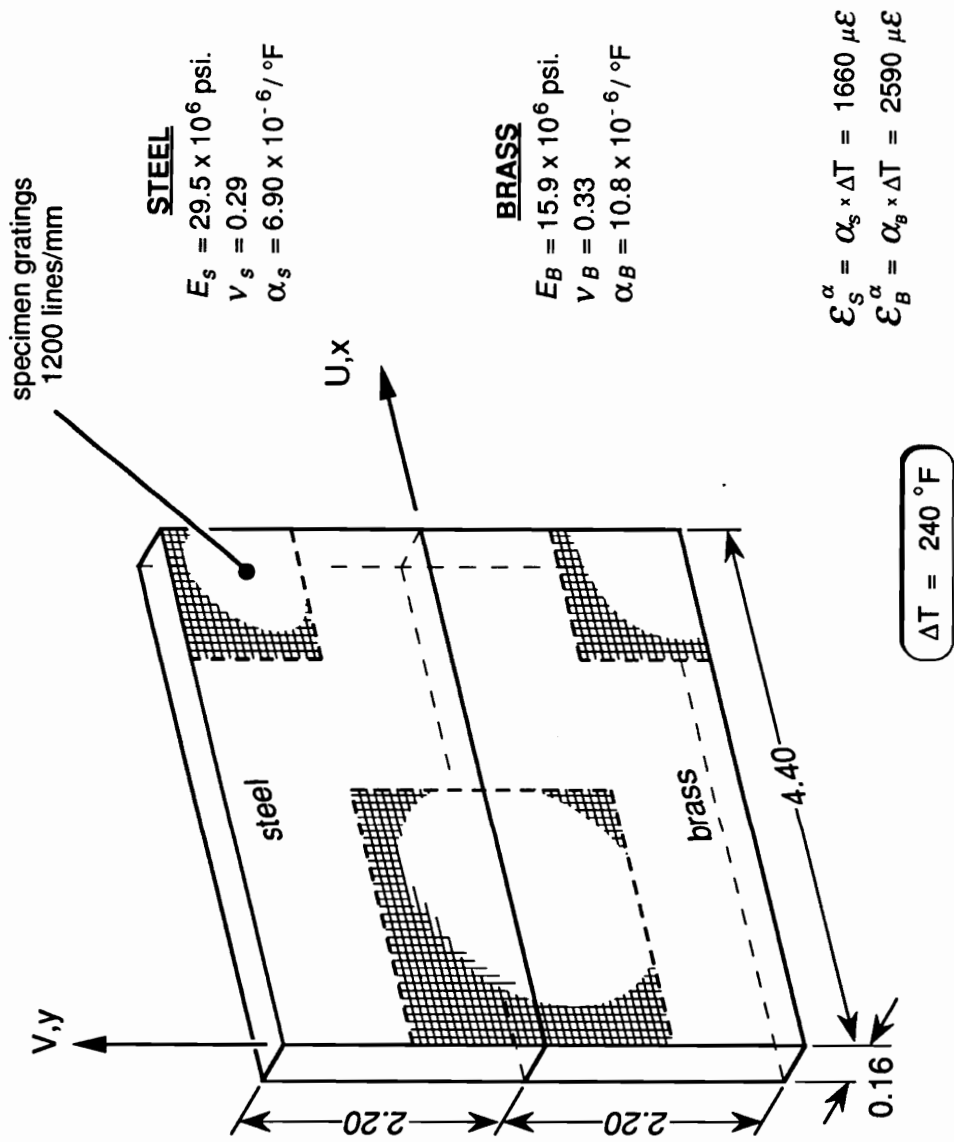


Figure 14. Specimen A: Geometry, material properties, and temperature increment.



as the primary specimen for interrogating this problem because this geometry had the longest length of interface (dimension "b" in Figure 15, below, as well as the greatest aspect ratios,  $a/c$ , and  $b/c$ . (Also, see Table 4.)

These two other specimen geometries, along with the primary specimen (Specimen-A), are shown in Figure 16. The corresponding aspect ratios are given below, in Table 4, and the material properties are given in Table 5. The dimensions a, b, and c, correlate to Figure 15, below. The shaded surface correlates to the surface interrogated by moiré interferometry and reported, here.

**Table 4. Specimen geometric aspect ratios.**

Specimen	Aspect Ratio		
	$a/b$	$a/c$	$b/c$
A	0.50	13.5	27.1
B	0.50	0.50	1.00
C	6.77	0.25	0.037
D	0.50	6.85	13.8

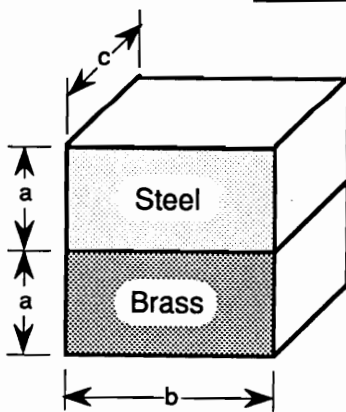


**Figure 15. Relative orientation of specimen dimensions.**

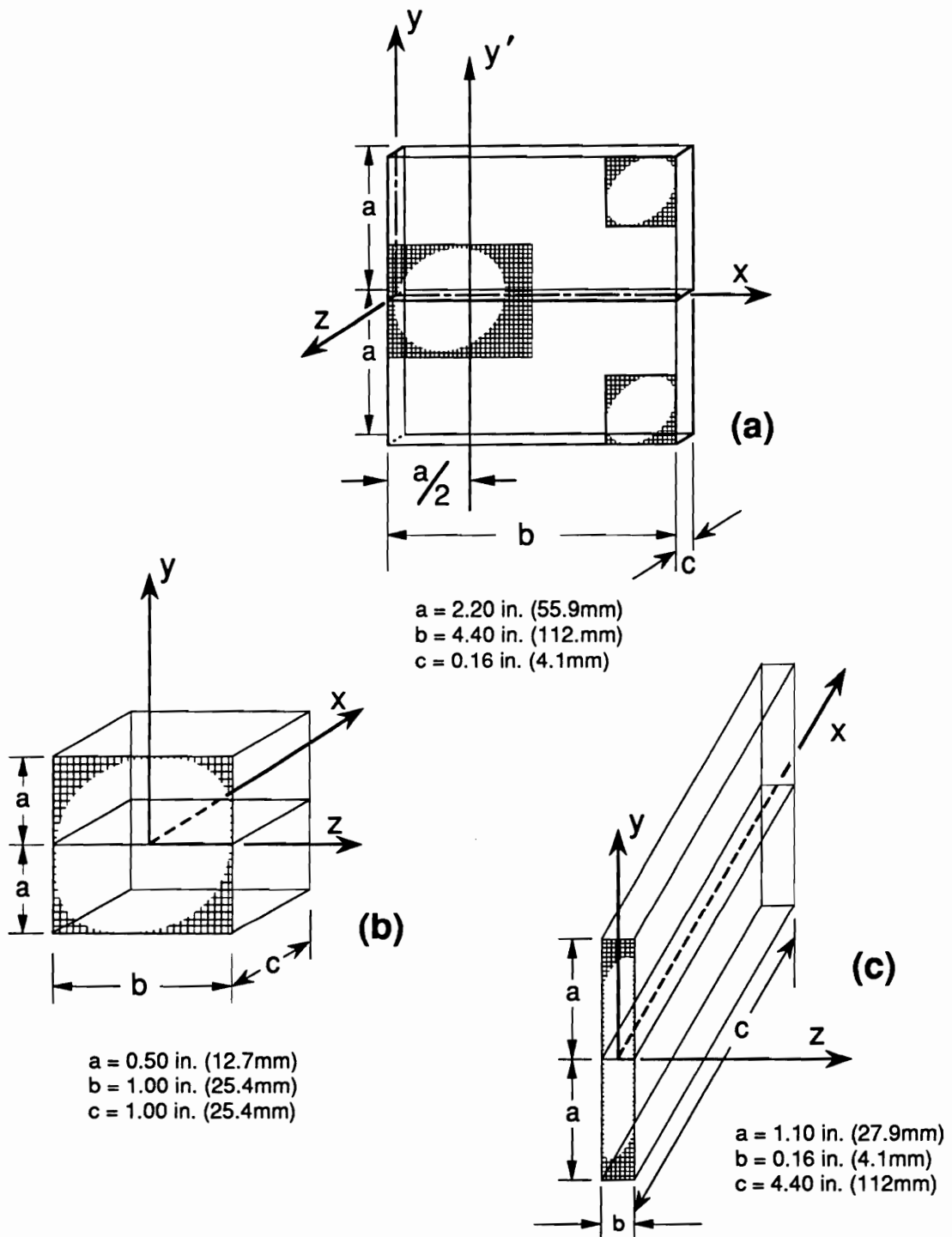


Figure 16. Specimen geometries and material properties for specimens: (a) A, (b) B, and (c) C. Note: U, V, and W are displacement components in the x, y, and z directions, respectively.

Table 5. Specimen material properties.

<b>STEEL</b>	<b>BRASS</b>
$E_S = 29.5 \times 10^6 \text{ psi.}$	$E_B = 15.9 \times 10^6 \text{ psi.}$
$\nu_S = 0.29$	$\nu_B = 0.33$
$\alpha_S = 6.90 \times 10^{-6} / ^\circ\text{F}$	$\alpha_B = 10.8 \times 10^{-6} / ^\circ\text{F}$

Two specimens (a bimaterial plate and a bimaterial cube) were made from the same stock of brass and steel. After it had been tested, Specimen-A (Figure 16a) was cut to make Specimen-C (Figure 16c). And similarly, after testing, Specimen-C was cut to make Specimen-D (Figure 17), i.e., Specimen-A and Specimen-C, (Figure 16a and c), and Specimen-D (Figure 17), are all from the same original specimen. The thermally-induced deformation in the interface region of Specimen-A, was investigated by the experimental method of moiré interferometry [108], which is described in the following sections. (This traditional method of moiré interferometry will be referred to, here, as *macroscopic moiré interferometry*.)

This investigation of Specimen-A, using *macroscopic moiré interferometry*, revealed extremely strong gradients in the immediate vicinity of the interface, a very narrow zone where the paths of the fringes were inconclusive. Therefore, in order to clearly define the deformation in this region, additional experimental evidence was sought by the higher-sensitivity method of *microscopic moiré interferometry* [116,117], using Specimen D.

The brass and steel were joined by a very thin continuous film of high-temperature silver solder. Each specimen was tested over approximately the same temperature increment,

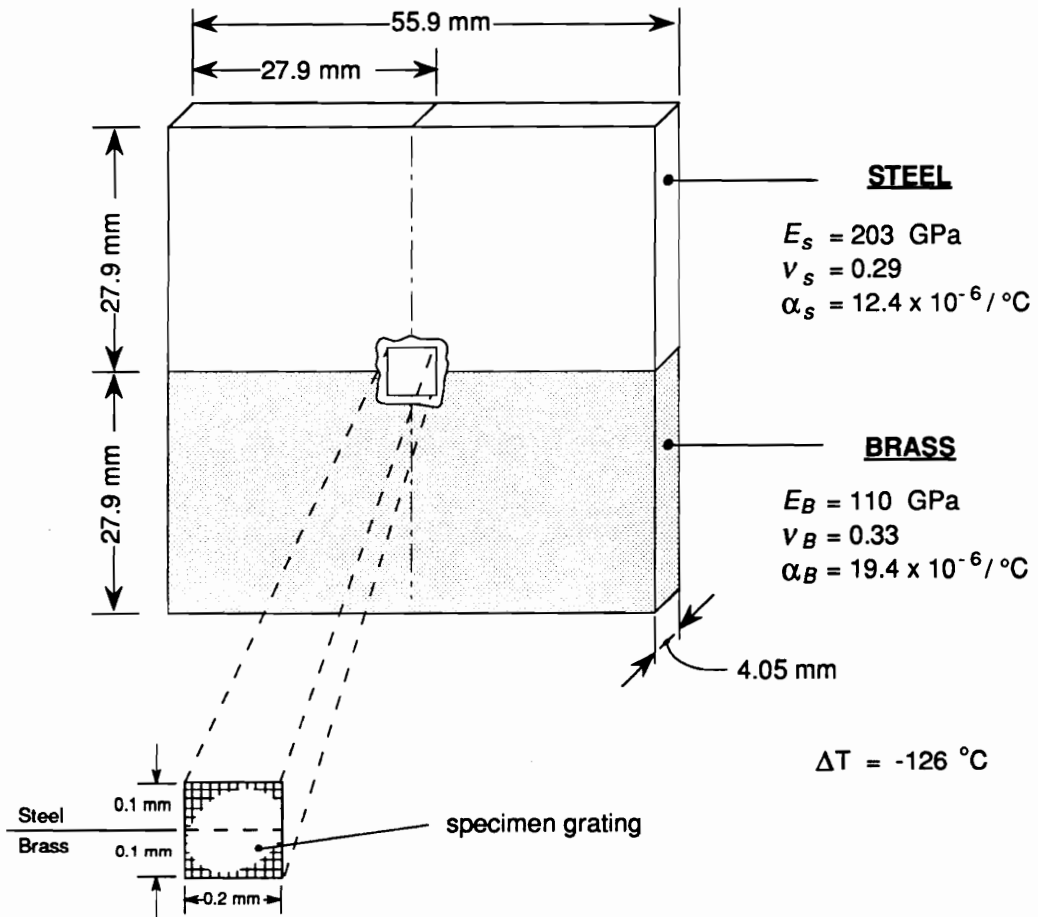


Figure 17. Specimen - D, specimen grating, and material properties.

$\Delta T$ . Temperature increments, free-thermal expansion, and corresponding coefficients of thermal expansion, for each of the specimens tested, are given later in Table 7 on page 55. The aspect ratios are given in Table 4 and the material properties are given in Table 5 for all four specimens.

## **3.2 *The Experimental Method: Moiré Interferometry***

### **3.2.1 Introduction**

The stress distributions were investigated by using the experimental method of moiré interferometry [108]. Moiré interferometry is an optical technique utilizing two-beam optical interference to produce interference fringe patterns which are full-field contour maps of in-plane displacements. It can be applied to measure deformations in almost any engineering material. With its very high sensitivity, the method produces a great abundance of displacement information. Therefore strains can be determined with high accuracy and stresses can be calculated from the strains.

This technique can be used to analyze both homogeneous and non-homogeneous, linear and non-linear deformations. This broad capability enables determination of both elastic strains and plastic strains in different regions of the same field on the same specimen, which is an important asset for this problem, since it was thought that localized plasticity could occur.

Analytical models predict singular or infinite stresses at the interface of two dissimilar homogeneous-elastic materials. This indicates that yielding might occur at the interface in the

real material having the lower yield strength. Very high strain gradients are also predicted in this region adjacent to the interface, but the experimental method of moiré interferometry can cope with extremely high gradients.

### 3.2.2 Moiré Interferometry - the Basic Principle

Moiré interferometry [108] is typically practiced at room temperature by replicating a high-frequency specimen grating on the surface of the specimen. When the specimen is loaded, the grating deforms together with the underlying specimen. A fixed reference grating is superimposed on the specimen grating. The reference grating is usually formed by the intersection of two coherent beams and is twice the initial frequency of the specimen grating. The result is a moiré pattern, which is formed by interaction of the specimen grating and reference grating. The frequency of the virtual reference grating (2400  $\ell/\text{mm}$ ) is adjusted to twice that of the specimen grating, thus producing a null field before the specimen is loaded. Then, when the specimen is loaded, the displacement  $U$  (or  $V$ ) of every point is mapped by the moiré fringe pattern and interpreted by

$$U = \frac{1}{f} N_x, \quad V = \frac{1}{f} N_y \quad (1)$$

where  $N_x$  and  $N_y$  are fringe orders at the corresponding point, and  $f$  is the frequency of the reference grating. This room temperature application of moiré interferometry was adapted for use at elevated temperatures by the method described below. Governing equations for the thermal-strain problem are given in Table 6 on page 51, and described in that section.

### 3.3 Experimental Procedure

Crossed-line diffraction gratings (i.e. with furrows in orthogonal x and y directions) were replicated on each of the bimaterial (steel/brass) specimens at an elevated temperature. A reference mold with known grating frequencies was used to replicate epoxy gratings on the specimen on the interface as well as the free corners, as illustrated in Figure 14. This left crossed-line gratings imprinted in epoxy on the specimen surface. When cooled to room temperature, the specimen and overlying grating deformed as a result of (a) the free thermal contraction of the steel and brass and (b) the state of stress caused by the mutual constraint along the joint interface. The gratings that straddled the interface deformed as a result of both effects, while the gratings near the traction-free corners experienced only the thermal contractions; the latter were used to measure the coefficients of (stress-free) thermal expansion for each of two materials.

Moiré interferometry [108] was used to record the U and V displacements at each point in the gratings, i.e., the displacement components in the x and y directions, respectively. The experimental data were received as fringe patterns that represented whole-field contour maps of the displacement fields. The displacement sensitivity was  $0.417 \mu\text{m}$  ( $16.4 \mu\text{in.}$ ) per fringe order, corresponding to moiré with  $2400 \text{ lines/mm}$  ( $60,960 \text{ lines/in.}$ ), i.e., twice the initial specimen grating frequency [108]. (This is the value of  $f$ , used in the equations given in Table 6 on page 51, and is defined as  $f_0$ , given in the list of symbol definitions.) In the course of the experiments, carrier fringes [110] were used to emphasize features of the deformation field. In addition, a special technique (whereby carrier fringes canceled the uniform deformation fringes of free thermal contraction) was applied to produce a pattern that represented the stress-induced displacements, alone [99].

Moiré interferometry measures the deformations incurred between the application of the grating to the specimen and the subsequent observation of the deformed grating. Thus, the measurements are independent of the state of residual stresses in the specimen, except to the extent that the residual stresses might influence the mechanical and thermal properties of the material. In this analysis, the material properties were assumed to be constant through each element, brass and steel, although the residual stresses from fabrication of the specimen are concentrated near the interface.

This method is described below, in greater detail.

### **3.3.1 Method for Absolute Thermal Strain Measurements**

The basic idea is simple. A special grating mold is made on a zero-expansion substrate so that it has the same frequency at room temperature and elevated temperature. This mold is used to cast (or replicate) a specimen grating at elevated temperature. It is also used (directly or indirectly) to adjust the frequency of the virtual reference grating. Accordingly, the frequency of the reference grating is fixed at twice the frequency that the specimen grating previously had at the elevated (replication) temperature. Then, the absolute change of specimen grating frequency, induced by cooling the specimen, is recorded in the moiré pattern.

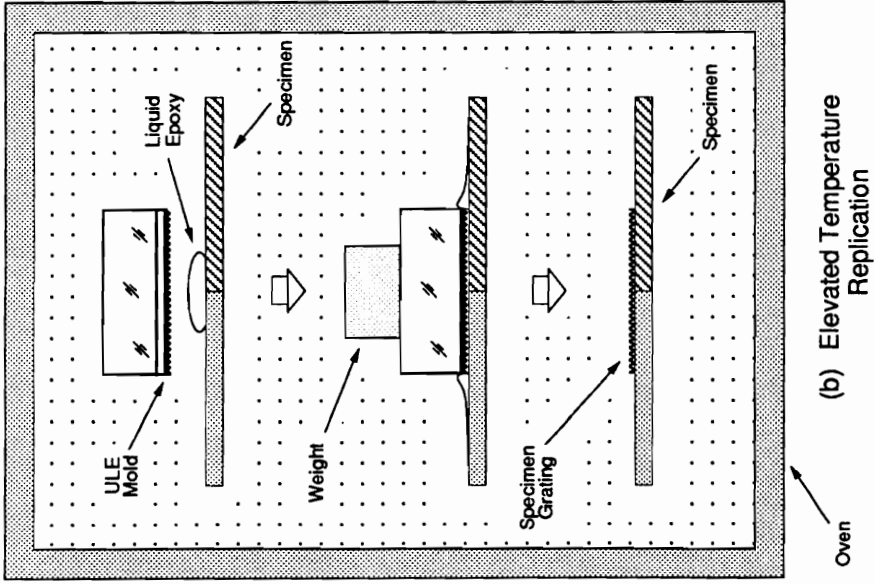


### 3.3.2 Zero-expansion Mold

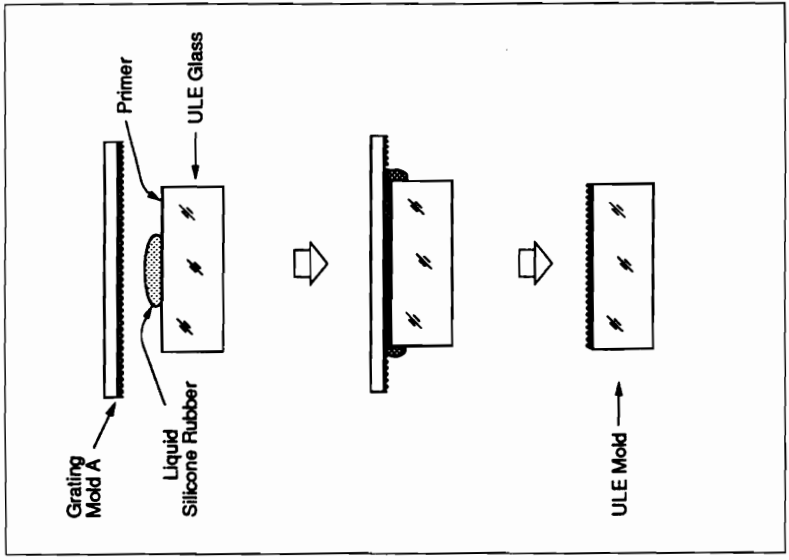
A grating mold is produced (replicated) on a (nearly) zero-expansion substrate. This procedure is illustrated in Figure 18(a). The normal grating mold on a glass substrate, marked *grating mold A*, is obtained. (It is made for example by the methods described in Ref. 108.) This grating is replicated in silicone rubber on the zero-expansion substrate at room temperature.

The substrate used here is a one-inch thick Ultra-low Expansion (ULE) glass plate, marketed by Corning Glass Works. In the temperature range 75-315°F, its coefficient of thermal expansion is  $5 \times 10^{-8}/^{\circ}\text{F}$ , which is sufficiently low to be considered zero for most applications. In special cases where the error might be significant, a correction can be introduced in strain calculations. The thermal expansion of this particular substrate was measured by interferometry by Bowles [109] to confirm that it fell within the Corning specifications.

To make the ULE mold, the substrate was coated with primer (Dow Corning 9-2023) to enable the silicone rubber to adhere to it. A small pool of liquid silicone rubber (Sylgard 184 by Dow Corning) was poured on the ULE plate and squeezed into a thin film by *grating mold A* (Figure 18a). The silicone rubber cured to a solid in 24 hours. The excess rubber was then trimmed away and *mold A* was pried off. This produced the zero-expansion mold, which is the ULE substrate with a thin (0.001 in.) silicone rubber grating on one surface.



(b) Elevated Temperature Replication



(a) Room Temperature Replication

Figure 18. Procedure to produce (a) the zero-expansion mold and (b) the specimen grating. ULE glass is an ultra-low expansion substrate. The grating is replicated on the specimen at elevated temperature in an oven.

### 3.3.3 Specimen Grating, Elevated Temperature

Figure 18(b) illustrates the process for producing the specimen grating at elevated temperature. The method is similar to the room-temperature procedure described above, but the grating is cast in epoxy instead of silicone rubber. The ULE mold and the metal specimen were preheated to 315°F in an oven. A small pool of liquid epoxy (Epon 828 with 36.5-percent hardener DDS) was poured on the specimen. The ULE mold was lowered onto the epoxy and a weight producing a force of about 0.2 pounds per square inch was added. The assembly was maintained at 315°F in the oven. The epoxy cured to a solid in about 1.5 hours, which eliminated the effects of a thermal gradient caused by the necessary oven door opening during replication. After six hours, the ULE mold was pried off and the specimen was slowly cooled to room temperature. A virtue of using silicone rubber for the zero-expansion mold is that epoxy will not adhere to it. Finally, an ultra-thin film of aluminum was applied to the epoxy surface by vacuum deposition to produce a reflective specimen grating.

### 3.3.4 Optical Apparatus and Virtual Reference Grating

The four-beam moiré interferometry apparatus [108] illustrated in Figure 19 was used. The light source used here, was produced by an argon-ion laser, using 200mW of power and a wavelength of 514.5 nm ( $\lambda = 514.5 \text{ nm}$ ). A virtual reference grating was formed by light from sections A' and B' of the incoming collimated beam, which were intercepted and redirected by mirrors A and B. Intersection of these sub-beams generated the virtual reference grating for the V field. The angle of intersection determines the frequency of the virtual reference grating and it was adjusted by fine thumbscrews on the mirror mountings. Similarly, the

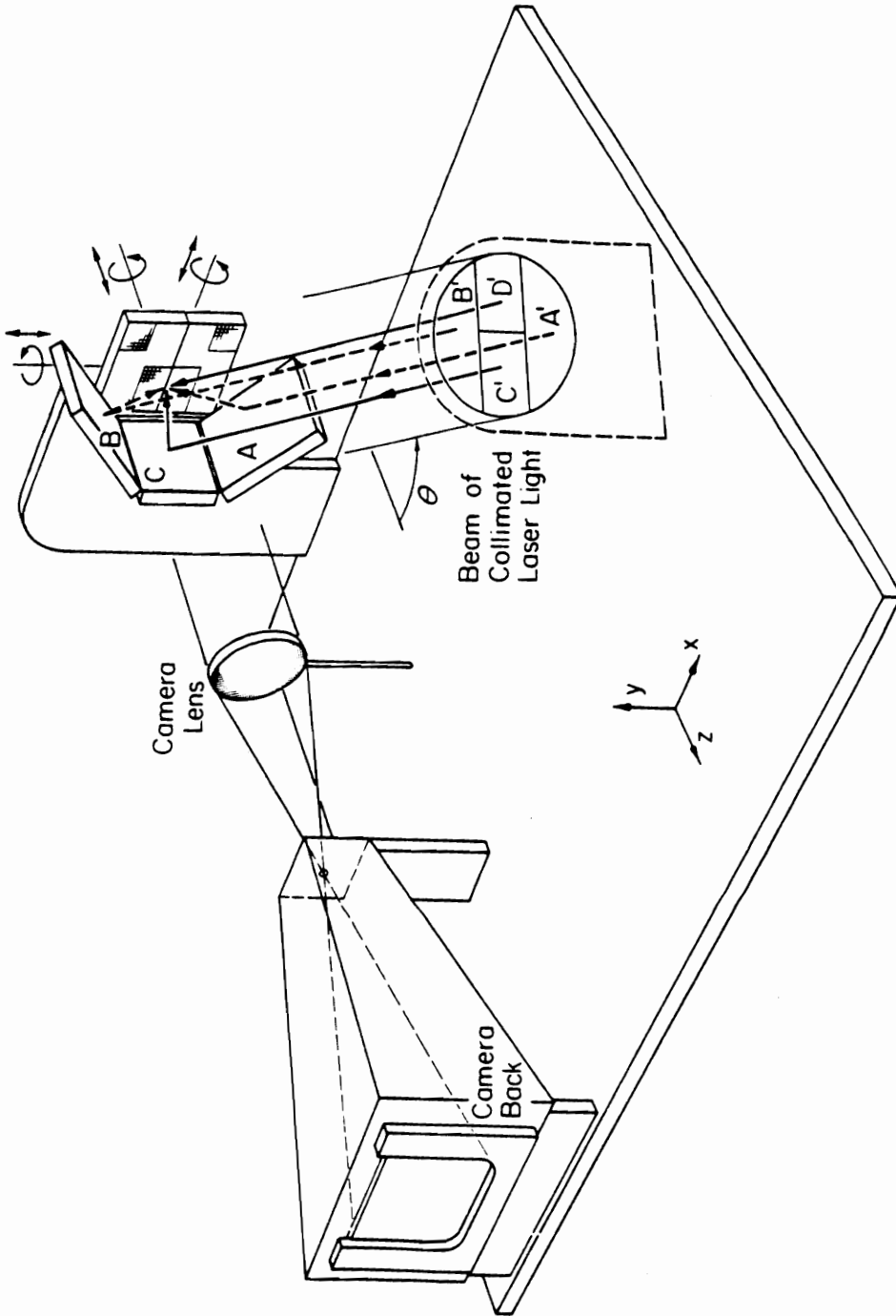


Figure 19. Four-beam moiré interferometer and specimen with deformed specimen grating

virtual reference grating for the  $U$  field was formed by sub-beams  $C'$  and  $D'$ , after reflection of beam  $C'$  by mirror  $C$ .

### 3.3.5 Virtual Reference Grating - Calibration

In the procedure employed here, a room-temperature replica of the *ULE grating mold* was installed on a fixture behind the interferometer (shown in Figure 19) where the specimen was later placed. A replica of the ULE grating mold (made at room temperature) will insure that the same conditions of the undeformed specimen grating (at elevated temperature) can be matched by the reference grating. This replica of the ULE grating mold was used to calibrate the virtual reference grating. Figure 20 illustrates why this is necessary.

The ULE grating mold, shown in Figure 20(a), is a crossed-line grating with grating frequencies  $F_1$  and  $F_2$  superimposed at an angle,  $\beta$ . Although  $F_1$  and  $F_2$  are essentially equal, they might not be exactly equal. And, although angle  $\beta$  is nominally 90 degrees, it might not be exactly 90 degrees. A replica, or mirror image of the ULE grating mold would produce the crossed-line grating shown in Figure 20(b) with frequencies  $F_1$  and  $F_2$  superimposed at an angle of,  $(180^\circ - \beta)$ . Mixing these two different orientations (i.e. adjusting or "tuning" the interferometer to the original ULE grating mold to interrogate a replica of the ULE grating mold ) would introduce an error of  $2 \times (90^\circ - \beta)$  in shear strain measurement.

Simply rotating the ULE grating mold by  $90^\circ$ , as shown in Figure 20(c), would eliminate this error. However, an error in extension measurement would be introduced if the grating frequencies,  $F_1$  and  $F_2$  are not exactly the same. To avoid these sources of error, a replica of the ULE grating mold (shown in Figure 20b), was used.

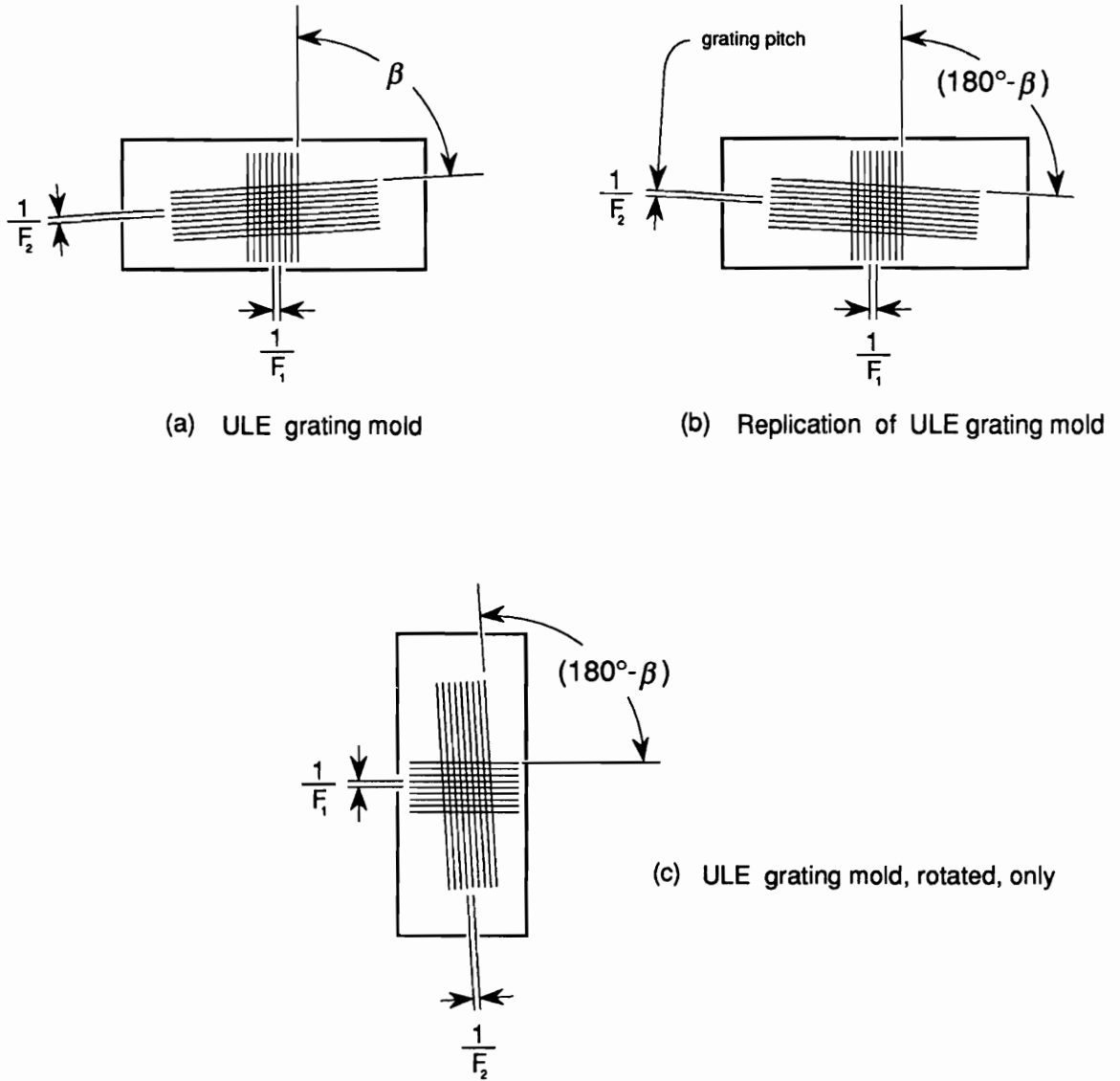


Figure 20. ULE mold: (a) original orientation , (b) replication, and (c) rotated, only.

This room temperature replica of the *ULE grating mold* was then placed in the interferometer and used to adjust (or "tune") the frequencies and orientation of the reference grating. The interferometer was adjusted to produce null fields (which are uniform intensity across each field) for both the  $U$  and  $V$  fields. The procedure outlined in Ref. [108] was followed for the adjustment, and it is referred to, briefly, in the following section. (Light diffracted in the  $0^{\text{th}}$  order of the grating is directed back into the source to define the angular orientation of the plane of the grating.) After null fields were established and calibration of the virtual reference gratings were completed, the mirrors remain fixed. They were never readjusted during the course of the experiment.

### 3.3.6 Moiré Carrier Patterns

A carrier pattern is introduced by changing the frequency and/or orientation of the reference grating. A carrier pattern is the result of the mismatch between the *adjusted* reference grating frequency, and the *true* or *absolute* reference grating frequency. The carrier pattern is an important ingredient in moiré interferometry. Together with other special properties, it makes moiré interferometry a unique and powerful technique for displacement and strain measurements. Carrier patterns can be used for various purposes, including (1) to increase the accuracy of extracting data from fringe patterns, (2) to distinguish the signs of the displacements by introducing a carrier pattern of known sign, (3) to determine fringe gradients when they are not adequately represented in the load-induced fringe patterns, (4) to cancel the initial or no-load fringe pattern, and (5) to measure in-plane and out-of-plane displacements, simultaneously [110]. Here, in this study, carrier patterns were used to cancel the uniform, thermal-contraction portion of the displacement fields, and to accentuate details in the deformation fields.

In moiré interferometry, the frequency and orientation of the reference grating is changed by adjusting the incident beam. These adjustments can be made by changing the angle of the incoming collimated beam (shown in Figure 19), or by changing the angle of *mirrors A and B*, (or *mirror C*).

For the work presented here, the reference grating was calibrated to a known value by changing the angle of the mirrors. And, to ensure that the reference grating remained constant throughout the experiment, the mirror angles were not changed after the initial calibration. Therefore, it was necessary to introduce carrier patterns by changing the angle of the incoming collimated beam. However, it was also necessary to introduce the carrier patterns in such a way that the *calibrated* optical system was not disturbed.

This was accomplished by inserting a glass plate in the diverging path of the laser light, prior to its collimation. Inclination of this glass plate changed the angle of the incoming collimated beam, without altering the calibration of the system. The carrier pattern was adjusted by changing the angle of the glass plate, and the carrier could be removed easily, by removing the glass plate from the system.

The pattern of Figure 21 on page 47 was transformed into that of Figure 22 on page 47 by carrier fringes of extension. The carrier fringes are parallel to the x axis, so  $\partial N_y/\partial x$  is not changed. However, the gradient  $\partial N_y/\partial y$ , corresponding to a normal strain in the y-direction, is altered by a constant, uniformly over the field. The special virtue of Figure 22 is that it makes the transition region between brass and steel very clear. This apparent subtraction of a uniform strain over the entire field helps to accentuate the non-uniform strain. The fringe gradients  $\partial N_y/\partial y$  (corresponding to normal strains  $\epsilon_y$ ) across the interface change dramatically in an extremely narrow zone, which is emphasized by this addition of carrier fringes. This zone is apparently less than 0.005-in. wide, in Specimen-A.



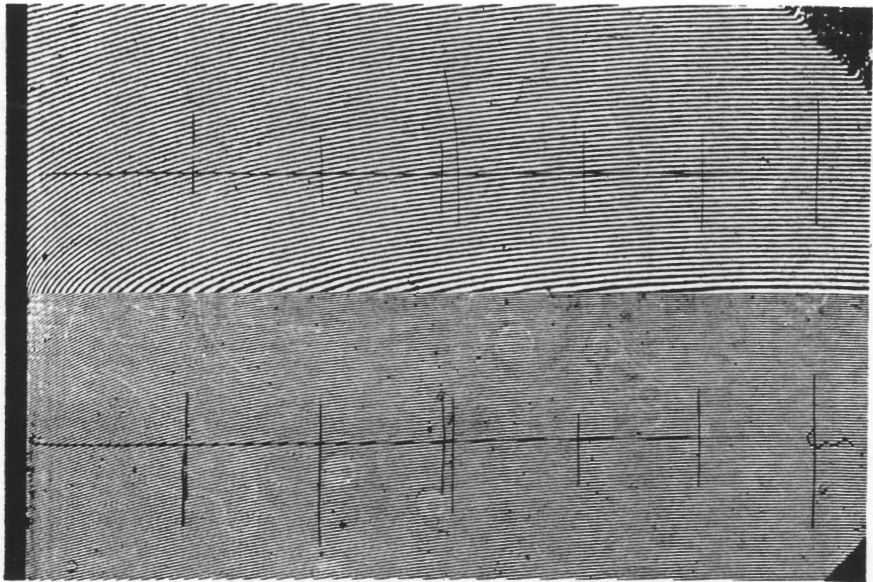


Figure 21. Specimen-A. V-displacement fields without a carrier pattern.

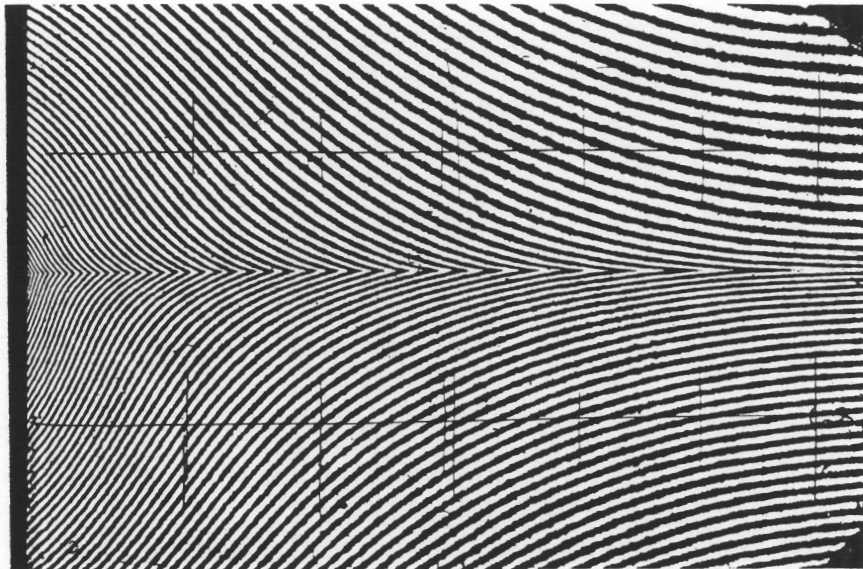
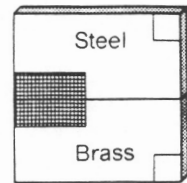
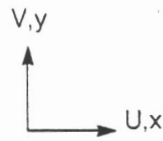


Figure 22. Specimen-A. V-displacement field with a carrier pattern.

## **3.4 Data Extraction from Experimental Results**

### **3.4.1 Recording Data**

Specimen gratings were replicated at an elevated temperature, and interrogated at room temperature. Therefore, the deformation observed was the result of the temperature difference,  $\Delta T$ . The specimen deformation caused by the temperature difference,  $\Delta T$ , was observed by the optical system described above, after the system was calibrated.

To record the thermal-deformation data, the specimen was attached to a fixture that allowed translations in the x, y, z directions, as well as universal angular adjustments about these axes. After the calibration steps described above (or "tuning" the system), the total U - and V - displacement fields were recorded photographically. And, in addition, carrier patterns were introduced to accentuate the stress-induced irregularities as well as the patterns of stress-induced fringes, which were also photographically recorded.

### **3.4.2 Specimen A - An Example of the Experimental Method**

The specimen was the bimetal plate shown in Figure 14 and Figure 16(a). Specimen gratings were replicated (at 314°F.) in the regions shown. The larger grating was used to investigate thermal deformations near the interface, and the corner gratings were used to determine the coefficients of thermal expansion of the steel and the brass.

The fixture to which the specimen was attached (shown in Figure 19) allowed controlled translations in the  $x$ ,  $y$ ,  $z$  directions, and universal angular adjustments about these axes. After the steps described above ("tuning" the system), the  $U$  and  $V$  fields were recorded photographically for the three regions. Figure 21 is the  $V$ -displacement field surrounding the joint. This is the total displacement caused by the  $-240^{\circ}F$  temperature change from the grating replication temperature to the interrogation (room) temperature. This thermal deformation is independent of any state of residual stresses developed in the manufacturing process of the material and the joining process of the specimen, since such residual stresses would have already been present when the specimen grating was applied; only the change of deformation is measured.

### 3.4.3 Data Reduction

#### 3.4.3.1 Calculation of Strains and Stresses

The governing equations for the thermal-strain problems are given in Table 6 on page 51, where,

$U$  and  $V$  are displacements in the  $x$  and  $y$  directions, respectively;

$N_x$  and  $N_y$  are the fringe orders in the  $U$  and  $V$  displacement patterns, respectively;

$N_x^t$  and  $N_y^t$  are fringe orders in the corresponding  $U$  and  $V$  fringe patterns of *total* displacements;

$N_x^\sigma$  and  $N_y^\sigma$  are fringe orders in the corresponding  $U$  and  $V$  fringe patterns of *stress-induced* displacements;

$f$  is the "effective" grating frequency, with

$$f_0 = 2400 \text{ lines/mm} \quad (60,960 \text{ lines/in.}), \quad \text{for the macroscopic study;}$$

$\varepsilon$  and  $\gamma$  are normal and shear strains, respectively;

$\sigma$  and  $\tau$  are normal and shear stresses, respectively;

$\Delta T$  is the temperature increment;

$\alpha$  is the coefficient of thermal expansion;

$\nu$  is Poisson's ration;

$E$  is the modulus of elasticity, or *Young's Modulus*;

$G$  is the shear modulus of elasticity, (or modulus of rigidity);

superscripts  $t$ ,  $\sigma$ , and  $\alpha$ , correspond to the total strain, the stress-induced part of the strain, and the free-thermal-expansion part of the strain, respectively;

$\alpha$ ,  $\nu$ ,  $E$ , and  $G$  are a different value for steel and for brass, and are listed in Table 5 on page 33, as well as in Figure 16 and Figure 17 on page 34.

Here,  $U$ ,  $V$ ,  $N_x$ , and  $N_y$  represent total displacements and fringe orders, as read from total deformation patterns such as Figure 21 on page 47. Equations (3)-(5) and (9)-(11) apply to

**Table 6. Governing equations for the thermal-strain problem.**

Displacements:

$$U = \frac{1}{f} N_x, \quad V = \frac{1}{f} N_y \quad (1)$$

Normal Strains:

$$\varepsilon_x = \frac{\partial U}{\partial x} = \frac{1}{f} \left( \frac{\partial N_x}{\partial x} \right), \quad \varepsilon_y = \frac{\partial V}{\partial y} = \frac{1}{f} \left( \frac{\partial N_y}{\partial y} \right) \quad (2)$$

$$\varepsilon^t = \varepsilon^e + \varepsilon^\alpha, \quad \varepsilon^\alpha = \alpha \Delta T \quad (3)$$

$$\varepsilon_x^e = \varepsilon_x^t - \varepsilon^\alpha = \frac{1}{f} \left( \frac{\partial N_x^e}{\partial x} \right) - \varepsilon^\alpha = \frac{1}{f} \left( \frac{\partial N_x^e}{\partial x} \right) \quad (4)$$

$$\varepsilon_y^e = \varepsilon_y^t - \varepsilon^\alpha = \frac{1}{f} \left( \frac{\partial N_y^e}{\partial y} \right) - \varepsilon^\alpha = \frac{1}{f} \left( \frac{\partial N_y^e}{\partial y} \right) \quad (5)$$

Shear Strains:

$$\gamma_{xy}^e = \frac{\partial U}{\partial y} + \frac{\partial V}{\partial x} = \frac{1}{f} \left( \frac{\partial N_x}{\partial y} + \frac{\partial N_y}{\partial x} \right) \quad (6)$$

$$\gamma_{xy}^t = \gamma_{xy}^e, \quad \text{as } \gamma_{xy}^\alpha = 0 \quad (7)$$

$$\gamma_{xy}^e = \frac{1}{f} \left( \frac{\partial N_x^e}{\partial y} + \frac{\partial N_y^e}{\partial x} \right) = \frac{1}{f} \left( \frac{\partial N_x^e}{\partial y} + \frac{\partial N_y^e}{\partial x} \right) \quad (8)$$

Stresses:

$$\sigma_x = \frac{E}{1 - \nu^2} (\varepsilon_x^e + \nu \varepsilon_y^e) \quad (9)$$

$$\sigma_y = \frac{E}{1 - \nu^2} (\varepsilon_y^e + \nu \varepsilon_x^e) \quad (10)$$

$$\tau_{xy} = G \gamma_{xy}^e = \left[ \frac{E}{2(1 + \nu)} \right] \gamma_{xy}^e \quad (11)$$

the brass and steel portions, separately, inasmuch as  $\alpha$  (and  $\varepsilon^\alpha$ ),  $\nu$ ,  $E$ , and  $G$  are different in the two materials. Equations (9) and (10) apply to the surface of the specimen, where there are no normal tractions on the surface. Shear strains and corresponding shear stresses are

independent of the uniform thermal contraction (equation 7). Therefore, either  $N^t$  or  $N^\sigma$  can be used to determine the shear strain (equation 8).

### **3.4.3.2 Specimen-A: An Example of the Experimental method, using carrier patterns**

The pattern of Figure 21 on page 47 was transformed into that of Figure 22 on page 47 by carrier fringes of extension. The carrier fringes are parallel to the x axis, so  $\partial N_y/\partial x$  is not changed. However, the gradient,  $\partial N_y/\partial y$ , corresponding to a normal strain in the y-direction, is altered by a constant, uniformly, over the entire field and helps to accentuate the non-uniform strain. The carrier fringes used (added) to transform the pattern of Figure 21 into the pattern of Figure 22 on page 47, were carrier fringes of extension, which were approximately equal to the average thermal expansion of the brass and steel, in magnitude, but opposite in sign. The differences between Figure 21 and Figure 22, are an excellent example of the special virtue of the carrier pattern, which, in this case, makes the transition region between brass and steel very clear. The fringe gradients,  $\partial N_y/\partial y$  (corresponding to normal strains  $\epsilon_y$ ) change dramatically, across the interface, in an extremely narrow zone, which is emphasized by this addition of carrier fringes. This extremely narrow zone is apparently less than 0.005-in. wide.

The carrier pattern of extension corresponds to adding or subtracting a constant strain over the entire fringe pattern, as illustrated above. Therefore, this technique can also be used to subtract the constant stress-free thermal contraction from the entire field. After subtraction, the pattern represents the stress-induced part of the total deformation.

The stress-free corners, away from the interface, were used to determine the stress-free thermal contraction, as well as the carrier pattern required to subtract the (constant) thermal contraction from the total deformation. An example of this is shown in Figure 23, below, for the stress-free corner of the brass, before (Figure 23a) and after (Figure 23b) the addition of the carrier pattern equal (in magnitude) to the stress-free thermal contraction of the brass, but with opposite sign. In Figure 23(a), the fringe gradient represents the free thermal expansion of the brass; the adjustment that produces (b) introduces an opposite fringe gradient that nullifies the fringes of free thermal expansion at the corner and everywhere else in the specimen.

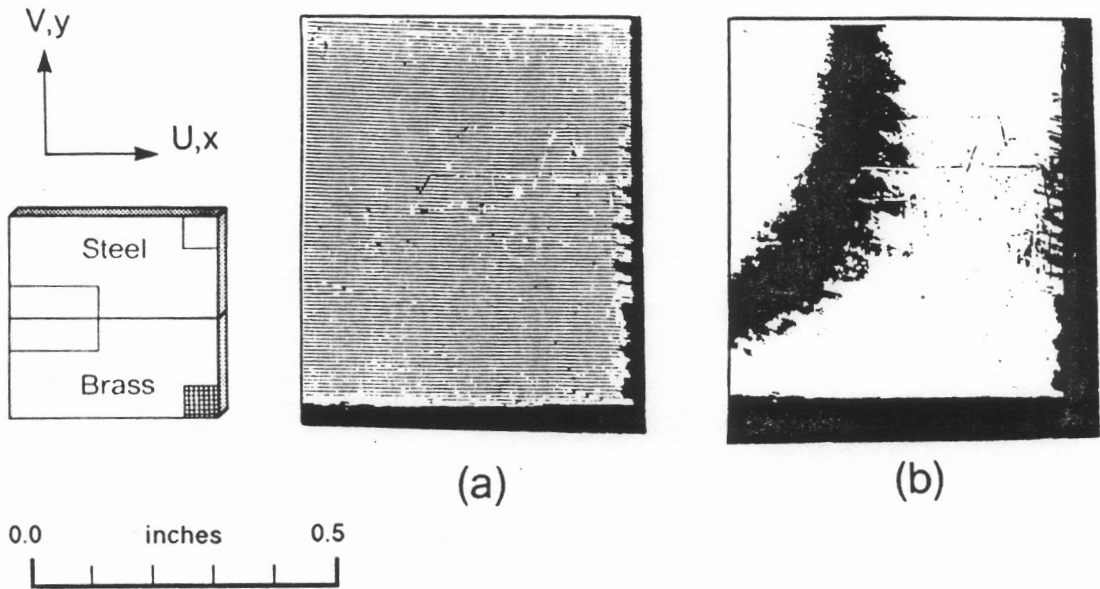


**Figure 23.** The V-displacement field in the stress-free brass corner, (a) without, and (b) with carrier pattern.

The constants  $\alpha$  and  $\varepsilon^\alpha$ , were determined from this experiment, separately, for the brass and steel by equation (3). These values were determined from each of the free corner (stress-free) patterns for the brass and the steel.

## **Chapter 4**

### **Chapter 4: Experimental Results**



## 4.1 Results: Specimen - A

The temperature increments and thermal-expansion measurements are given below, in Table 7.

Table 7. Temperature increments, thermal strains, and coefficients of thermal expansion.

Specimen	$\Delta T$	$\alpha \Delta T = \epsilon^\alpha$ , Strain $\times 10^6$		
		Steel	Brass	$\Delta \epsilon^\alpha$
A	-133°C (-240°F)	-1663	-2601	938
B	-144°C (-260°F)	-1823	-2750	927
C	-136°C (-245°F)	-1688	-2602	914
D	-126°C (-227°F)	-1568*	-2435*	867*

### 4.1.1 The Use of Moiré Interferometry

The direct results of moiré interferometry for Specimen-A are shown in Figure 24 and Figure 25. Figure 24(a), is the total V-displacement field, i.e., the  $N_y^\dagger$  pattern. It is dominated by the thermal contraction of each part, steel and brass; thus the gradient  $\partial N_y^\dagger / \partial y$  is negative everywhere. This is seen in the magnified pattern of Figure 26, which verifies that

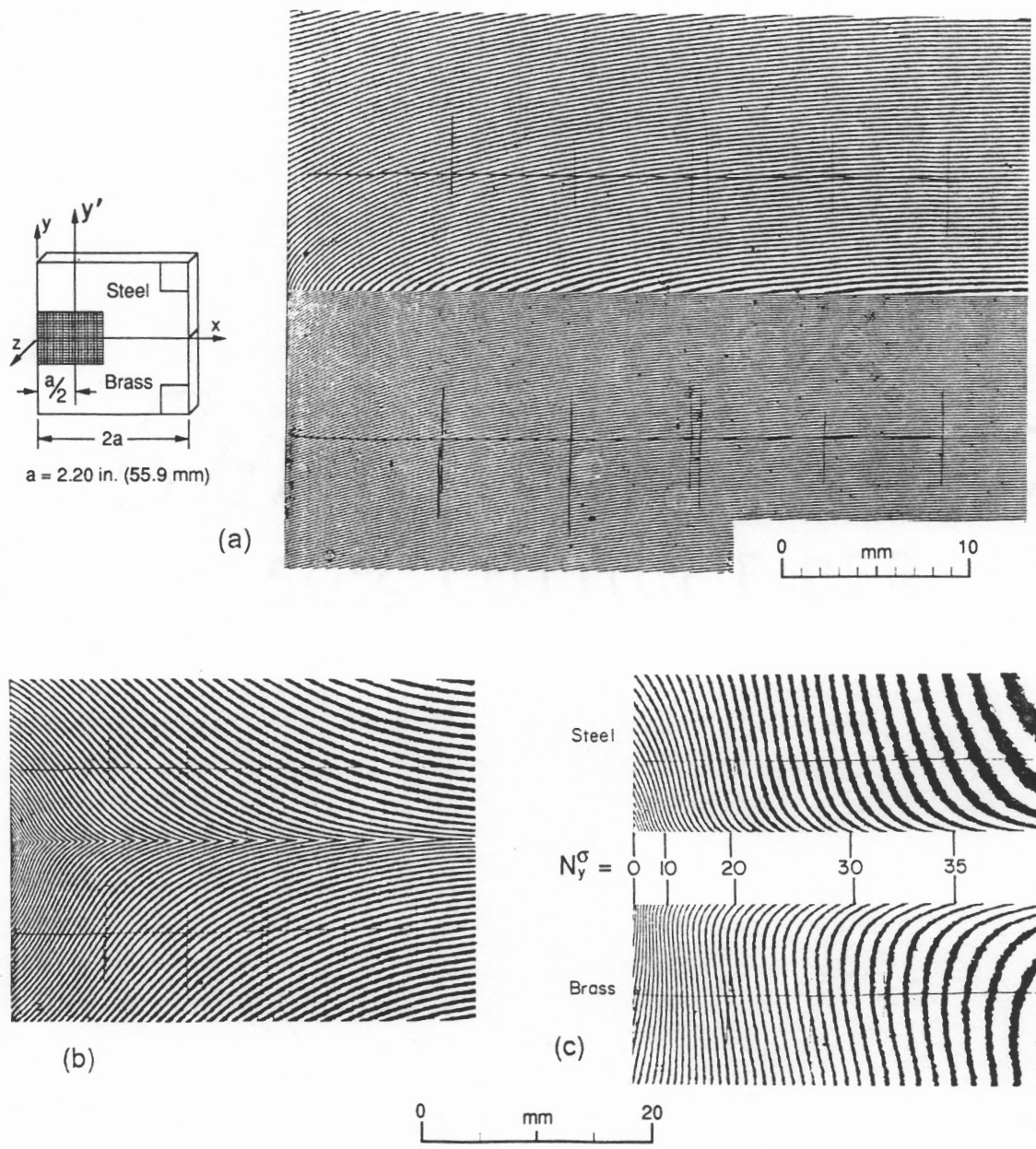


Figure 24. Specimen-A. V-displacement fields in the shaded region for  $\Delta T = -240^\circ\text{F}$  ( $-133^\circ\text{C}$ ). (a) contours of  $N_y^σ$ , depicting the total displacements. (b) V field, modified by carrier fringes of extension, (approximately) equal to the average of the thermal contractions. (c) contours of  $N_y^σ$ , depicting the stress-induced displacements in steel and brass.

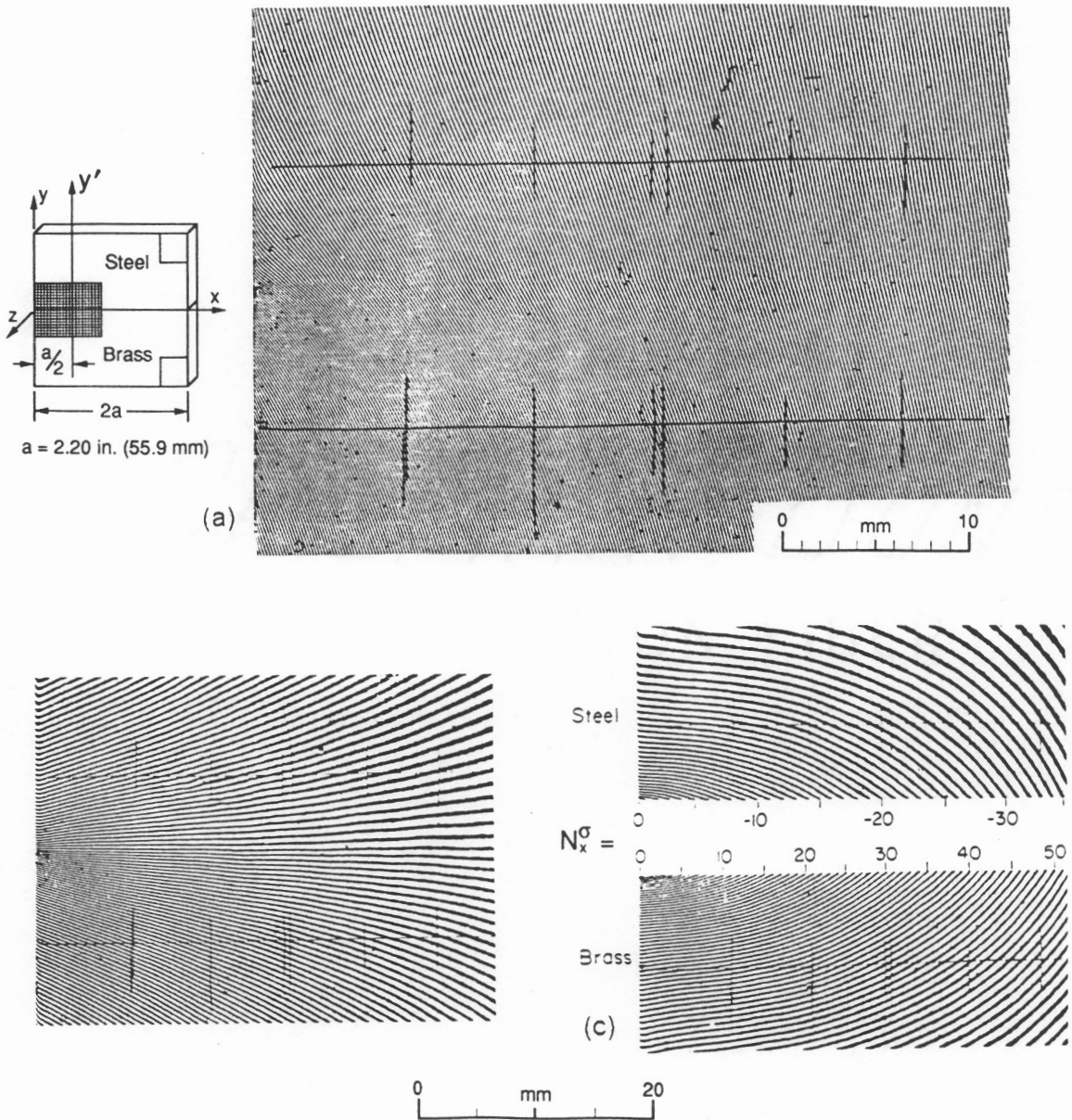


Figure 25. Specimen-A. U-displacement fields in the shaded region for  $\Delta T = -240^\circ\text{F}$  ( $-133^\circ\text{C}$ ). (a) contours of  $N_x^I$ , depicting the total displacements. (b) U field, modified by carrier fringes of extension, (approximately) equal to the average of the thermal contractions. (c) contours of  $N_x^\sigma$ , depicting the stress-induced displacements in steel and brass.

$N_x^y$  decreases everywhere, as  $y$  increases. The zero-order fringe is chosen arbitrarily, because the analysis of deformations only requires relative displacements.

Although the fringe gradients in both materials change quite rapidly near the interface, the total displacements across the steel/brass interface must be continuous (unless the material has failed, leaving a gap). The stress-induced deformations combine with the free thermal contractions to produce a very-sharp change of fringe gradient across the interface. This change is emphasized in Figure 24(b) (and earlier, in Figure 22 on page 47), where carrier fringes of extension were introduced. These carrier fringes have the effect of subtracting off a uniform strain (approximately) equal to the average of the thermal contractions. The change across the interface is rather abrupt, which is emphasized by the carrier patterns used in these figures.

In Figure 24(c), the carrier fringes introduced a uniform, apparent strain, equal and opposite to the experimentally determined  $\epsilon^\alpha$  (or  $\alpha \Delta T$ ), which had the effect of canceling the free thermal contraction part of the fringe pattern. The result is a pattern of the stress-induced displacements, namely the contour map of  $N_x^y$ . This procedure was carried out for the upper (steel) and lower (brass) regions, separately, since the magnitudes of  $\alpha$ , (or  $\epsilon^\alpha$ ) are different for steel and brass.

The U-displacement fields (corresponding to the V-displacement fields in Figure 24), are shown in Figure 25. Figure 25(a) is the total displacement pattern of the  $N_x^y$  fringes. Figure 25(b) is the same field, but combined with a carrier pattern that has the effect of subtracting a constant strain from the entire field. The value of carrier strain subtracted off, is (approximately) equal to the average of the thermal contractions of the brass and steel (and corresponds to the carrier for the V-displacement field shown in Figure 24b). Figure 25(c) is the stress-induced part of the U field, depicted by contours of  $N_x^y$ . Pattern (b) demonstrates

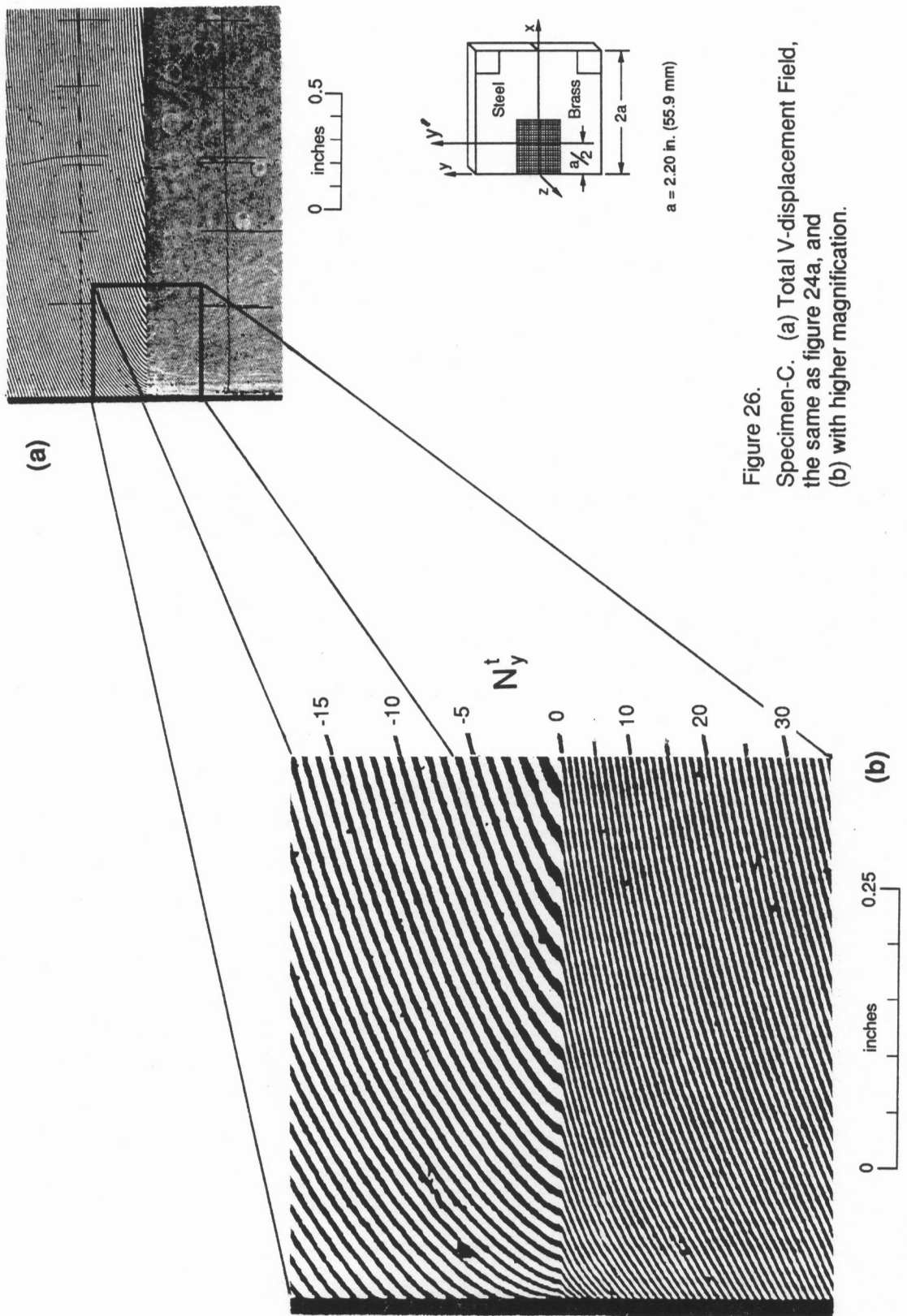


Figure 26.  
 Specimen-C. (a) Total V-displacement Field,  
 the same as figure 24a, and  
 (b) with higher magnification.

that the  $\epsilon_x^t$  (total) strains in the steel and brass are essentially constant along the interface and identical in the two materials. The fringe orders marked in Figure 25(c), indicate that the stress-induced strain,  $\epsilon_x^t$ , along the interface is compressive in the steel and tensile in the brass. This is consistent with the greater thermal contraction of the brass and the opposing restraint by the steel.

#### 4.1.2 The Use of Mechanical Differentiation

Figure 27 introduces another kind of fringe pattern, the pattern of mechanical differentiation [112] and [108]. Using Figure 27(a) as an example, the pattern was constructed by superimposing two photographic images of Figure 25(a), with a shift of one image relative to the other by a finite increment,  $\Delta x$ . (Here,  $\Delta x = 0.1$  in., or 2.5 mm). When shifted, the dark lines of the two patterns interweave and create a moiré effect. The effect is known as geometric moiré, which is distinct from the interferometric moiré of Figure 24 and Figure 25. At any point in the pattern (resulting from mechanical differentiation) the fringe order  $N_{xx}^*$  equals the difference,  $\Delta N_x^t$ , of fringe orders,  $N_x^t$ , in the two superimposed transparencies. Thus,

$$N_{xx}^* = \Delta N_x^t = \Delta x \frac{\Delta N_x^t}{\Delta x} \simeq \Delta x \frac{\partial N_x^t}{\partial x} \quad (12)$$

The double subscript refers, first, to the displacement component of the fringe pattern and, second, to the direction of the shift. Using  $N_{ij}$ , the subscript "i" represents the displacement field (i.e. x for the U-displacement field and y for the V-displacement field), and the subscript "j" represents the direction of mechanical differentiation (i.e. a translation parallel to the x or y axis).

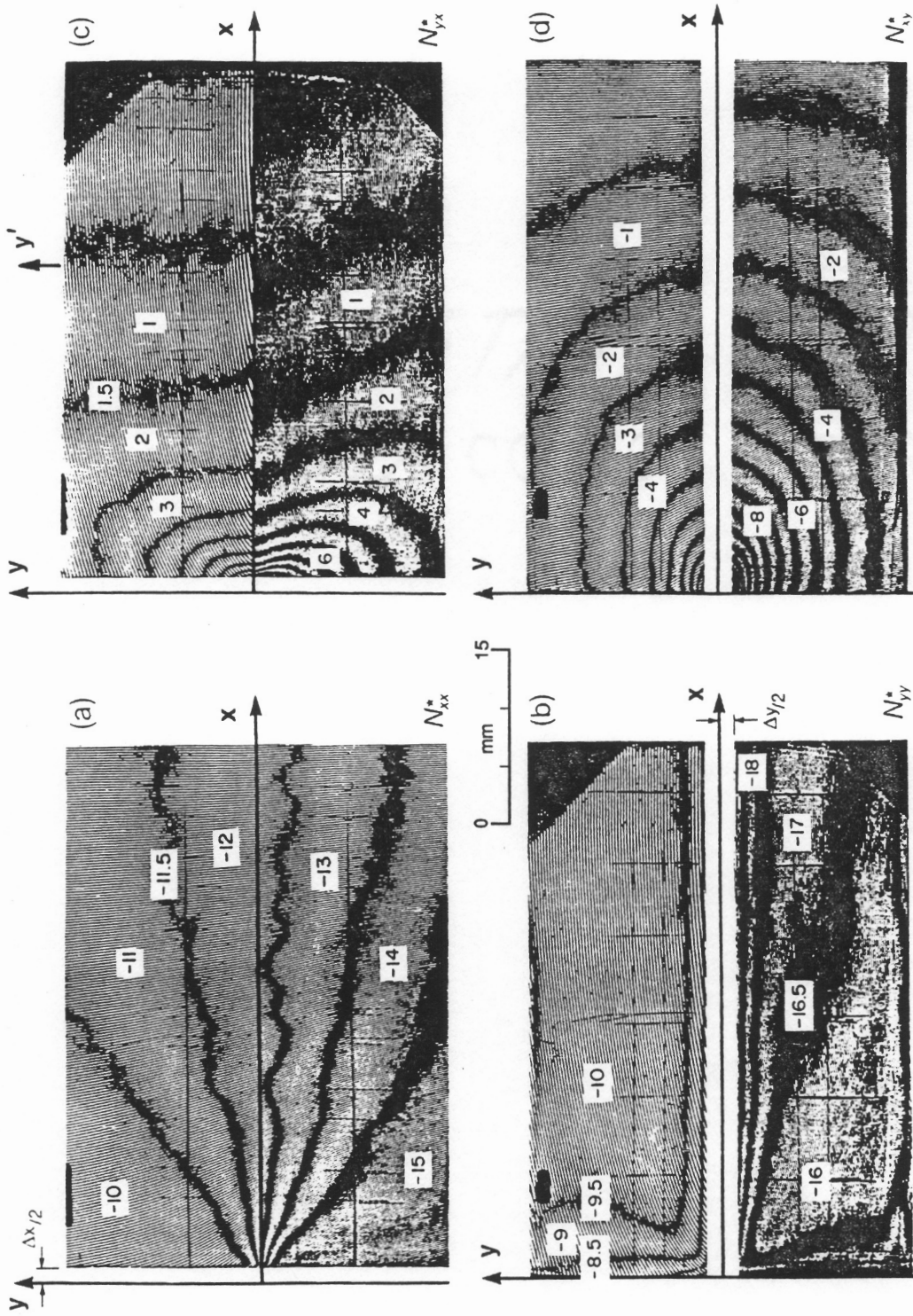


Figure 27. Specimen-A. Countours of displacement derivatives by mechanical differentiation.  
 $\Delta x = \Delta y = 0.1$  in. (2.5 mm).

Accordingly,  $N_{xx}^*$  is proportional to the finite-increment approximation of the differential. By Equation (4),

$$\varepsilon_x^\sigma \simeq \frac{1}{f \Delta x} N_{xx}^* - \varepsilon^\sigma \quad (13)$$

The finite increment approximation must exactly equal the derivative at least at one point in the interval and it is very accurate in regions where the strain gradient in the interval,  $\Delta x$ , is either linear or small. In this case, it is a useful means of extracting the derivatives on a whole-field basis everywhere except in the immediate vicinity of the interface.

The same procedure was used to portray all four derivative fields, i.e. shifting each pattern  $N_x^t$  and  $N_y^t$  by increments  $\Delta x$  and  $\Delta y$ . The increments were 2.5 mm (0.1 in.) in all cases, and the data pertains to the midpoint of each increment. Therefore, zones of width  $\Delta x/2$  and  $\Delta y/2$  are blank in the figures because the parent patterns did not overlap in these zones and no data exist, there. These blank zones are only 1.25 mm wide (or about 1% of the specimen length) and, in this case, the gradients were large in these zones, near the interface.

An obvious feature of the strain distribution is the irregular nature of fringes in Figure 27(a). A theoretical-elasticity solution would prescribe smooth contours, so the irregularities must be associated with some facet of the experiment. There does not appear to be a consistent argument that attributes the fringe irregularities to features of the experimental technique. It is tempting to attribute these fringe irregularities to gaps or cracks in the silver-solder joint. However, cracks would introduce out-of-phase fluctuations on opposite sides of the interface, in Figure 27(a). The observed in-phase fluctuations indicate that there is  $\varepsilon_x$ -continuity across the interface. Therefore, I believe that there were no gaps or cracks in the joint, but instead, one or both of the materials exhibits small variations of (one or more) physical properties, namely the thermal coefficient of expansion, modulus of elasticity and Poisson's ratio. These



variations might be heightened in a heat-affected zone near the silver-soldered interface, where the fringe irregularities are most severe. This is also the zone of largest residual stresses. Such anomalies illustrate the idiosyncracies of real materials.

In Figure 27, the largest departure from a smooth  $N_{xx}^*$  fringe occurs near the interface in the brass, where the departure is about 1/4 of a fringe order. If a variation of the thermal coefficient of expansion in the brass was fully responsible for this irregularity, the local value of  $\alpha$  would have changed by  $3 \times 10^{-7}/^\circ\text{C}$ , (or by 1.5% of its global value).

Away from the interface, the  $N_{xx}^*$  fringes were smoothed for data interpretation. Then, (using the mechanical-differentiation pattern of Figure 27, with  $\Delta x = 0.10$  in.), the total strains were determined from the fringe orders by

$$\varepsilon_x^t = \frac{N_{xx}^*}{f \Delta x} = 164 \times 10^{-6} N_{xx}^*, \quad (2')$$

and the stress-induced strains by

$$\varepsilon_x^\sigma = 164 \times 10^{-6} N_{xx}^* - \varepsilon_x^\alpha. \quad (4')$$

Note that  $\varepsilon_x^\alpha$  is negative for both materials (as a negative temperature increment was used). Similar relationships apply for all four derivatives. The numbers shown on the fringe patterns are  $N^*$  values for each derivative field, where,  $N^*$  represents  $N_{ij}$ , as described, above.

### 4.1.3 Graphs and Contour Maps

The displacement patterns of Figure 24 and Figure 25 were analyzed in accordance with Equations (4), (5), and (8), given in Table 6 on page 51. A detailed analysis was performed along the  $y'$  axis at the quarter-width of the specimen. The results for the stress-induced strains are plotted in Figure 28. Corresponding strains along  $y'$  are substantially different in sign and magnitude for the steel and brass. Near the interface, where  $y' \simeq 0$ , the difference of stress-induced strains,  $\varepsilon_x^s$ , in steel and brass is almost equal to the difference of free thermal contractions,  $\varepsilon^a_{(steel)} - \varepsilon^a_{(brass)}$ , or  $\Delta \varepsilon^a$ . The  $\varepsilon_x^s$  and  $\gamma_{xy}$  curves are nearly linear and data extraction was relatively easy. The  $\varepsilon_y^s$  curves and their values far away from the interface are nearly linear, also. However, special attention was given to the determination of the  $\varepsilon_y^s$  curves and their values near the interface.

The gradient of the  $N_y$  vs.  $y$  curve rapidly increases (or decreases in magnitude) approaching the interface, and linear interpolation of fringe order between fringes in this interface region is no longer valid. Consequently, additional data was sought to increase the number of data points in this region, which increased the sensitivity of the experiment in this region, allowing the  $N_y$  vs.  $y'$  curve to be defined more accurately.

This additional data was extracted from the fringe patterns, using a method somewhat analogous to the method of *fringe-shifting* [116,117]. The method is referred to here, as *the parallel-axis method*, and is described below in section 4.2: *Technique developed for increasing sensitivity of the experimental method*.

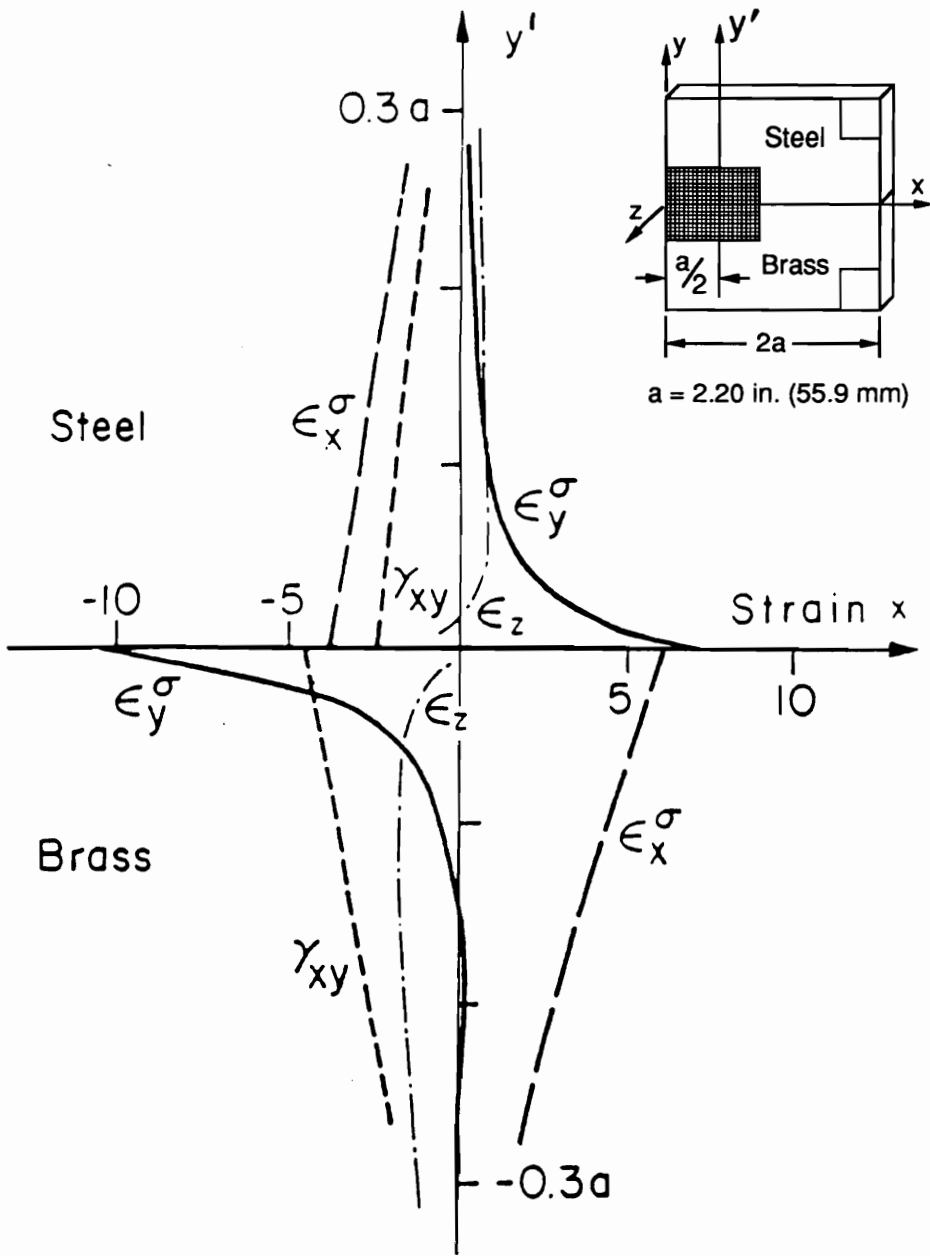


Figure 28. Specimen-A. The distribution of stress-induced strains on the  $y'$  axis along the free surface.  $\epsilon_z$  was calculated from  $\epsilon_x$  and  $\epsilon_y$  by the relationship,  $\epsilon_z = -\nu(\epsilon_x + \epsilon_y)/(1-\nu)$ .

These data were extracted from Figure 24(a), as well as other fringe patterns of the V-displacement field with the addition of carrier fringes, by *the parallel-axis method*, described in section 4.2.

The  $\varepsilon_y$  strains were not extrapolated to the interface, but remained undetermined from this experiment, in the narrow zone bounded by  $y \simeq \pm 100 \mu m$ . (0.004 in.), called the *interface zone*.

The corresponding stresses were calculated from the strains by Equations (9)-(11) (given in Table 6 on page 51), which are valid over the free surface of the specimen, where  $\sigma_z = 0$ . These stresses, along the  $y'$  axis of Specimen-A, are plotted in Figure 29. The stress distributions are remarkably similar in the steel and brass. The shear stresses are nearly symmetrical and exhibit equal magnitudes at the interface (as theoretically required for equilibrium). Normal stresses,  $\sigma_x$ , have similar distributions, but opposite signs. The difference between interface values does not violate equilibrium, because  $\sigma_x$  is self-equilibrated. Normal stresses,  $\sigma_y$ , exhibit similar distributions, but also with opposite signs. Similar to the  $\varepsilon_y$  strains, the stresses near the interface were not extrapolated through the interface zone; if they were, a violation of  $\sigma_y$  equilibrium would appear. The  $\sigma_y$  stresses in the interface zone for this specimen (Specimen-A) will be validated and discussed, further, in the next chapter.

A detailed analysis of the fringe patterns, Figure 24 and Figure 25, was also performed along the interface zone. The stresses plotted in Figure 30 represent  $\sigma_x$  and  $\tau_{xy}$  at the interface, and the peak values of  $\sigma_y$ , which occur near the interface, although not on the interface. They illustrate that the stress disturbance at the specimen corner is highly localized, --- within about 1% of the specimen length for the normal stresses and 3% for the shear stresses. Elsewhere, (outside the *critical-corner* region), the normal stresses are constant and the shear

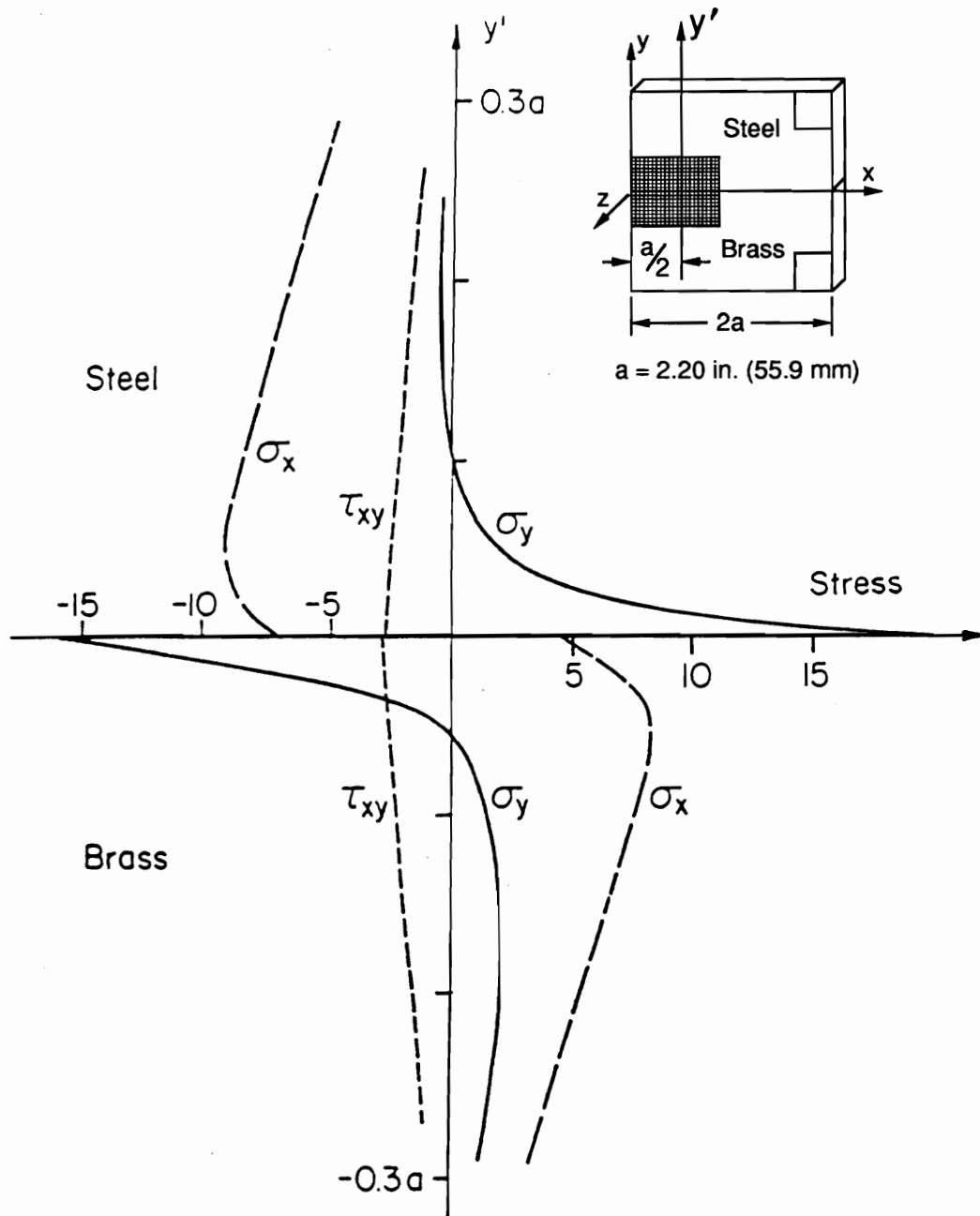


Figure 29. Specimen-A. The distribution of stresses on the  $y'$  axis. The units on the stress scale are psi, when the numbers are multiplied by 1000, and MPa, when multiplied by 6.9.

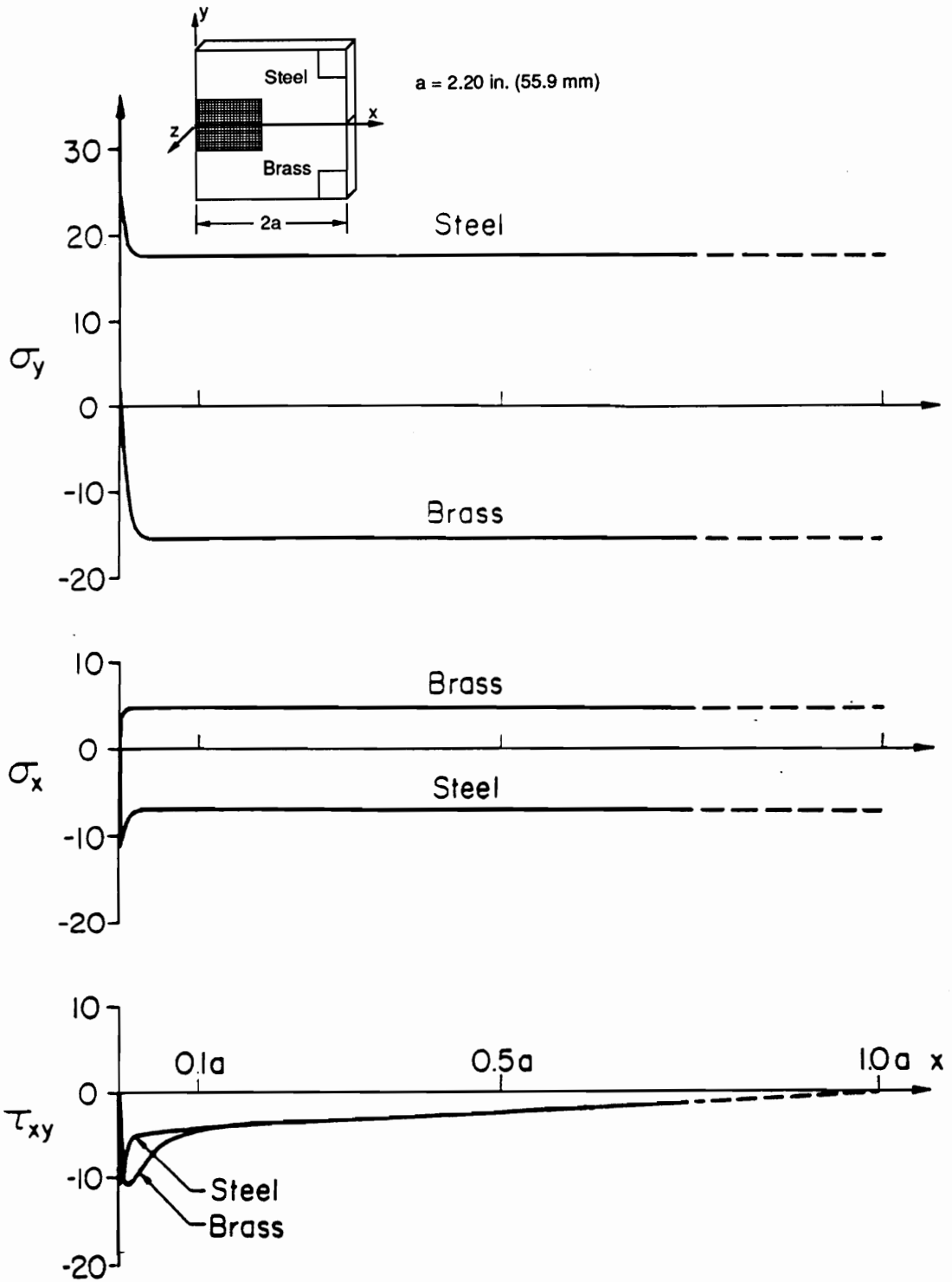


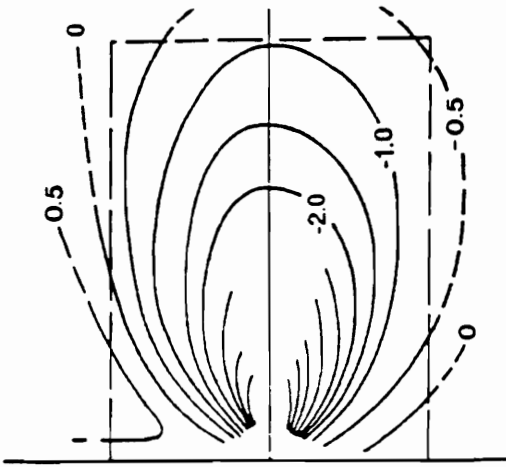
Figure 30. Specimen-A. The distribution of peak stresses near the interface, along the free surface. The units on the stress scale are psi, when the numbers are multiplied by 1000, and MPa, when multiplied by 6.9.

stresses vary linearly along the interface length. Of course, these represent stresses at the surface of the specimen and they are not proposed as representative of the interior stresses. (See Figure 6 on page 16, for the three-dimensional qualitative stress distribution, where it is clear that the distribution of *surface stresses* in a three-dimensional problem, does not represent the distribution of interior stresses.)

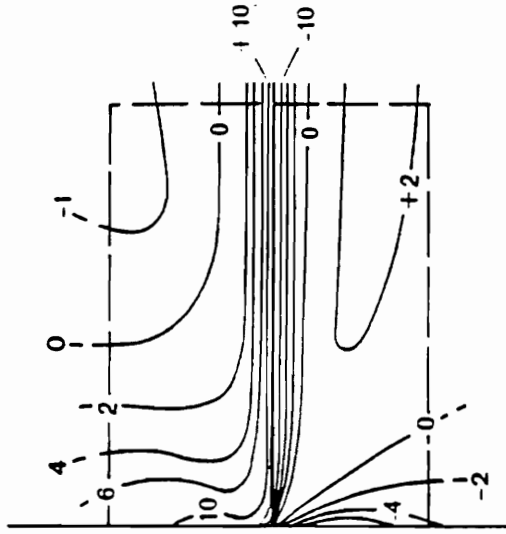
Whole-field contour maps of the surface stress fields for Specimen-A are shown in Figure 31. The mechanical differentiation data of Figure 27 were used for the portion of the specimen that was covered by the specimen grating (except in the high-gradient interface region). For the shear stress determination, the special graphical process of Post, et. al. [113] was used to add the cross-derivatives of Figure 27(c) and (d) and construct the map of shear strains, shown in Figure 31(c). Equations (9)-(11) were used to calculate the stresses. In the high-gradient region, near the interface, stresses were calculated using data from the moiré patterns of Figure 24 and Figure 25. Figure 31(b) illustrates that  $\sigma_y$  is very small except near the interface. The  $\sigma_y$  distribution is essentially independent of  $x$  near the interface, except close to the free corner (or *critical corner*) of the specimen, as illustrated by Figure 27(b).

## ***4.2 Technique developed for increasing sensitivity of the experimental method.***

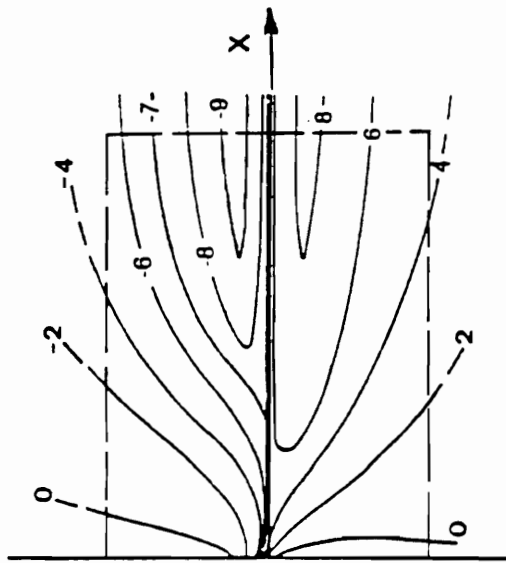
This technique is referred to here, as *the parallel-axis method*. This technique is performed by



(a)  $\sigma_x$



(b)  $\sigma_y$



(c)  $\tau_{xy}$

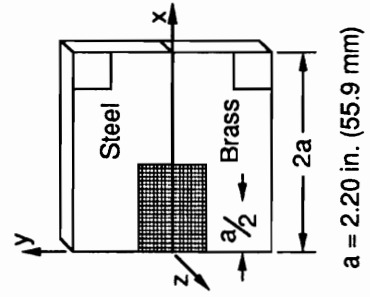


Figure 31. Specimen-A. Contour maps of the surface-stress distributions in the 1.2 x 1.6 in. (30 x 40 mm) portion of the specimen. The numbers denote stresses in psi, when the numbers are multiplied by 1000, and MPa, when multiplied by 6.9.



- (1) measuring the coordinates of the centers of fringes from an enlarged pattern, using a digitizing tablet, and then
- (2) plotting fringe order,  $N_y^f$ , vs. distance from the interface, along the  $y'$  axis, (i.e.  $N_y^f$  vs.  $y$ , along each  $y'$  axis),
- (3) drawing a *best fit* curve through this data and determining the slope of the  $N_y^f$  vs.  $y$  curve at various points along the  $y'$  axis.
- (4) calculating the strain, from the slope of the  $N_y^f$  curve using equation (2) from (Table 6 on page 51), and subtracting off any uniform carrier pattern as well as the uniform thermal expansion,  $\epsilon^\alpha$ , by equation (5), and plotting the curve through this high gradient portion of the data, and
- (5) repeating the above procedure along several  $y'$  axes parallel to  $y'$  and lying in the vicinity of  $y'$ .

The parallel-axis method is effective here, and in all other cases where  $\epsilon_y$  is independent of  $x$  in the region of interest, that is, where the  $N_y$ -fringes change with  $x$  in a self-similar fashion.

The value of this technique is its ability to extract an abundance of statistically significant data in the local region near the interface. It was used to reveal turn-around points near the interface for  $\epsilon_y$  curves that, otherwise, appeared to vary monotonically.

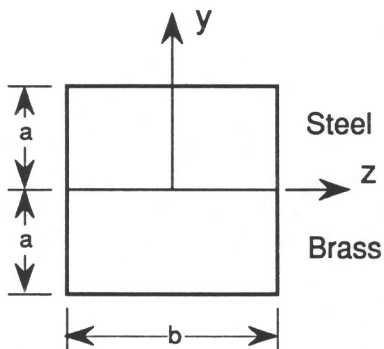
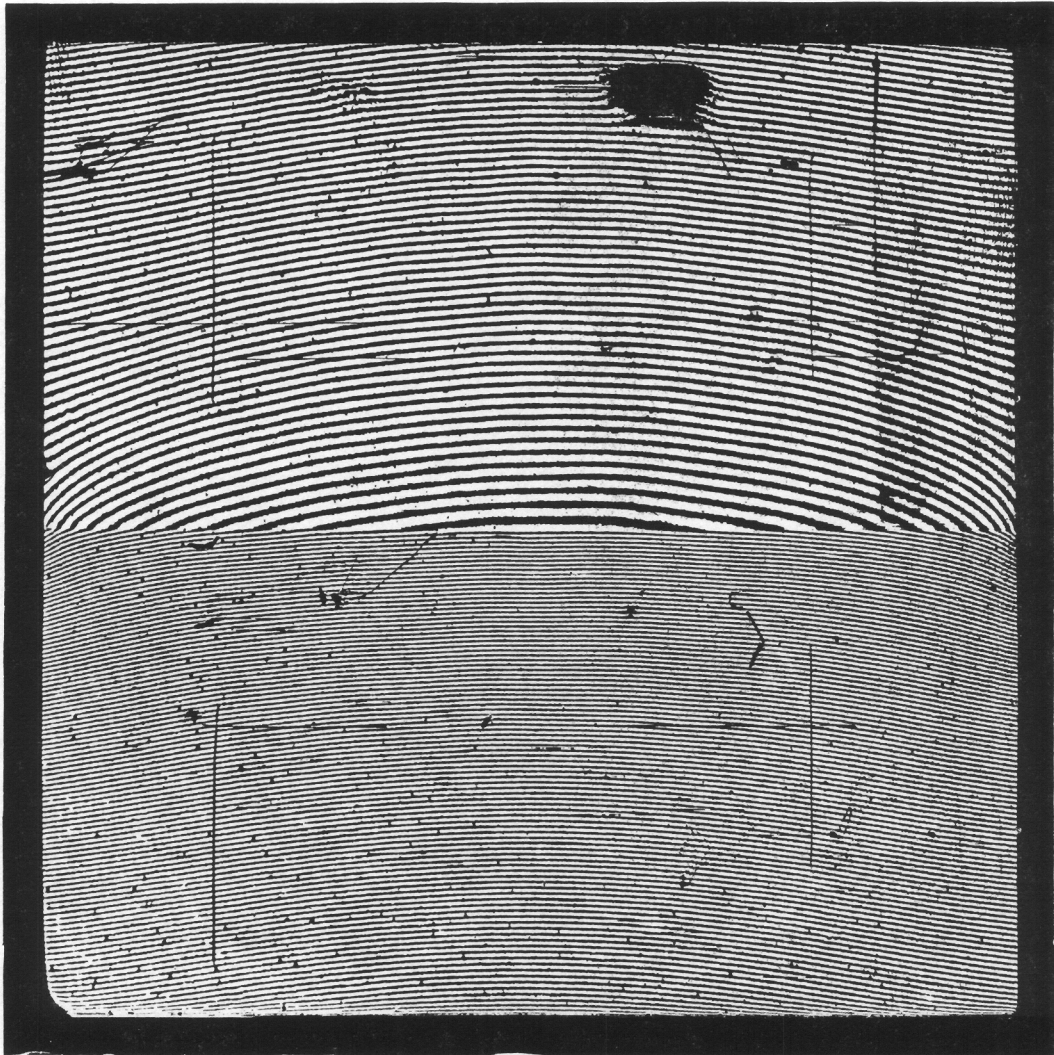
### 4.3 The turn-around-point

The *turn-around-point* (i.e. the point where the strains and corresponding stresses reach a maximum or minimum, and then reverse) was found to depend upon the geometric-aspect ratio of the specimen. Three specimen geometries were evaluated, specimen geometries A, B, and C, shown in Figure 16 on page 32. The turn-around-point was most evident in Specimen B, on the brass side, approaching the interface.

In Figure 32, it is clear that the fringes become closer and closer (i.e. the gradient,  $\partial V/\partial y$ , increases in magnitude) as they approach the interface from the brass side. However, the last fringe spacing on the brass side of the interface is wider, which indicates a turn-around-point. This is seen more clearly in Figure 33. Using *the parallel-axis method*, the turn-around-point was determined to be at about 0.039 inches from the interface, on the brass side of the interface, and about 0.008 inches from the interface, on the steel side of the interface. This is illustrated in Figure 34, which shows the stress,  $\sigma_y$ , along the specimen centerline, calculated from the V-field patterns and the corresponding U-field patterns.

Unlike Figure 32 and Figure 33, the turn-around-point was more difficult to determine in Specimen C, using Figure 35 and Figure 36. However, with the parallel-axis method, the turn-around-point was determined to be at about 0.017 inches from the interface on the brass side, and 0.002 inches of the interface on the steel side. This is illustrated in Figure 37, which shows  $\sigma_y$  along the specimen centerline.

The turn-around-points for Specimen A were closer to the interface than could not be determined from this method. An additional method was used to measure these values, *microscopic moiré interferometry*, and it is discussed in the following chapter.



$a = 0.50 \text{ in.}$   
 $b = 1.00 \text{ in.}$   
 $c = 1.00 \text{ in.}$

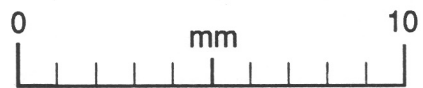
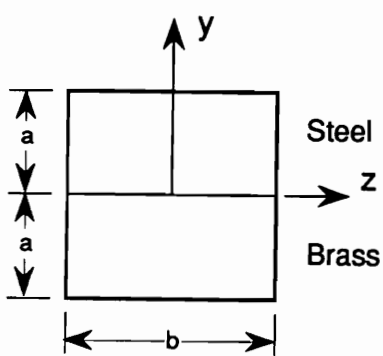
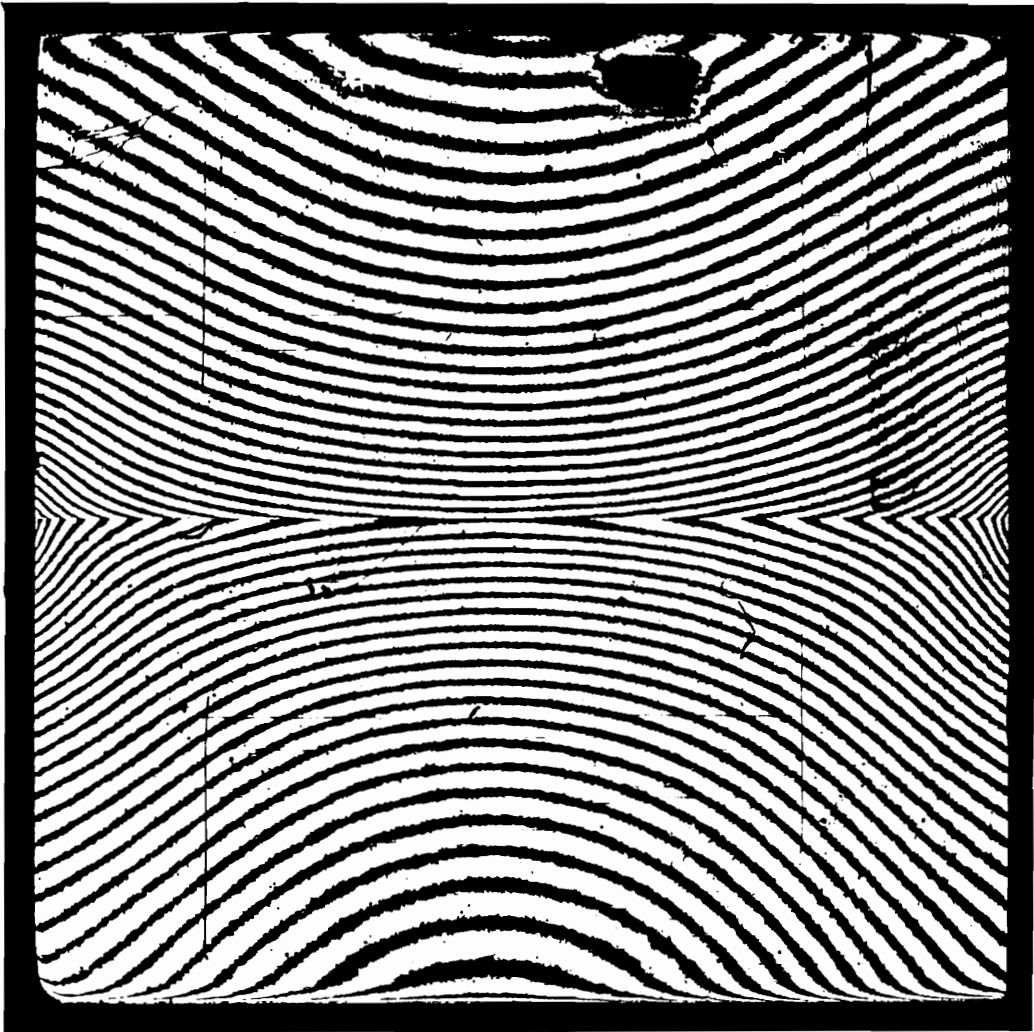


Figure 32.  
 Specimen-B. V-displacement field,  
 showing contours of total displacements  
 perpendicular to the interface.



$a = 0.50 \text{ in.}$   
 $b = 2.00a$   
 $c = 2.00a$



Figure 33.

Specimen-B. V-displacement field (Figure 32) modified by carrier fringes that subtract off the average of the free thermal expansions of the two materials.

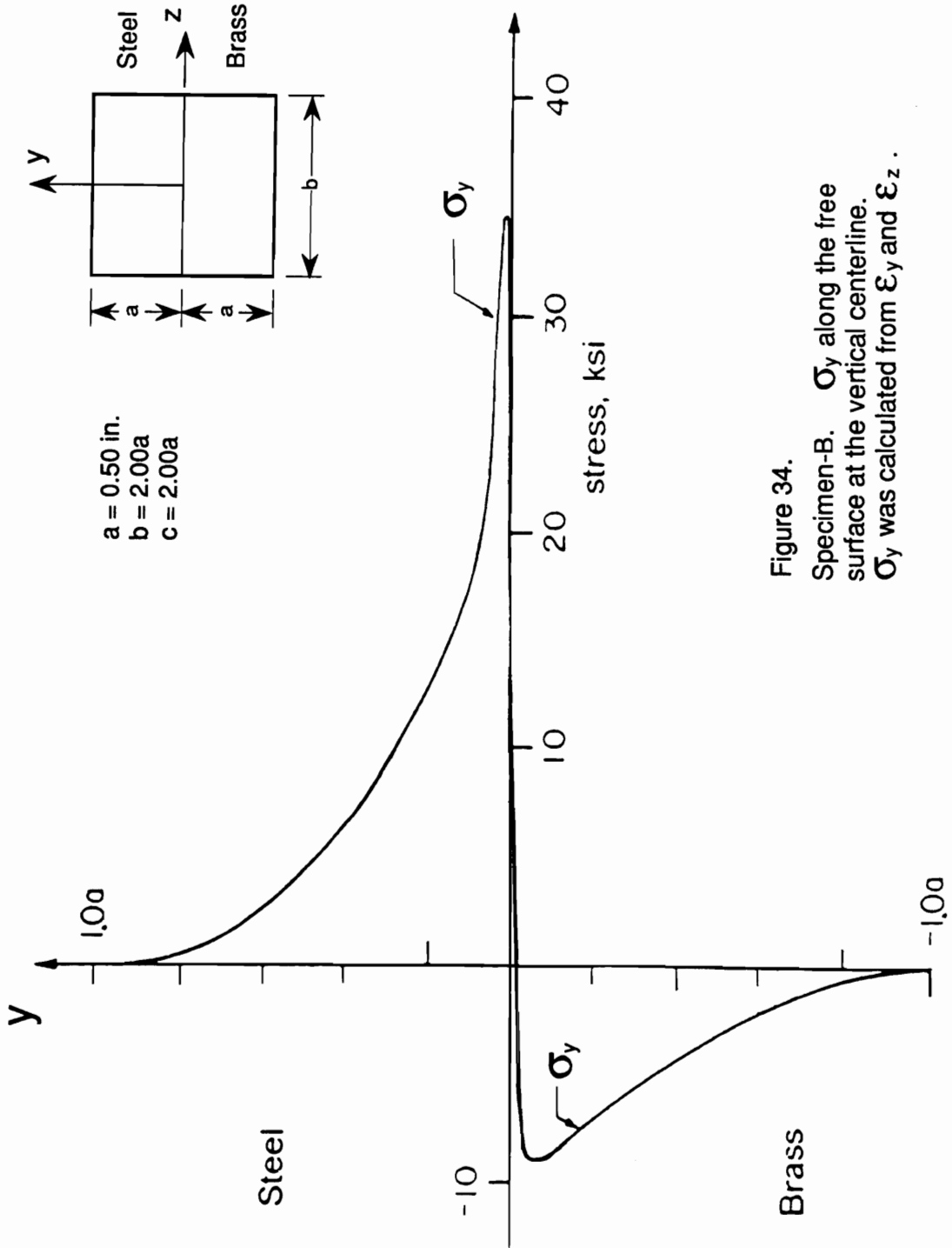


Figure 34.  
 Specimen-B.  $\sigma_y$  along the free surface at the vertical centerline.  $\sigma_y$  was calculated from  $\epsilon_y$  and  $\epsilon_z$ .

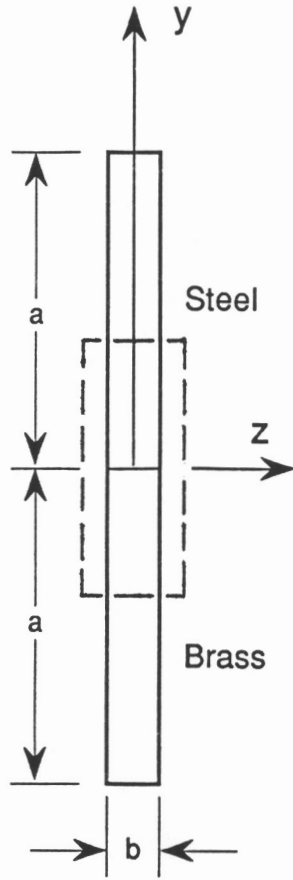
The  $\sigma_y$  curves in Figure 34 and Figure 37 were calculated from the moiré data and Eq. (10). Because  $\varepsilon_x$  is essentially constant in the interface zone (near  $y'$ ), the location of peak values of  $\varepsilon_y$  coincides with the peak values of  $\sigma_y$ .

**Table 8. Effect of geometric aspect ratio on turn-around-point.**

Specimen	Turn-around-point distance from the interface		interface zone width total $\Delta y$	Aspect Ratio		
	Brass $\Delta y$	Steel $\Delta y$		$a/b$	$a/c$	$b/c$
B	1000 $\mu m$ (0.040 in.)	200 $\mu m$ (0.008 in.)	1200 $\mu m$ (0.048 in.)	0.50	0.50	1.00
C	430 $\mu m$ (0.017 in.)	< 60 $\mu m$ (< 0.002 in.)	< 490 $\mu m$ (< 0.019 in.)	6.77	0.25	0.037
D	25 $\mu m$ (0.001 in.)	25 $\mu m$ (0.001 in.)	50 $\mu m$ (0.002 in.)	0.50	6.85	13.8

Table 8 gives the relationship between the geometric aspect ratio and the *turn-around-point* for each of the specimens tested. The width of the interface zone (given as the distance between maximum and minimum peak stresses) is also given. Results shown for Specimen-D are taken from Chapter 5.

The width of the interface zone must be a function of the specimen-aspect ratios. However, the specimen with the widest interface zone (Specimen-B) does not have the highest or lowest aspect ratio. This can be explained by the three-dimensional nature of this problem. The measurements made along the centerline of Specimen-C contained the additional influence of the *critical corner*, because of the narrow width of the specimen. The measurements from the other two specimen geometries were not affected by the additional influence of the *critical*

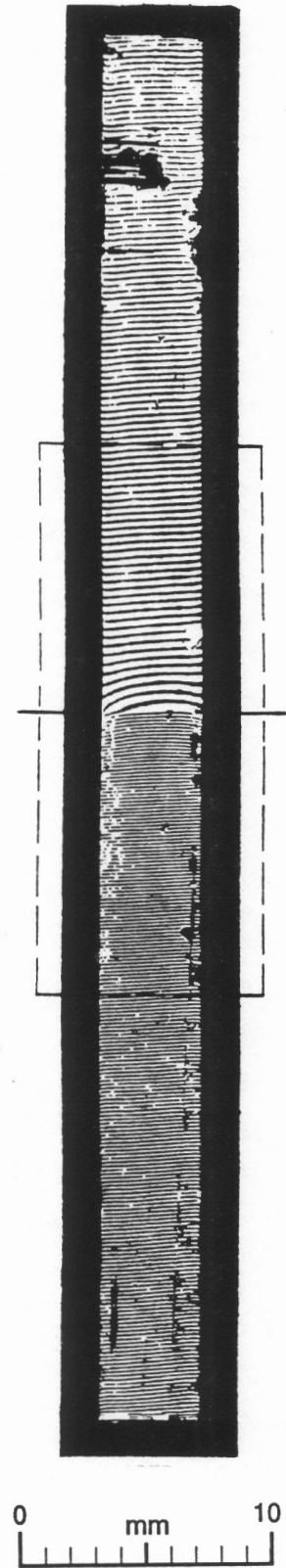


$$a = 1.10 \text{ in.}$$

$$b = 0.15a$$

Figure 35.

Specimen-C. V-displacement field, showing displacements in the  $y$  direction, perpendicular to the interface. Figure 36 presents the displacement fields inside the dashed region at a higher magnification.



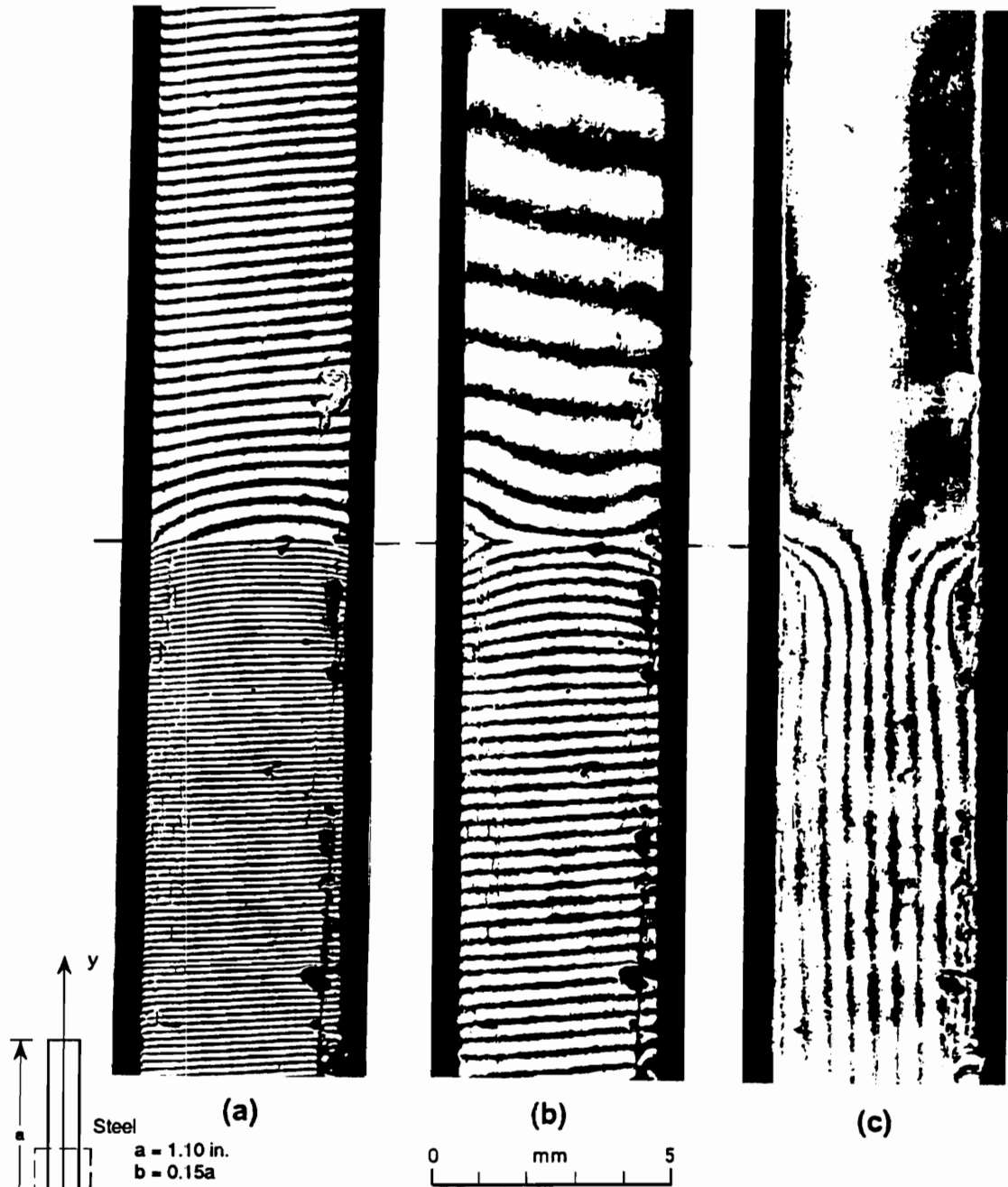


Figure 36.

Specimen-C. (a) V-displacement field with no carrier. (b) the same V-displacement field as (a), modified by carrier fringes that subtract off the free thermal expansion of the steel. (c) The W-displacement field modified by carrier fringes that correlate to (b).



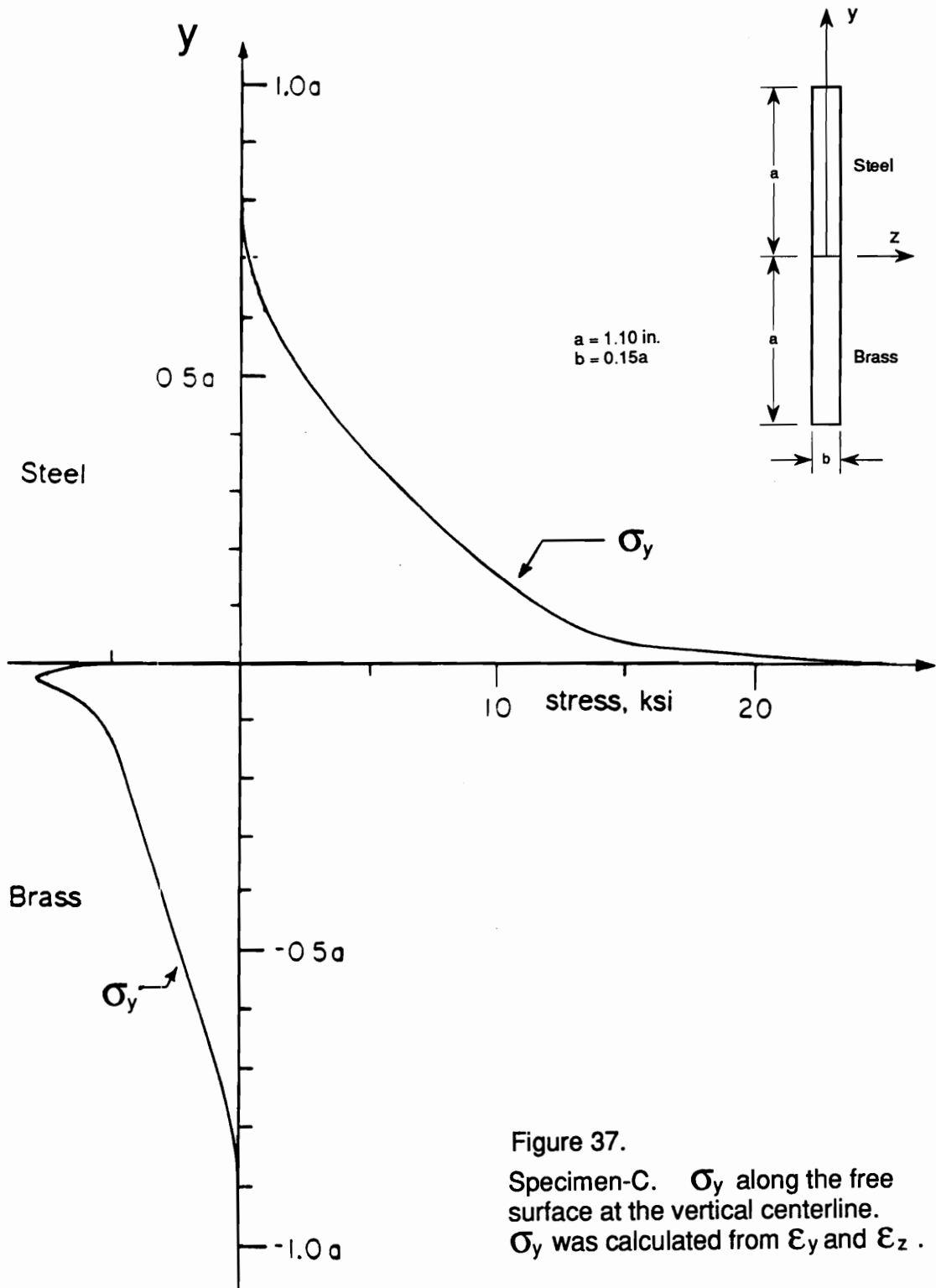


Figure 37.  
 Specimen-C.  $\sigma_y$  along the free surface at the vertical centerline.  
 $\sigma_y$  was calculated from  $\epsilon_y$  and  $\epsilon_z$ .

corner. This is illustrated schematically in Figure 6(e) on page 16, where  $\sigma_y^{(relative)}$  is higher at the center of the narrow face than at the center of the wide face.

## 4.4 Summary of Results

The surface stresses in a bimaterial metal joint subjected to a uniform temperature change were determined experimentally. Surface strains,  $\varepsilon_x$ ,  $\varepsilon_y$ , and  $\gamma_{xy}$  were determined on a whole-field basis. Stresses were calculated using known mechanical properties. Dependable whole-field measurements were made in regions outside of a  $\pm 100 \mu\text{m}$  wide zone near the interface, using *macroscopic* moiré interferometry. Large tensile and compressive stresses were documented on opposite sides of the interface. Comprehensive results were plotted for Specimen A. Normal stresses,  $\sigma_y$  were plotted for specimens B and C.

The stress distributions were akin to those of *singular* solutions (i.e. stresses approaching  $\infty$ ), but in the physical experiment, the stresses reached finite peak values of opposite signs. Thereupon, their magnitudes decreased precipitously in a very narrow interface zone, a zone of about  $1200 \mu\text{m}$  (0.050 in.) width for Specimen-B, and  $500 \mu\text{m}$  (0.020 in.) width for Specimen-C. However, for Specimen A, the paths of the fringes were inconclusive by this method and required further investigation to demonstrate continuity of the stress distribution for  $\sigma_y$ .

In order to assess the distribution of  $\varepsilon_y$  in the immediate vicinity of the interface, a special technique (described in *Section 4.2*) was used to increase the sensitivity of this *macroscopic* moiré interferometry method. The fringes are clearly delineated outside the interface zone, for all three specimen geometries.

## Chapter 5

### Chapter 5: Interpretation and Discussion

#### 5.1 *Stresses within the Interface Zone, Specimen A,D*

In order to assess the distribution of  $\sigma_y$  in the immediate vicinity of the interface, the sharpness of the chevron-like fringes of Figure 24(b) must be evaluated. The fringes are clearly delineated outside the interface zone. Within the tiny interface zone, however, the paths of the fringes are inconclusive. If the clearly delineated fringes in the steel and brass are extrapolated to the interface with a monotonically decreasing inclination, or else with a constant inclination, then the peak values of  $\sigma_y$ , in both materials would occur at the interface (where  $y = 0$ ). A physically inadmissible condition would result, where  $\sigma_y$ , at each interface point, would have two distinct values and where vertical equilibrium would be violated.

On the other hand, if the fringes change their course and bend toward the interface, the curve of  $\sigma_y$  vs.  $y'$  would reach peak positive and negative values at some small distance from the interface. The curve would then turn sharply away from the peaks and progress in the interface zone with finite slopes between the peak values. The following analysis relates the fringe inclination in Figure 24(b) to  $\sigma_y$ .

Close to the interface, the behavior of  $\sigma_y$  hinges upon the behavior of  $\varepsilon_y^\sigma$ . This exclusive dependence occurs because  $\varepsilon_x^\sigma$  is (essentially) constant within the 100  $\mu m$  interface zone, Figure 28, and it can be treated as a constant in Equation (10). The behavior of  $\varepsilon_y^\sigma$  can be elicited from Figure 24(b). The fringe orders  $N_y$ , marked in the figure, represent

$$N_y = N_y^\sigma + \alpha \Delta T - N_y^c$$

where superscript "c" denotes carrier fringes. The gradients of these fringes are related to  $\varepsilon_y^\sigma$ , through Equation (5), by

$$\frac{1}{f} \frac{\partial N_y}{\partial y} = \frac{1}{f} \frac{\partial N_y^\sigma}{\partial y} + k_1 = \varepsilon_y^\sigma + k_1 \quad (14)$$

where  $k_1$  is a constant, representing the combined effect of  $\alpha \Delta T$ , and the carrier fringes. The fringe order  $N_y = 0$  is chosen arbitrarily in Figure 24(b), since only relative displacements are required for strain analysis.

Along  $y'$ ,  $\partial N_y / \partial y$  is positive in the steel. It can be determined by

$$\frac{1}{f} \frac{\partial N_y}{\partial y} = \frac{1}{f} \frac{\partial N_y}{\partial x} \tan \phi = k_2 \tan \phi,$$

since  $\tan \phi = dx/dy$ , where  $\phi$  is the angle from a line parallel to the  $y$  axis to the tangent to the fringe, and where  $k_2$  is a constant. The derivative  $\partial N_y/\partial x$  can be considered a constant, as corroborated by Figure 27(c), which indicates that near the interface its variation along  $y'$  is essentially zero. Accordingly,

$$\varepsilon_y^\sigma = k_2 \tan \phi - k_1. \quad (15)$$

Since  $\varepsilon_x^\sigma$  can be treated as a constant within the interface zone, Equations (10) and (15) provide, for that zone,

$$\sigma_y = k_3 \tan \phi - k_4, \quad (16)$$

where  $k_3$  and  $k_4$  are combined constants.

The same argument applies to  $\sigma_y$ , in the brass, where  $\partial N_y/\partial y$  is negative and correspondingly,  $\phi$  is negative. Thus,  $\sigma_y$  has opposite signs in the steel and brass. And again, the magnitude of  $\sigma_y$  increases as  $|\phi|$  increases. Thus,  $\sigma_y$  reaches opposite peak values (tensile and compressive) as the interface is approached from the steel and brass.

## 5.2 Supplementary Experiment

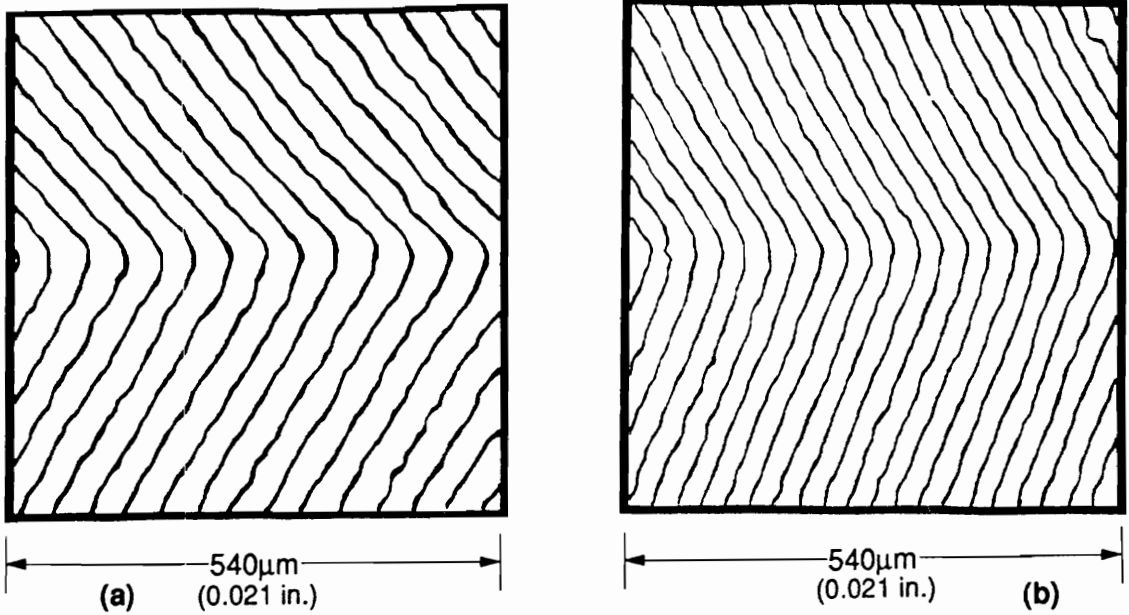
Since  $\sigma_y$  depends critically upon  $\phi$  in the narrow interface zone of Figure 24(b), and the shape of the fringes in that zone remains uncertain, additional experimental evidence to characterize  $\sigma_y$ , was sought by the method of *microscopic moiré* interferometry (Han and Post

[116], and Han [117]). With this method, an immersion interferometer provided a two-fold increase of basic sensitivity, utilizing a virtual reference grating of 4800 lines/mm (122,000 lines/in.). Phase shifting and optical/digital fringe sharpening and multiplication provided contour maps of displacements with contour intervals of 52 nm/fringe contour.

*Microscopic* fields of view of 540 and 310  $\mu\text{m}$  (0.021 and 0.012 in.) widths were observed, spanning the interface region. The measurement sensitivity was eight times greater than that of the *macroscopic* analysis, equal to the sensitivity of moiré with 19,200 lines/mm (487,680 lines/in.) i.e.  $f_1 = 19,200$  lines/mm.

The same specimen as that of Figure 14 on page 30 was used, except its width and height were cut to half of the previous dimensions. The specimen grating was applied at elevated temperature, as before, and observed at room temperature to reveal the stress-induced thermal deformation. The specimen grating was applied at the center of the specimen, as shown in Figure 17 on page 34, and as depicted in Figure 38. This change from the quarter-width position of  $y'$  is permissible since  $\sigma_y$  is independent of  $x$  in these regions. Replication of the specimen grating in this small region of interest was achieved with a much smaller grating thickness, approximately 2  $\mu\text{m}$  thickness in this case. Accordingly, the shear-lag deformation that occurs through the grating thickness in the vicinity of high-strain gradients, is now expected to affect a zone of about 10  $\mu\text{m}$  (0.0004 in.) width near the interface, i.e.,  $\pm 5 \mu\text{m}$ . Authentic results can be expected at locations twenty-times closer to the interface than in the *macroscopic* experiment.

The resulting fringe contours are shown in Figure 38, which represent the thermal deformations plus carrier fringes. The carrier fringes were applied again to emphasize the changes near the interface. Carrier fringes of extension, subtracted off the average (approximately) of the fringe gradients in the steel and brass, as before, (similar to Figure 22 on page



Displacement = 52 nm/fringe contour

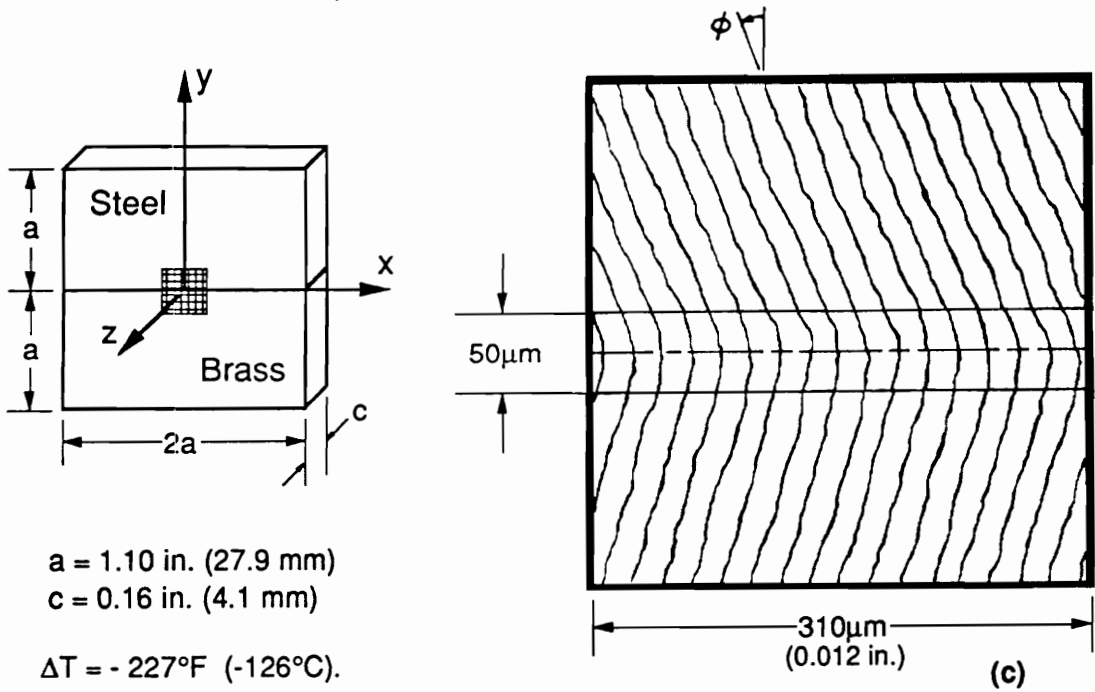


Figure 38. Patterns corresponding to Figure 24b, but with higher sensitivity and resolution, produced by microscopic moiré interferometry. The patterns differ by the amount of carrier of rotation and magnification.

47). Carrier fringes of rotation were applied to clearly delineate the fringe contours near the interface. Note that the carrier of extension adds a constant, apparent strain to  $\varepsilon_y^c$ , as provided in Equation (14), and that the carrier fringes of rotation are parallel to the  $y$  axis and have no influence on  $\partial N_y/\partial y$  and also have no influence on  $\varepsilon_y^c$ . The interface is indicated by the broken line in Figure 38. Its location relative to the contour map was determined by *microscopic* inspection.

The patterns show a distinct decrease of  $|\phi|$  in a  $50\ \mu\text{m}$  (0.002 in.) zone, which proves that the curves of  $\varepsilon_y^c$  for the steel and brass turn-around from their peak values and move towards each other in a very narrow zone of extremely-high stress gradients. By Equation (10), and knowledge that  $\varepsilon_x$  is essentially constant in this zone,  $\sigma_y$  must follow the same trend. The distribution of  $\sigma_y$  is illustrated in Figure 39, where the vertical scale is greatly magnified. The axis is marked  $y'$ , but the results apply along most of the interface zone as indicated in Figure 30 and as discussed above. The dashed line recognizes the remaining uncertainty in the high-gradient region. The region of uncertainty is now diminished by nearly an order of magnitude, and a monotonic variation of  $\sigma_y$  within the region can be rationalized with substantial confidence. The *microscopic* analysis indicates that a  $\sigma_y$  curve near the interface is always single-valued, i.e., the curve has a finite slope, and the potential equilibrium imbalance is eliminated. The stress gradients are high, but they are finite.

In Figure 38, the fringe contours outside the  $50\ \mu\text{m}$  zone are nearly straight on the brass side. Correspondingly, the stress in Figure 39 is nearly constant in the same portion of the specimen. On the steel side, the fringes are concave. Angle  $\phi$  increases as the  $50\ \mu\text{m}$  zone is approached, and this translates to the corresponding increase of  $\sigma_y$  revealed in Figure 39. The peak value of  $\sigma_y$  in the steel obtained from Figure 24 was slightly lower, but the result of the *microscopic* analysis has been incorporated into the curves of Figure 28, Figure 29, and Figure 30.



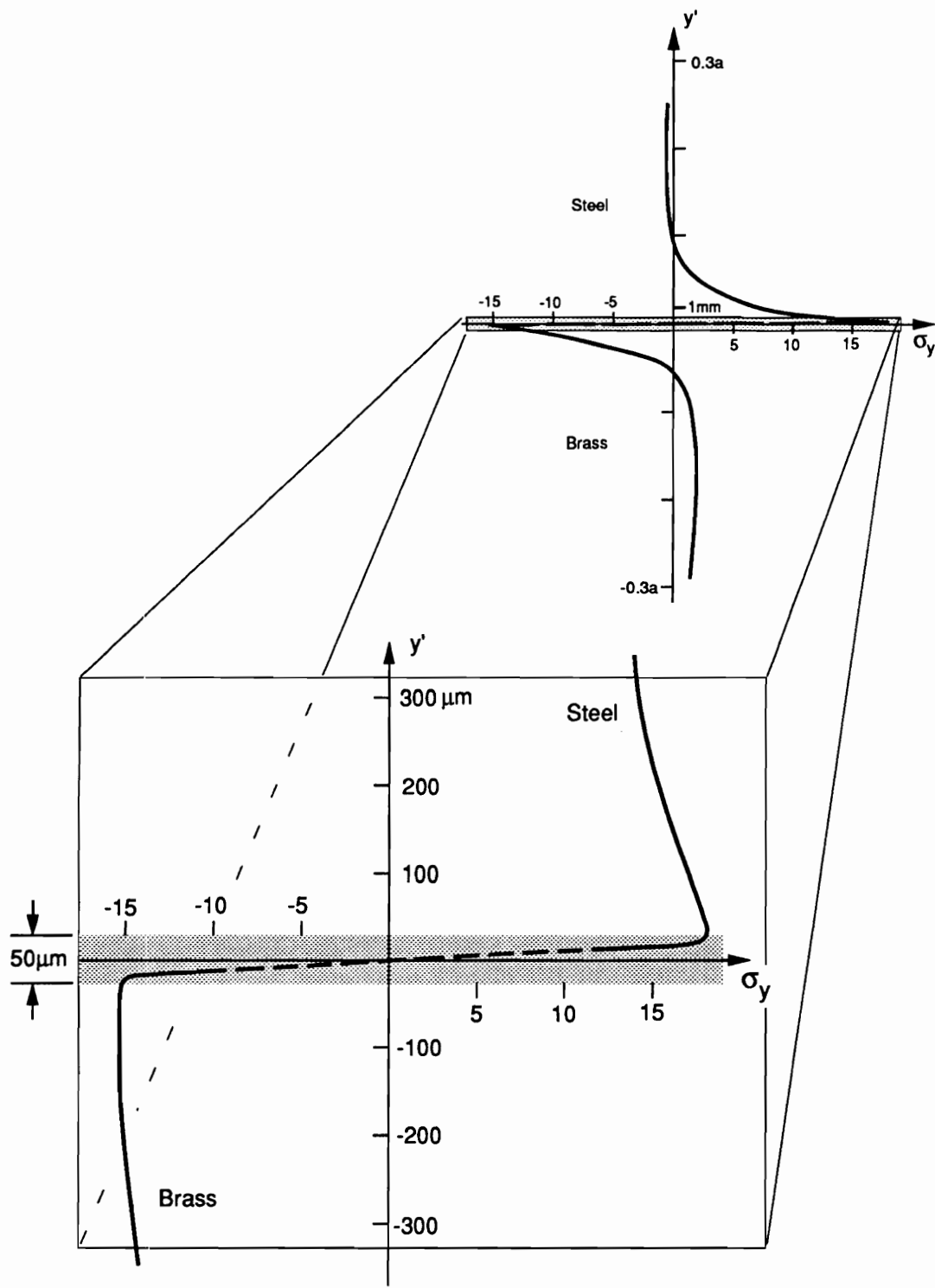


Figure 39. The distribution of  $\sigma_y$  near the interface. The stress units are psi when the numbers are multiplied by 1000, and MPa when multiplied by 6.9.

### 5.3 Discussion

Note that  $\partial N_y / \partial x$  is not affected by the fringe curvature in the interface zone. Note, too, that there is no corresponding uncertainty for the  $N_x$  fringes. Accordingly, the  $\sigma_x$  and  $\tau_{xy}$  curves in Figure 29 extend to the interface, where  $y' = 0$ .

It is interesting to observe the similarity of stress distributions in Figure 29, Figure 30, and Figure 31, for the steel and brass elements. When the joined body experiences a temperature change, one element tends to expand relative to the other. The dominant constraint that restricts the relative expansion, is a system of shear forces. At each point on the interface, the shear forces acting on the steel and the brass are equal in magnitude and opposite in direction. If we consider the steel and brass parts separately, and if we consider only these shear forces, we see that the parts have identical geometry and exactly opposite force systems. Since the stresses in an elastic body depend only upon the forces and body geometry, these forces generate equal stress distributions in the steel and brass, but of opposite signs. Indeed, the results in Figure 29, Figure 30, and Figure 31 show approximately equal and opposite stress distributions in the steel and brass.

The theoretical singularities predicted in the literature cannot occur in real joints that maintain their structural integrity. Nevertheless, it is seen that the experimentally determined stresses mimic the singular solutions to a substantial degree. Very near the interface, however, the asymptotic rise of a singular stress is replaced by a reversal and an extremely rapid decrease of the normal stress,  $\sigma_y$ .

## Chapter 6

### Chapter 6: Conclusions

The stress distribution near a bimaterial metal interface subjected to a uniform temperature change were determined experimentally. Surface strains,  $\varepsilon_x$ ,  $\varepsilon_y$ , and  $\gamma_{xy}$  determined on a whole-field basis. Stresses were calculated using known mechanical properties. Dependable whole-field measurements were made in regions outside of a  $\pm 100 \mu\text{m}$  wide zone near the interface, using *macroscopic* moiré interferometry. Large tensile and compressive stresses were documented on opposite sides of the interface. *Microscopic* moiré interferometry was used to characterize the stresses in the interface zone to within  $\pm 5 \mu\text{m}$  of the interface.

The stress distributions were akin to those of *singular* solutions (i.e. stresses approaching  $\infty$ ), but in the physical experiment, the stresses reached finite peak values of opposite signs. Thereupon, their magnitudes decreased precipitously in an extremely narrow interface zone, a zone of about  $50 \mu\text{m}$  (0.002 in.) width, for Specimen-A/Specimen-D,  $1200 \mu\text{m}$  (0.048 in.) width for Specimen-B, and  $<490 \mu\text{m}$  ( $<0.019$  in.) width for Specimen-C. This very strong tension-

compression stress system and the very strong stress gradient occurred along the entire length of the interface and it can be assumed to prevail along the entire perimeter of the joint.

A localized, but strong stress-strain disturbance was observed in the corner region where the two free edges intersected. The experiments represent the analysis of a fully three-dimensional, bimaterial joint, thermal-stress problem. Both *macroscopic* and *microscopic* moiré interferometry were required to extract the stress distribution.

## References

1. Timoshenko, S., "Analysis of Bimetal Thermostats," *J. Optical Society of America*, v.11, n.3 (Sept. 1925) pp.233-255.
2. Goland, M. and Reissner, E., "The Stresses in Cemented Joints," *J. Applied Mechanics*, v.11 (1944) pp.A17-A27.
3. Boley, B.A. and Weiner, J.H., *Theory of Thermal Stresses*, Wiley, New York (1967).
4. Boley, B.A. and Testa, R.B., "Thermal Stresses in Composite Beams," *Int. J. Solids and Structures*, v.5 (1969) pp.1153-1169.
5. Chen, W.T. and Nelson, C.W., "Thermal Stress in Bonded Joints," *IBM J. Res. Develop.*, v.23, n.2 (1979) pp.179-188.
6. Wittmer, M., Boer, C.R., and Gudmundson, P., "Mechanical Properties of Liquid-Phase-Bonded Copper-Ceramic Substrates," *J. American Ceramic Society*, v.65, n.3 (March 1982) pp.149-153.
7. Hsueh, C.H. and Evans, A.G., "Residual Stresses in Metal/Ceramic Bonded Strips," *J. American Ceramic Society*, v.68, n.5 (1985) pp.241-248.
8. Suhir, E., "Stresses in Bi-Metal Thermostats," *J. Applied Mechanics*, v.53 (1986) pp.657-660.
9. Kunz, Stephanie C. and Loehman, Ronald E., "Thermal Expansion Mismatch Produced by Interfacial Reactions in Glass-Ceramic to Metal Seals," *ACM*, v.2, n.1 (1987) pp.69-73.
10. Hess, Milton S., "The End Problem for a Laminated Elastic Strip - I. The General Solution," *J. Composite Materials*, v.3 (March. 1969) pp.262-280.
11. Hess, Milton S., "The End Problem for a Laminated Elastic Strip - II. Differential Expansion Stresses," *J. Composite Materials*, v.3 (Oct. 1969) pp.630-641.

12. Grimado, P.B., "Interlaminar Thermoelastic Stresses in Layered Beams," *J. Thermal Stresses*, v.1, n.1 (1978) pp.75-86.
13. Choi, I., and Horgan, C.O., "Saint-Venant End Effects for Plane Deformation of Sandwich Strips," *International Journal of Solids and Structures*, v.14 (1978) pp.187-195.
14. Dempsey, J.P. and Sinclair, G.B., "On the Singular Behavior at the Vertex of a Bi-material Wedge," *J. Elasticity*, v.11, n.3 (July 1981) pp.317-327.
15. Wang, S.S. and Choi, I., "Boundary Layer Effects in Composites Laminates: Part I. - Free Edge Stress Singularities" and "Part II. - Free Edge Stress Solutions and Basic Characteristics," *J. Applied Mechanics*, v.49 (Sept. 1982) pp.541-560.
16. Bogy, D.B., and Sternberg, Eli, "The Effect of Couple-Stresses on Singularities Due to Discontinuous Loadings," *Int. J. of Solids and Structures*, v.3 (1967) pp. 757-770.
17. Hein, V.L., "Residual Stresses in a Two-Material Wedge and a Finite Cylinder," Ph.D. Thesis, Lehigh University (1968).
18. Hein, V.L. and Erdogan, F., "Stress Singularities in a Two-Material Wedge," *Int. J. of Fracture Mechanics* v.7, n.3 (Sept. 1971) pp.317-330.
19. Bogy, D.B., and Sternberg, Eli, "The Effect of Couple-Stresses on the Corner Singularity due to an Asymmetric Shear Loading," *Int. J. of Solids and Structures*, v.4 (1968) pp.159-174.
20. Bogy, David B., "Edge-Bonded Dissimilar Orthogonal Elastic Wedges Under Normal and Shear Loading," *J. Applied Mechanics*, v.35 (Sept. 1968) pp.460-466.
21. Bogy, D.B., "On the Problem of Edge-Bonded Elastic Quarter Planes Loaded at the Boundary," *Int. J. of Solids and Structures*, v.6 (1970) pp.1287-1313.
22. Bogy, D.B., "Two Edge-Bonded Elastic Wedges of Different Materials and Wedge Angles Under Surface Traction," *J. Applied Mechanics*, v.38, n.2 (June 1971) pp.377-386.
23. Bogy, D.B., and Wang, K.C., "Stress Singularities at Interface Corners in Bonded Dissimilar Isotropic Elastic Materials," *Int. J. Solids Structures*, v.7 (1971) pp.993-1005.
24. Bogy, D.B., "On the Plane Elastostatic Problem of a Loaded Crack Terminating at a Material Interface," *J. Applied Mechanics*, v.38 (Dec. 1971) pp.911-918.
25. Kuo, M.C., and Bogy, D.B., "Plane Solutions for the Displacement and Traction-Displacement Problems for Anisotropic Elastic Wedges," *J. Applied Mechanics*, v.41 (March 1974) pp.197-202.
26. Kuo, M.C., and Bogy, D.B., "Plane Solutions for Traction Problems on Orthotropic Unsymmetrical Wedges and Symmetrically Twinned Wedges," *J. Applied Mechanics*, v.41 (March 1974) pp.203-208.
27. Bogy, D.B., "The Plane Solution for Joined Dissimilar Elastic Semistrips Under Tension," *J. Applied Mechanics*, v.42 (Mar. 1975) pp.93-98.
28. Cheng, Shun and Gerhardt, T.D., "Laminated Beams of Isotropic or Orthotropic Materials Subjected to Temperature Change," Forest Products Laboratory, Research paper FPL375 (June 1980).

29. Chen, Du, Cheng, S., and Gerhardt, T.D., "Thermal Stresses in Laminated Beams," *J. Thermal Stresses*, v.5 (1982) pp.67-84.
30. Sawa,Toshiyuki, Temma,Katsuhiko, Tsunoda,Yuuichi, and Ishikawa,Hirohisa, "Three-Dimensional Stress Analysis of Adhesive Butt Joints Subjected to Tensile Loads (Adhesion of Dissimilar Solid Cylinders)," *Nihon Kikai Gakkai Rombunshu*, v.55, n.509 (January 1989) pp.73-78, (*In Japanese*).
31. Suganuma, K., Okamoto, T., and Koizumi, M., "Effect of Interlayers in Ceramic-Metal Joints with Thermal Expansion Mismatches," *J. American Ceramic Society*, v.67, n.12 (1984) pp.C256-C257.
32. Blanchard, J.P. and Watson, R.D., "Residual Stresses in Bonded Armor Tiles for In-Vessel Fusion Components," *Nuclear Engineering and Design/Fusion*, v.4 (1986) pp.61-66.
33. Fukumoto,Masahiro, Torii,Kouji, and Okane,Isao, "Thermal Stress Analysis in Ceramics-Metal Solid State Bonding Process," *Nihon Kakai Gakkai Rombunshu*, v.53, n.496 (December 1987) pp.2724-2728, (*In Japanese*).
34. Gerstle, F.P. and Chambers, R.S., "Analysis of End Stresses in Glass-Metal Bimaterial Strips," *Proceedings of Symposium on Technology of Glass, Ceramic, or Glass-Ceramic to Metal Sealing, 1987 ASME Winter Meeting, Dec. 13-18, (1987) Boston, Ma.*
35. Miyagawa,Matsuo, Yada,Toshio, Koguchi,Hideo, and Honzawa,Toyoshige, "Reliability Evaluation of Joints of Ceramics and Metal (1<sup>st</sup> Report, Consideration on Thermoelastic-Plastic Stress Around the Interface of Joined Dissimilar Materials)," *Nihon Kikai Gakkai Rombunshu*, v.54, n.507 (November 1988) pp.1949-1955, (*In Japanese*).
36. Yada,Toshio, Koguchi,Hideo, Honzawa,Toyoshige, Kaya,Toshinori, and Miyagawa,Matsuo, "Reliability Evaluation of Joints of Ceramics and Metals (2<sup>nd</sup> Report, The influence of Changing the Shape of a Joint on the Thermal Stress of Joined Dissimilar Materials)," *Nihon Kikai Gakkai Rombunshu*, v.54, n.508 (December 1988) pp.2128-2134, (*In Japanese*).
37. Terasaki,Toshio, Seo,Kenji, and Hirai,Takayuki, "Dominating Parameters of Residual Stress Distribution, Residual Stress in Bonded Dissimilar Materials, Part 1," *Yosetsu Gakkai Ronbunshu*, v.5, n.4 (November 1987) pp.103-107 (also numbered pp.533-537), (*In Japanese*).
38. Terasaki,Toshio, Hirai,Takayuki, and Seo,Kenji, "Effect of Material Constant and Specimen Size on Residual Stress, Residual Stress in Bonded Dissimilar Materials (Part II)," *Yosetsu Gakkai Ronbunshu*, v.6, n.2 (1988) pp.88-92 (also numbered pp.284-288), (*In Japanese*).
39. Rosenberg, J.E. and Langerman, A, "A Method and Apparatus for Studying the Physical Properties of Vitreous Enamels on Steel," *J. American Ceramics Society*, v.19, n.3 (1936) pp.86-90.
40. Bryant,E.E. and Ammon,M.G., "Determination of Compressive Stress Present in Porcelain Enamel on Sheet Iron," *J. of the Am. Ceramic Society*, v.31, n.1 (Jan. 1948) pp.28-30.
41. Walton, J.D., and Sweo, B.J., "Determination of Strains Between Enamel and Iron by Means of Split Rings," *J. American Ceramic Society*, v.36, n.10 (Oct. 1953) pp.335-341.

42. Walton, Jr., J.D. "Study of Strains Between Enamel and Iron as Related to Physical Properties of Each," *J. American Ceramic Society*, v.37, n.3 (March 1954) pp.153-160.
43. Lauchner, J.H., Cook, R.L., and Andrews, A.I., "Fundamental Thermal Deflection Analysis of Enamel-Metal Systems," *J. American Ceramic Society*, v.39, n.8 (1956) pp.288-292.
44. Inge, J.E., and Swanson, J.E., "Experimental Investigation of Stresses in a Ceramic-to-Metal Brazed Joint," *Experimental Mechanics*, v.2 (Oct. 1962) pp.289-295.
45. Alwar, R.S., "Experimental Verification of Saint-Venant's Principle in a sandwich beam," *AIAA J.*, v.8, (1970) p.160: (see also discussion, *AIAA J.*, v.8 (1970) p.1535).
46. Suganuma, K., Okamoto, T., Koizumi, M., and Shimada, M., "Acoustic Emission from Ceramic/Metal Joints on Cooling," *Am. Ceramic Society Bulletin*, v.65, n.7 (1986) pp.1060-1064.
47. Suganuma, K., Okamoto, T., Koizumi, M., and Kamachi, K., "Influence of Shape and Size on Residual Stress in Ceramic/Metal Joining," *J. Material Science* v.22, n.10 (October 1987) pp.3561-3565.
48. Suganuma, K., Okamoto, T., and Kamachi, K., "Influence of Shape and Size on Residual Stress in Ceramic/Metal Joining," *J. Material Science* v.22, n.8 (1987) pp.2702-2706.
49. Parks, Vincent J., "Stresses in a Bonded Wafer," *Experimental Mechanics*, v.28, n.1 (March 1988) pp.77-85.
50. Leitner, G., Balke, H., Schuster, K.F., Storbeck, I., and Wolf, M., "In Situ Investigation of Distortion of Multilayer Structures at Elevated Temperatures," *J. Thermal Analysis*, v.33, n.3 (August 1988) pp.871-874.
51. Wah, Thein, "Stress Distribution in a Bonded Anisotropic Lap Joint," *J. of Engineering Materials and Technology*, v.95 (1973) pp.174-181.
52. Keer, L.M. and Chantaramungkorn, K., "Stress Analysis for a Double Lap Joint," *J. Applied Mechanics*, v.42 (June 1975) pp.353-357.
53. Delale, F., Erdogan, F., and Aydingoglu, M.N., "Stresses in Adhesively Bonded Joints: A Closed-Form Solution," *J. Composite Materials*, v.15 (May 1981) pp.249-271.
54. Adams, R.D. and Peppiatt, N.A., "Effect of Poisson's Ratio Strains in Adherends on Stresses of an Idealized Lap Joint," *J. Strain Analysis*, v.8, n.2 (1973) pp.134-139.
55. Adams, R.D. and Peppiatt, N.A., "Stress Analysis of Adhesive-Bonded Lap Joints," *J. Strain Analysis*, v.9, n.3 (1974) pp.185-196.
56. Post, D., Czarnek, R., Wood, J.D., and Joh, D., "Deformations and Strains in a Thick Adherent Lap Joint," *Adhesively Bonded Joints: Testing, Analysis, and Design, ASTM STP 981*, W.S. Johnson, Ed., American Society for Testing and Materials, Philadelphia (1988) pp.107-118.
57. Adams, R.D., Chambers, S.H., Del Strother, P.J.A., and Peppiatt, N.A., "Rubber Model for Adhesive Lap Joints," *J. Strain Analysis*, v.8, n.1 (1973) pp.52-57.
58. Davidson, R., Post, D., and Boeman, R., "The Application of Laser Moiré Techniques to the Measurement of Shearing Effects in Laminated Structures," *Proceedings of Applied Solid Mechanics, III*, Guilford, England (April 6, 1989).



59. Seo, Kenji, Kusaka, Masahiro, Nogata, Fumio, Terasaki, Tosio, Nakao, Yosikuni, and Saida, Kazuyosi, "Study on the Thermal Stress at Ceramics-Metal Joint," *Nihon Kikai Gakkai. in: Nihon Kikaisakkai rombunsh u..* v.55, n.510 (February 1989) pp.312-317, (in Japanese).
60. Herakovich, C. T. "On the Relationship Between Material Properties and Delamination of Composite Materials," *J. Composite Materials*, v. 15 (July 1981) pp.336-348.
61. Pagano, N.J. and Pipes, R.B., "Some Observations on the Interlaminar Strength of Composite Laminates," *Int. J. Mechanical Sciences* v.15 (1973) pp.679-688.
62. Hahn, H.T. and Pagano, N.J., "Curing Stresses in Composite Laminates," *J. Composite Materials*, v.9 (Jan. 1975) pp.91-106.
63. Herakovich, Carl T., "On Thermal Edge Effects in Composite Laminates," *Int. J. Mechanical Sciences*, v.18, n.3-D (1976) pp.129-134.
64. Zwiars, R.I., Ting, T.C.T., and Spilker, R.L., "On the Logarithmic Singularity of Free-Edge Stress in Laminated Composites Under Uniform Extension," *J. Applied Mechanics*, v.49 (Sept. 1982) pp.561-569.
65. Puppo, A.H. and Evensen, H.A., "Interlaminar Shear in Laminated Composites Under Generalized Plane Stress," *J. Composite Materials*, v.4 (April 1970) pp.204-220.
66. Pipes, R. Byron, and Pagano, N.J., "Interlaminar Stresses in Composite Laminates Under Uniform Axial Extension," *J. Composite Materials*, v.4 (Oct. 1970) pp.538-548.
67. Pipes, R.B. and Pagano, N.J., "Interlaminar Stresses in Composite Laminates - An Approximate Elasticity Solution," *J. Applied Mechanics*, v.41, n.3 (Sept. 1974) pp.668-672.
68. Lau, C.W. and Delale, F., "Interfacial Stress Singularities at Free Edge of Hybrid Metal Matrix Composites," *J. of Engineering Materials and Technology*, v.110, n.1 (Jan. 1988) pp.41-47.
69. Alwar, R.S., and Nagaraja, Y.R., "Elastic Analysis of Adhesive Butt Joints," *J. of Adhesion*, v.7, (1976) pp.279-287.
70. Dempsey, J.P., and Sinclair, G.B., "On the Stress Singularities in the Plane Elasticity of the Composite Wedge," *J. of Elasticity*, v.9, n.4 (October 1979) pp.373-391.
71. Rao, A.K., "Stress Concentrations and Singularities at Interface Corners," *Zeitschrift für Angewandte Mathematik und Mechanik*, Band 51 (v.51) (1971) pp.395-406.
72. Aleck, B.J., "Thermal Stresses in a Rectangular Plate Clamped Along an Edge," *J. of Applied Mechanics*, v.16 (June 1949) pp.118-122.
73. Wah, T., "In-Plane Thermal Stresses in Elastic Plates," *J. of Strain Analysis*, v.19, n.2 (1984) pp.97-101.
74. Theocaris, P.S., and Dafermos, K., "The Elastic Strip Under Mixed Boundary Conditions," *J. of Applied Mechanics*, v.31 (December 1964) pp.714-716.
75. Hsu, P.W. and C.T. Herakovich, "Edge Effects in Angle-Ply Composite Laminates," *J. of Composite Materials*, v.11 (Oct. 1977) pp.422-428.

76. Hsu, P.W. and Herakovich, C.T., "A Perturbation Solution for Interlaminar Stresses in Composite Laminates," *Composite Materials Testing and Design*, (Forth Conference), ASTM STP 617, Am. Soc. for Testing and Materials (1977) p.296.
77. Pagano, N.J., "Free-Edge Stress Fields in Composite Laminates," *Int. J. Solids and Structures*, v.14 (1978) pp.401-406.
78. Wang and Choi, "Boundary-Layer Effects in Composite Laminate: Part 2 - Free-Edge Stress Solutions and Basic Characteristics," *J. Applied Mechanics*, v.49 (Sept. 1982) pp.549-560.
79. Erdogan, F., and Gupta, G.D., "Layered Composites with an Interface Flaw," *International J. of Solids and Structures*, v.7 (1971) pp.1089-1107.
80. Adams, R.D. and Harris, J.A., "The Influence of Local Geometry on the Strength of Adhesive Joints," *Int. J. of Adhesion and Adhesives*, v.7, n.2 (April 1987) pp.69-80.
81. Rybicki, E. F., "Approximate Three-Dimensional Solutions for Symmetric Laminates Under In-Plane Loading," *J. Composite Materials*, v. 5 (July 1971) 354-360.
82. Renieri, G.D., and Herakovich, C.T., "Nonlinear Analysis of Laminated Fibrous Composites," VPI-E-76-10 (June 1976) 177 pages.
83. Herakovich, C.T., Renieri, G.D., and Brinson, H.F., "Finite Element Analysis of Mechanical and Thermal Edge Effects in Composite Laminates," Army Symposium on Solid Mechanics, 1976, *Composite Materials: The Influence of Mechanics of Failure on Design*, Cape Cod, Mass. (Sept. 1976) pp.237-248.
84. Wang, A.S.D., and Crossman, F.W., "Some New Results on Edge Effects in Symmetric Composite Laminates," *J. Composite Materials*, v.11 (January 1977) p.92-106.
85. Reedy, Jr., E.D., "On Free-Edge Interlaminar Stress Distributions," *Composites Science and Technology*, v.34 (1989) pp.259-266.
86. Wang, A.S.D., and Crossman, Frank W., "Edge Effects on Thermally Induced Stresses in Composite Laminates," *J. Composite Materials*, v.11 (July 1977) pp.300-312.
87. Blevins, R.D., "Elastic Thermal Stresses in Bimetallic Pipe Welds," *J. of Pressure Vessel Technology*, v.102, n.4 (November 1980) pp.430-432.
88. Lee, Kang Yong and Choi, Hyung Jip, "Boundary Element Analysis of Stress Intensity Factors for Bimaterial Interface Cracks," *Engineering Fracture Mechanics*, v.29, n.4 (1988) pp.461-472.
89. Yuuki, Ryoji and Cho, Sang-Bong, "Boundary Element Analysis of Stress Intensity Factors for an Interface Crack in Dissimilar Materials," *Nihon Kikai Gakkai Rombunshu*, v.55, n.510 (February 1989) pp.340-347, (In Japanese).
90. Altus, E., Rotem, A., and Shmueli, M., "Free Edge Effect in Angle Ply Laminates - A New Three Dimensional Finite Difference Solution," *J. Composite Materials*, v.14 (Jan. 1980) pp.21-30.
91. Pagano, N.J. and J.C. Halpin, "Influence of End Constraint in the Testing of Anisotropic Bodies," *J. of Composite Materials*, v.2 (1968) p.18.

92. Pipes, R.B., and Daniel, I.M., "Moiré Analysis of the Interlaminar Shear Edge Effect in Laminated Composites," *J. Composite Materials*, v.5 (April 1971) pp.255-259.
93. Oplinger, D. W., Parker, B. S., and Chiang, F. P., "Edge-Effect Studies in Fiber-Reinforced Laminates," *Experimental Mechanics*, v.14, n.9 (Sept. 1974) pp.347-354.
94. Czarnek, R., Post, D. and Herakovich, C. T., "Edge Effects in Composites by Moiré Interferometry," *Experimental Techniques*, v.7, n.1 (Jan. 1983) pp.18-21.
95. Herakovich, C. T., Post, D., Buczek, M. B., and Czarnek, R., "Free Edge Strain Concentrations in Real Composite Laminates: Experimental-Theoretical Correlation," *Proceedings of the Winter Annual Meeting of the ASME*, Miami, Florida (Nov.13-17m 1985) pp.1-7 (paper no.85-WA/APM-10), and *J. Applied Mechanics*, v.52 (Dec. 1985) pp.787-793.
96. Wood,J.D., "Detection of Delamination Onset in a Composite laminate Using Moiré Interferometry," *J. Composites Technology and Research*, v.7, n.4 (Winter 1985) pp.121-128.
97. Fellows,R.L. and Novy,O.R., "Interpretation of Data Relating to Coefficient of Expansion of Various Types of Porcelain Enamels, Part I," *Better Enameling*, v.19, n.6 (June 1948) pp.6-11,35.
98. Fellows,R.L. and Novy,O.R., "Interpretation of Data Relating to Coefficient of Expansion of Various Types of Porcelain Enamels, Part II," *Better Enameling*, v.19, n.7 (July 1948) pp.6-11,33.
99. Post,D. and Wood,J., "Determination of Thermal Strains by Moiré Interferometry," *Experimental Mechanics* v.29, n.3, (Sept. 1989) pp.318-322.
100. Lauchner,J.H., Cook,R.L., and Andrews,A.I., "A New Technique for Simultaneous Recording of Strains and Temperature in Enamel-Metal Systems," *Am. Ceramic Society Bulletin*, v.34, n.4 (1955) pp.105-108.
101. Hatakeyama,F. Suganuma,K., Okamoto,T., "Solid-State Bonding of Alumina to Austenitic Stainless Steel," *J. of Materials Science*, v.21 (1986) pp.2455-2461.
102. Mylonas,C., "Experiments on Composite Models with Applications to Cemented Joints," *Proceedings of the Society for Experimental Stress Analysis*, v.12, n.2 (1954) pp.129-142.
103. Nicoletto,G., "Theoretical Fringe Analysis for Coherent Optics Method of Residual Stress Measurement," *J. of Strain Analysis for Engineering Design*, v.23, n.4 (1988) pp.169-178.
104. Chaoui,Kamel, Moet,Abdelsamie, and Chudnovsky,Alexander, "Strain Gage Analysis of Residual Stress in Plastic Pipes," *J. of Testing and Evaluation*, v.16 (1988) pp.286-290.
105. Lefebvre,D.R., Dillard,D.A., and Brinson,W.F., "A Model for the Diffusion of Moisture in Adhesive Joints, Part II: Experimental," *The Journal of Adhesion*, v.27, n.1 (1989) pp.19-40.
106. Ifju,P., and Post,D., "Thermal Strain Analysis Using Moiré Interferometry," *Proceedings of the SPIE - Applied Optics Meeting*, San Diego, California (August 1987).
107. Post,D., Wood,J.D., Han,B., Parks,V.J., and Gerstle,F.P., "Thermal Stresses in a Bimaterial Joint: an Experimental Analysis," *J. Applied Mechanics*, (submitted for publication).
108. Post, D., "Moiré Interferometry," Chapter 7, *Handbook of Experimental Mechanics*, A. S. Kobayashi, Editor, Prentice-Hall, Englewood Cliffs, NJ (1987).

109. Bowles, D.E., "Thermal Expansion of Composites Using Moiré Interferometry," MS Thesis in Engineering Mechanics, Virginia Polytechnic Inst. and State Univ. (July 1980).
110. Guo,Y., Post,D. and Czarnek,R., "The Magic of Carrier Fringes in Moiré Interferometry," *Experimental Mechanics* v.29, n.2, (June 1989) pp.169-173.
111. Guo,Y.,Post,D., and Han,B., "Thick Composites in Compression: An Experimental Study of Micromechanical Behavior and Smeared Engineering Properties," *J. of Composite Materials*, (to be published - March 1982).
112. Duncan,J.P., and Sabin,P.G., "An Experimental Method for Recording Curvature Contours in Flexed Elastic Plates," *Experimental Mechanics*, v.5, n.1 (1965) pp.22-28.
113. Post,D., Czarnek,R., and Joh,D., "Shear-Strain Contours by Moiré Interferometry," *Experimental Mechanics*, v.25, n.1 (September 1985) pp.282-287.
114. Post,Daniel, "Optical Interference for Deformation Measurements - - Classical, Holographic, and Moiré Interferometry," *Mechanics of Nondestructive Testing*, (Edited by W.W.Stinchcomb), Plenum Publishing Corp., New York (1980) pp.1-53.
115. Hecht,Eugene, and Zajac,Alfred, *Optics*, Addison-Wesley Publishing Company, Reading, Massachusetts (1979) pp.38,42,63-65.
116. Han,B., and Post,D., "Immersion Interferometer for Microscopic Moire Interferometry," *Experimental Mechanics*, (submitted for publication).
117. Han,B., "Higher Sensitivity Moiré Interferometry for Micromechanics Studies," *Optical Engineering*, (submitted for publication).
118. Pipes, R.B., "Effects of Interlaminar Shear Stress Upon Laminate Membrane Performance," Airforce Materials Laboratory/Industry Sponsored IRAD Status Report on Composite Materials, Bethpage, N.Y. (April 1970).
119. Pagano, N.J., and Whitney, J.M., "Geometric Design of Composite Cylindrical Characterization Specimens," *J. Composite Materials*, v.4 (1970) p.360.
120. Pagano, N.J., "On the Calculation of Interlaminar Normal Stress in Composite Laminates," *J. Composite Materials*, v.8 (Jan. 1974) pp.65-81.
121. Spilker, Robert L., "Edge Effects in Symmetric Composite Laminates: Importance of Satisfying the Traction-Free-Edge Condition," *J. Composite Materials*, v.14 (Jan. 1980) pp.2-20.
122. Marom,G. and Gershon,B. "Interfacial Bonding and Thermal Expansion of Fibre-Reinforced Composites," *J. of Adhesion*, v.7 (1975) pp.195-201.
123. Iancu,O.T., "Non-Singular Wedge Combinations at the Free Edge of a Brazed Ceramic-Metal Joint," *Computers . Structures*, v.33, n.3 (1989) pp.873-878.
124. Sun,C.T., and Chen,J.K., "Effect of Plasticity on Free Edge Stresses in Boron-Aluminum Composite Laminates," *J. of Composite Materials*, v.21 (Jan. 1990) pp.969-985.
125. Ting,C.T., and Chou,S.C., "Edge Singularities in Anisotropic Composites," *International J. of Solids and Structures*, v.17, n.11 (1981) pp.1057-1068.
126. Jones,R.M., *Mechanics of Composite Materials*, Chapters 2, 3, and 4, McGraw Hill Book Co., New York (1975).

127. Suresh,S., and Needleman,A., (Editors), "Proceedings of the Symposium on Interfacial Phenomena in Composites: Processing Characterization and Mechanical Properties," Newport, RI, U.S.A., June 1988, *Materials Science and Engineering*, v.A107 (January 1989) 280 pages.
128. Thornton,J.S., Montgomery,R.E., Thompson,C.M., and Dillard,D.A., "Analysis of Interfacial Stresses for Elastomeric Disks in Compression," *Polymer Engineering and Science*, v.28, n.10 (1962) pp.655-659.
129. Vedula,M., Pangborn,R.N., and Queeney,R.A., "Modification of Residual Thermal Stress in a Metal-Matrix Composite with the Use of a Tailored Interfacial Region," *Composites*, v.19, n.2 (March 1988) pp.133-137.
130. Frasier,J.T., and Rongved,Leif, "Force in the Plane of Two Joined Semi-Infinite Plates," *J. of Applied Mechanics*, v.24 (1957) pp.582-584.
131. Sun,C.T., Achenbach,J.D., and Herrmann,George, "Continuum Theory for a Laminated Plates," *J. of Applied Mechanics*, v. , n. (Sept. 1968) pp.467-475.
132. Hayes, Thomas J., *Elements of Ordinance*, Sec. 154, Wiley and Sons, New York (1938).
133. Oel,H.J., and Fréchette,V.D., "Stress Distribution in Multiphase Systems: II. Composite Disks with Cylindrical Interfaces," *J. of the American Ceramic Society*, v.69, n.4 (April 1986) pp.342-346.
134. Bikerman,J.J., "On a Theory of Interfacial Tension," *J. of Adhesion*, v.3 (1971) pp.19-22.
135. Feathers,James K., and Scott,William D., "Prehistoric Ceramic Composite from the Mississippi Valley," *American Ceramic Society Bulletin*, v.68, n.3 (1989) pp.554-557.
136. Cole,Sanford S., and Inge,John E., "Calculation and Measurement of Stress in a Ceramic-to-Metal Seal," *Am. Ceramic Society Bulletin*, v.40, n.12 (Dec. 1961) pp.738-743.
137. Suganuma,Katsuaki, Okamoto,Taira, Koizumi,Mitsue, and Shimada, Masahiko, "Method for Preventing Thermal Expansion Mismatch Effect in Ceramic-Metal Joining," *J. of Material Science Letters*, v.4 (1985) pp.648-650.
138. Kimura,Osamu, and Kawashima,Toshio, "Analysis of Thermal Stresses in a Ceramic-Metal Joint with Thermal Expansion Mismatch (III).," *J. of the Japan Society of Powder and Powder Metallurgy*, v.36, n.1 (February 1989) pp.1-6 (alternate numbering, also numbered pp.1-6), (*in Japanese*).
139. Osamu,Kimura, "Analysis of Thermal Stresses in a Ceramic-metal Joint (II).," *J. of the Japan Society of Powder and Powder Metallurgy*, v.34, n.9 (1987) pp.152-155 (also numbered pp.518-521), (*in Japanese*).
140. Koguchi,Hideo, Kaya,Toshinori, and Yada,Toshio, "Thermal Stress Analysis of Joints of Ceramics and Metals, (1st Report: Variation of Stress Concentration and Plastic Region by Modifying Size of Joints)," *Nihon Kikai Gakkai. in: Nihon Kikaisakkai rombunsh u..* v.55, n.520 (Dec. 1989) pp.2527-2532, (*in Japanese*).
141. Dalgleish,B.J., Lu,M.C., and Evans,A.G., "The Strength of Ceramics Bonded with Metals," *Acta Metallurgica*, v.36, n.8 (1988) pp.2029-2035.

142. Suganuma, Katsuaki, Okamoto, Taira, Shimada, Masahiko, and Koizumi, Mitsue, "New Method for Solid-State Bonding Between Ceramics and Metals," *Communications of the American Ceramic Society*, v.66, n.7 (July 1983) pp.C117-C118.
143. Borom, Marcus P., and Turkalo, Anna M., "Strength and Microstructure in Lithium Disilicate Glass-Ceramics," *Am. Ceramic Society Journal*, v.58, n.9-10 (1975) pp.385-391.
144. Watkins, R.D., and Loehman, R.E., "Interfacial Reactions Between a Complex Lithium Silicate Glass-Ceramic and Inconel 718," *Advanced Ceramic Materials*, v.1, n.1 (1986) pp.77-80.
145. Loehman, Ronald E., and Tomsia, Antoni P., "Joining of Ceramics," *American Ceramic Society Bulletin*, v.67, n.2 (February 1988) pp.375-380.
146. Varshneya, Arun K., "Stresses in Glass-to-Metal Seals, Glass III," *Treatise on Material Science and Technology*, v.22 (1982) pp.241-306.
147. Pask, Joseph A., "From Technology to the Science of Glass/Metal Sealing," *Am. Ceramic Society Bulletin*, v.66, n.11 (Nov. 1987) pp.1587-1592.
148. Howe, E.E. and Lange, L.A., "The Use of the Interferometer in the Porcelain Enameling Industry," *Better Enameling*, v.7, n.9 (Sept. 1936) pp.11-13, 26-27.
149. Fellows, R.L., and Howe, E.E., "Effect of Mill Additions on the Thermal Expansion of Sheet-Iron Ground-Coat Enamels," *J. of the American Ceramic Society*, v.19, n.4 (1936) pp.109-111.
150. Harrison, W.N., Shelton, S.M., and Wadleigh, W.H., "Strength and Young's Modulus of Some Ground-Coat Enamels for Sheet Iron," *J. of the American Ceramic Society*, v.18, n.3 (1935) pp.100-106.
151. Roy, S., Lefebvre, D.R., Dillard, D.A., and Reddy, J.N., "A Model for the Diffusion of Moisture in Adhesive Joints, Part III: Numerical Simulations," *The Journal of Adhesion*, v.27, n.1 (1989) pp.41-62.
152. Hu, S.M., "Film-Edge-Induced Stress in Substrates," *J. of Applied Physics*, v.50, n.7 (July 1979) pp.4661-4666.
153. Lundin, C.E., "Dissimilar Metal Welds - Transition Joints Literature Review," *Welding Journal*, v.61, n.2 (Feb. 1982) pp.58s-63s.
154. Taylor, T.C., and Yuan, F.L., "Thermal Stress and Fracture in Shear-Constrained Semiconductor Device Structures," *I R E* v.ED-9 (May 1962) pp.303-308.
155. van den Bogert, W.F., Molter, M.J., Belton, D.J., Gee, S.A., and Akylas, V.R., "Thermal Stress in Epoxy Molding Compounds and Packaged Devices," *Polymer Material Science Engineering*, v.59 (Sept. 1988) pp.642-646.
156. Auletti, Craig R., Kessler, John L., and Spalding, John A., Jr., "Compliant Silicone Helps Control Thermal Expansion Mismatch," *Adhesives Age*, v.32, n.2 (Feb. 1989) pp.33-37.
157. Ripling, E.J., Mostovoy, S., and Bersch, C., "Stress Corrosion Cracking of Adhesive Joints," *J. of Adhesion*, v.3 (1971) pp.145-163.
158. Das, M.P., Kaschner, R., Nafari, N., and Aiesche, P., "Adhesive Forces at Bimetallic Interfaces," *Solid State Communications*, v.63, n.5 (1987) pp.367-370.

159. Erdogan, F. and Gupta, G.D., "The Torsion Problem of a Disk Bonded to a Dissimilar Shaft," *Int. J. Solids and Structures*, v.8 (1972) pp.93-109.
160. Adams, R.D., Coppendale, J. and Peppiatt, N.A., "Stress Analysis of Axisymmetric Butt Joints Loaded in Torsion and Tension," *J. of Strain Analysis*, v.13, n.1 (1978) pp.1-10.
161. Cao, H.C., Thouless, M.D., and Evans, A.G., "Residual Stresses and Cracking in Brittle Solids Bonded with a Thin Ductile Layer," *Acta Metallurgica*, v.36, n.8 (1988) pp.2037-2046.
162. Sawa, T., Temma, K., and Tsunoda, Y., "Axisymmetric Stress Analysis of Adhesive Butt Joints of Dissimilar Solid Cylinders Subjected to External Tensile Loads," *International J. of Adhesion and Adhesives*, v.9, n.3 (July 1989) pp.161-169.
163. Chen, Du, and Cheng, Shun, "Stress Distribution in Plane Scarf and Butt Joints," *J. of Applied Mechanics*, v.57 (March 1990) pp.78-83.
164. Chen, D. and Cheng, S., "An Analysis of Adhesive-Bonded Single-Lap Joints," *J. Applied Mechanics*, v.50 (March 1983) pp.109-115.
165. Gilbert, Y. and Rigolot, A., "Determination of Stress Distribution in Double-Lap Joints, Matched Asymptotic Expansions and Conformal Mapping," *Adhesively Bonded Joints: Testing, Analysis, and Design, ASTM STP 981*, W.S. Johnson, Ed., American Society for Testing and Materials, Philadelphia (1988) pp.145-159.
166. Kant, Rishi, "Solutions for Potentials in a Lap Joint of Arbitrary Geometry and Dissimilar Materials," *Q. J. of Mechanics and Applied Math*, v.40, n.3 (1987) pp.315-325.
167. Hattori, Toshio, Nakamura, Masayuki, and Ishizuka, Tazuro, "Fretting Fatigue Analysis of Strength Improvement Models with Grooving or Knurling on a Contact Surface," *Symposium on Standardization of the Fretting Fatigue Test Method and Equipment*, pp.1-12.
168. Hattori, Toshio, "A Stress-Singularity-Parameter Approach for Evaluating Adhesive Strength of Single-Lap Joints," (*Submitted for Publication*), pp.1-11.
169. Crews, J.H., Jr., Shivakumar, K.N., and Raju, I.S., "Factors Influencing Elastic Stresses in Double Cantilever Beam Specimens," *Adhesively Bonded Joints: Testing, Analysis, and Design, ASTM STP 981*, W.S. Johnson, Ed., American Society for Testing and Materials, Philadelphia (1988) pp.119-132.
170. Aivazzadeh, S., Bichara, M., Ghazal, A., and Verchery, G., "Special Mixed Finite Elements for Interfacial Stress Analysis of Adhesively Bonded Joints," *Adhesively Bonded Joints: Testing, Analysis, and Design, ASTM STP 981*, W.S. Johnson, Ed., American Society for Testing and Materials, Philadelphia (1988) pp.133-144.
171. Srivastava, K.N., Gupta, O.P., and Palaiya, R.M., "Interaction of Elastic Waves in Two Bonded Dissimilar Elastic Half-Planes Having Griffith Crack at Interface - I," *Int. J. of Fracture*, v.14, n.2 (April 1978) pp.145-154.
172. Mizoguchi, Takao, Kobayashi, Masato, and Inoue, Takao, "Stress Analysis and Strength Evaluation for Bonded Joints of Dissimilar Materials," *R. D. Res. Dev. Kobe Steel Ltd.*, v.39, n.2 (April 1989) pp.77-80, (*in Japanese*).
173. Harrison, N.L., and Harrison, W.J., "The Stresses in an Adhesive Layer," *J. of Adhesion*, v.3 (1972) pp.195-212.

174. Williams, James H., Jr. "Stresses in Adhesive between Dissimilar Adherends," *J. of Adhesion*, v.7 (1975) pp.97-107.
175. Kinloch, A.J., "Review: The Science of Adhesion, Part 2, Mechanics and Mechanisms of Failure," *J. of Materials Science*, v.17 (1982) pp.617-651.
176. Bigwood, D.A., and Crocombe, A.D., "Non-linear Adhesive Bonded Joint Design Analyses," *International J. of Adhesion and Adhesives*, v.20, n.1 (Jan. 1990) pp.31-41.
177. Hattori, Toshio, Sakata, S., and Watanaba, T., "A Stress Singularity Parameter Approach for Evaluating Adhesive and Fretting Strength," Transactions of the ASME: *Advances in Adhesively Bonded Joints*, MD-v.6, Editors: S.Mall, K.M.Liechti, and J.R.Vinson, (Book No. G00485) pp.43-50.
178. Kuenzi, E.W., and Stevens, G.H., "Determination of Mechanical Properties of Adhesive for Use in the Design of Bonded Joints," Report No. FPL-011, Wood Engineering Research, Forest Products Laboratory, Madison, Wisconsin, 53705 (September 1963).
179. Lefebvre, D.R., Dillard, D.A., and Ward, T.C., "A Model for the Diffusion of Moisture in Adhesive Joints, Part I: Equations Governing Diffusion," *The Journal of Adhesion*, v.27, n.1 (1989) pp.1-18.
180. Williams, M.L., "Stress Singularities, Adhesion, and Fracture," *Proceedings of the 5<sup>th</sup> U.S. National Congress of Applied Mechanics*, Minneapolis, June 14-17 (1966) pp.451-464.
181. Crose, J.G., Holman, R.L., and Pagano, N.J., "Validation of Advanced Composite Thermal Stress Analysis Methods," *J. of Engineering Materials and Technology*, v.109 (Jan. 1987) pp.40-46.
182. Kaprielian, P.V., Rogers, T.G., and Spencer, A.J.M., "Theory of Laminated Elastic Plates, Isotropic Laminae," *Philosophical Transactions of the Royal Society*, London, A324, (1988) pp.565-594.
183. Scott, W.R., "Wave Propagation in Anisotropic Layered Media," Report No. NADC-80099-60, Aircraft and Crew Systems Technology Directorate, Naval Air Development Center, Warminster, Pennsylvania, 18974 (June 1980).
184. Suganuma, Katsuaki, Odamoto, Taira, and Koizumi, Mitsue, "Effect of Interlayers in Ceramic-Metal Joints with Thermal Expansion Mismatches," *J. Am. Ceramics Society*, v.67, n.12 (1984) pp.256-257.
185. Yamada, T., Yokoi, K., and Kohno, A., "Effect of residual stress on the strength of alumina-steel joint with Al-Si interlayer," *J. of Materials Science*, v.25 (1990) pp.2188-2192.
186. Isaacs, H.S., "Initiation of Stress Corrosion Cracking of Sensitized Type 304 Stainless Steel in Dilute Thiosulfate Solution," *J. Electrochemical Society*, v.135, n.9 (Sept. 1988) pp.2180-2183.
187. Logan, H.L., *The Stress Corrosion of Metals*, Wiley, New York, 1966.
188. Robertson, W.D. (ed), *Stress Corrosion Cracking and Embrittlement*, Wiley, New York, 1956.
189. Hattori, Toshio, Nakamura, Masayuki, and Watanabe, Takashi, "Fretting Fatigue Analysis by Using Fracture Mechanics," *Transactions of the ASME*, paper no. 84-WA/DE-10 (1984) pp.1-7.



190. Zak,A.R. and Williams,M.L., "Crack Point Stress Singularities at a Bi-Material Interface," *J. Applied Mechanics*, v.30 (March 1963) pp.142-143.
191. England, A.H., "A Crack Between Dissimilar Media," *J. Applied Mechanics*, v.32 (June 1975) pp.400-402.
192. Kundo,T. and Hassan,T., "A Numerical Study of the Transient Behavior of an Interfacial Crack in a Bimaterial Plate," *Int. J. of Fracture*, v.35 (1987) pp.55-69.
193. Carpenter,William C., and Byers,Curtis, "A Path Independent Integral for Computing Stress intensities for V-notched Cracks in a Bi-material," *International Journal of Fracture*, v.35 (1987) pp.245-268.
194. Hull, D., *Introduction to Dislocations, 2nd Edition*, Pergamon Press, Oxford, 1975.
195. Wolf,D., and Phillpot,S., "Role of the Densest Lattice Planes in the Stability of Crystalline Interfaces: A Computer Simulation Study," *Materials Science and Engineering*, v.A-107 (Jan. 1989) pp.3-14.
196. Chou,Tsu-Wei, and Tetelman,Alan,S., "Elastic Cracks and Screw Dislocation Pile-Ups Crossing a Bimaterial Interface," *International J. of Fracture Mechanics*, v.7, n.3 (Sept. 1971) pp.331-338.
197. Gent,A.N., and Meinecke,E.A., "Compression, Bending, and Shear of Bonded Rubber Blocks," *Polymer Engineering and Science*, v.10, n.1 (Jan. 1970) pp.48-53.
198. Oel,H.J., and Fréchette,V.D., "Stress Distribution in Multiphase Systems: I. Composites with Planar Interfaces," *J. of the American Ceramic Society*, v.50, n.10 (Oct. 1967) pp.542-549.
199. Hattori,Toshio, Sakata,S., and Murakami,G., "A Stress Singularity Parameter Approach for Evaluating the Interfacial Reliability of Plastic Encapsulated LSI Devices," *J. of Electronic Packaging*, v.111 (December 1989) pp.243-248.
200. Messner, A.M., "Stress Distributions in Poker-chip Tensile Specimens," *Bull. 2nd Meeting Interagency Chem. Rocket Propulsion Working Group on Mechanical Behavior*, Chem. Propulsion Information Agency, Publication No. 28 (October 1963) pp.109-129.
201. Mukae,Shizuo, Katoh,Mitsuaki, Nishio,Kazumasa, Yokono,Yasukazu, and Nakamura,Kazuo, "Quality Evaluation and Investigation of Deformation Behavior of Joints of Dissimilar Aluminum Alloys," *Keikinzoiku Yosetsu*, v.26, n.2 (1988) pp.49-58 (also numbered pp.1-10), (*in Japanese*).
202. Dundurs,J., "Effect of Elastic Constants on Stress in a Composite Under Plane Deformation," *J. of Composite Materials*, v.1 (1967) pp.310-322.
203. Evans,A.G., and Mehrabian,R., "The Processing and Mechanical Properties of High Temperature/High Performance Composites," Annual Report, University Research Initiative, Contract No.: N00014-86-K-0753, (Sept.1987-Sept.1988), 6 books, 1450 pages (sponsored by DARPA, monitored by ONR).
204. Williams,M.L., "Stress Singularities Resulting From Various Boundary Conditions in Angular Corners of Plates in Extension," *J. of Applied Mechanics*, v.19 (Dec. 1952) pp.526-528.

205. Muki,Rokuro, and Sternberg,Eli, "Elastostatic Load Transfer to a Half-Space from a Partially Embedded Axially Loaded Rod," *International J. of Solids and Structures*, v.6 (1970) pp.69-90.
206. Muki,Rokuro, and Sternberg,Eli, "On the Diffusion of an Axial Load from an Infinite Cylindrical Bar Embedded in an Elastic Medium," *International J. of Solids and Structures*, v.5 (1969) pp.587-605.
207. Mikata,Y., and Taya,M., "Stress Field in and Around a Coated Short Fiber in an Infinite Matrix Subjected to Uniaxial and Biaxial Loadings," *J. of Applied Mechanics*, v.52 (March 1985) pp.19-24.
208. Jentsch,Lothar, "On a Thermal Stress Problem for Contacting Half-Spaces with Inclusions of Other Material Involving a New Method for Computing Potentials and Singular Integrals," *Mathematical Methods in the Applied Sciences*, v.10 (1988) pp.225-243.
209. Dundurs,J., and Lee,M.-S., "Stress Concentrations at a Sharp Edge in Contact Problems," *J. of Elasticity*, v.2, n.2 (June 1972) pp.109-112.
210. Gomez,Celina, and Dundurs,John, (Note) "The Local Stress State at a Sharp Corner of an Expanding Inclusion," *J. of Applied Mechanics*, v.49 (March 1982) pp. 229-231.
211. Benthem,J.P., and Minderhoud,P., "The Problem of the Solid Cylinder Compressed Between Rough Rigid Stamps," *International J. of Solids and Structures*, v.8 (1972) pp.1027-1042.
212. Comninou,Maria, "Stress Singularity at a Sharp Edge in Contact Problems with Friction," *J. of Applied Mathematics and Physics*, v.27 (1976) pp.493-499.
213. Blanchard,J.P., and Ghoniem,N.M., "Relaxation of Thermal Stress Singularities in Bonded Viscoelastic Quarter Planes," *J. of Applied Mechanics*, v.56 (Dec. 1989) pp.756-762.
214. Pagano,N.J., "Exact Solutions for Composite Laminates in Cylindrical Bending," *J. of Composite Materials*, v.3, (July 1969) pp.398-411.
215. Dundurs,J., (Discussion) "Edge-Bonded Dissimilar Orthogonal Elastic Wedges Under Normal and Shear Loading," *J. of Applied Mechanics*, v.36 (Sept. 1969) pp.650-652.
216. Reissner,E., and Stavsky,Y., "Bending and Stretching of Certain Types of Heterogeneous Anisotropic Elastic Plates," *J. of Applied Mechanics*, v.28 (Sept. 1961) pp.402-408.
217. Timoshenko,S.P., and Goodier,J.N., *Theory of Elasticity*, McGraw-Hill Book Co., New York (1970) pp.15-17.
218. Ugural,A.C., and Fenster,S.K., *Advanced Strength and Applied Elasticity: The SI Version*, Elsevier, New York (1981) pp.6-8,58-61.
219. Shames,Irving H., *Mechanics of Deformable Solids*, Robert E. Krieger Publishing Company, Huntington, New York (1979) pp.64-65,141-164.
220. Frederick,Daniel, and Chang,Tien Sun, *Continuum Mechanics*, Scientific Publishers, Inc., Cambridge (1972) p.136.
221. Dawson,Thomas H., *Theory and Practice of Solid Mechanics*, Plenum Press, New York (1976).

222. Young, Warren C., *Roark's Formulas for Stress and Strain*, Sixth Edition, McGraw-Hill Book Company, New York (1989).
223. Mase, George E., *Theory and Problems of Continuum Mechanics*, Schaum's Outline Series, McGraw-Hill Book Company, New York (1970) pp.140-147.

## Vita

The author was born in Bangor, Maine, on January 5, 1957, and is the youngest of four children of Dr. and Mrs. Herbert H. Wood. She started her education in Albion, Michigan, and continued it in Kansas City, Missouri, through the ninth grade, before her family moved to Virginia. Three years later, she graduated from West Springfield High School, Springfield, Virginia, in 1975.

She began her studies toward a B.S. in Civil Engineering at Old Dominion University and completed her degree in Civil Engineering at Virginia Tech (Virginia Polytechnic Institute and State University) in 1981. During 1978, she worked for Jones Associates in Bellevue, Washington, as an Engineering Technician and Draftsman, and in 1980 worked for Boeing Aerospace Company in Kent, Washington. She completed her M.S. degree in Engineering Mechanics at Virginia Tech (Virginia Polytechnic Institute and State University) in 1983 and began a Ph.D. degree in Materials Engineering Science.

While on her way to attend the *1985 SEM (Society for Experimental Mechanics) Spring Conference on Experimental Mechanics* (in Las Vegas, Nevada), the author was near-fatally struck by a motor vehicle, estimated to be travelling in excess of 80-m.p.h.. She was not in a motor vehicle. Consequently, as a result, she suffered very extensive injuries and required a long and extensive recovery, which interrupted her studies.

